Budapest University of Technology and Economics

Pál Vásárhelyi Doctoral School of Civil Engineering and Earth Sciences

Department of Structural Engineering

Performance-based wind design of lattice towers

PhD Dissertation by

Ágnes Kenéz

Supervisor:

Dr. Attila László Joó

2024

Budapest

"Probability does not exist."

Bruno de Finetti

Acknowledgements

I would like to express my sincere gratitude to Dr. Attila László Joó, my supervisor, for suggesting this research topic and providing guidance. I extend my appreciation to all the members of the Department of Structural Engineering at Budapest University of Technology and Economics for their kindness and constructive feedback, with special thanks to Dr. László Dunai and Dr. Balázs Kövesdi, the heads of the department, for granting me this opportunity.

I am deeply thankful to Hungarian Telekom Telecommunications Plc. for generously sharing the measurement data series related to the tower under investigation. Additionally, I would like to acknowledge the Hungarian Meteorological Service for providing access to the meteorological data series used in this research.

I would like to seize this opportunity to express my appreciation to my family and friends for their unwavering support and words of encouragement, particularly my husband and child, as well as my mother, for their boundless patience and assistance throughout this journey, especially the professional assistance provided by my husband. Their collective support has played a significant role in the completion of this thesis.

Table of Contents

Nomenclature

Acronyms

CDF	Cumulative distribution function
CV	Coefficients of variation
DM	Damage measure parameter
DV	Decision variable
EDP	Engineering demand parameter
FEM	Finite element method
GEV	Generalized extreme value distribution
GMNIA	Geometrically and materially nonlinear analysis with imperfections
GPD	Generalized Pareto distribution
HMS	Hungarian Meteorological Service
IM	Intensity measure parameter
IP	Interaction parameter
LND	Lognormal distribution
MC	Monte Carlo simulation
MLE	Maximum likelihood estimation
PBD	Performance-based design
PBWD	Performance-based wind design
PBWE	Performance-based wind engineering
PDF	Probability density function
POT	Peaks-over-threshold
ULS	Ultimate limit state
SEM	The standard error of the mean
SLS	Serviceability limit state
SP	Structural parameter
STD	Standard deviation

Latin symbols

c_{e}	Exposure factor
c_{f}	Drag or force coefficient
c_{g}	Gust factor

c_{r}	Roughness factor
f_{y}	Yield strength
f_{u}	Ultimate strength
g	Peak factor
E_a	Young's modulus
I_v	Turbulence intensity
$\bar{r}$	Time-averaged response
$\tilde{r}_B$	Background response
$\tilde{r}_R$	Resonant response peak
u	Threshold
u_*	Friction velocity
v	Wind velocity
$v_{\mathrm{b},0}$	Fundamental basic wind velocity
Re	Reynolds number
S	Internal axial forces in chords
z	Height
z_0	Roughness length

Greek symbols

α	Wind direction
α_{ULS}	Load amplification factor
μ	Location parameter of the GEV and GPD distributions
κ	von Kármán constant
ξ	Shape parameter of the GEV and GPD distributions
ρ	Air density
σ	Scale parameter of the GEV and GPD distributions
τ	Reparametrized scale parameter
φ	Rotation
ϕ	Solidity ratio
ψ	Stability parameter for atmospheric stabilities

1 Introduction

1.1 Wind engineering

Large uncertainty is involved in the characterization of different environmental actions, such as snow, wind and temperature and their contributions to the structural response as well. The wind load is one of the most significant actions influencing the integrity of several structural types, especially those at exposed sites such as bridges, wind turbines and telecommunication masts. Compromise has to be found in the structural design process between safety considerations and extra costs of overdesign. Therefore, it is of utmost importance to examine the related modelling assumptions and to make sure that the model aptly describes reality.

Over a century ago, wind actions on lattice towers were estimated in a highly approximate and conservative manner: assuming the maximum wind velocity recorded at the top remained constant along the tower. In the 1950s, with an increasing number of electricity transmission towers and radio towers, engineers began considering the cost of these structures, which prompted them to compare actual loads on conductors with the usual conservative assumptions. Most of the experimental findings were documented in reports published by the Conseil International des Grands Réseaux Électriques (CIGRE), including works by Birjulin et al. (1960), Mors and Baer, (1956), Marchal et al. (1956), Poyart (1952) and Zetterholm and Sandin (1954). Consequently, design wind actions were reduced based on experimental reduction factors (Ducloux and Figueroa, 2016).

Davenport (1961; 1967) had set a milestone by introducing the stochastic description of wind, which allowed a more accurate monitoring of aerodynamic effects and paved the way for their statistical evaluation. The term "wind engineer" originated during this period. The initial "Recommendations for the calculation of wind effects on buildings and structures" in Europe were published in 1978 (ECCS, 1978). Wind Loading Chain of Alan G. Davenport (Davenport, 1982) presents a systematic approach to address specific wind engineering problems, conceptualizing them as a wind loading chain (Figure 1.1). This framework enables the evaluation of wind loads and wind-induced responses for buildings and structures.

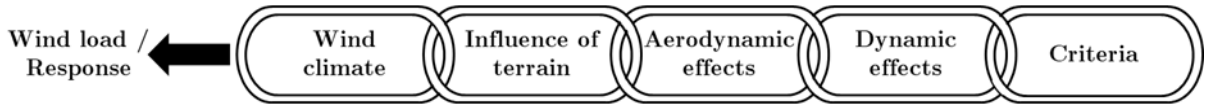

Figure 1.1. Wind Loading Chain of Alan G. Davenport (Davenport, 1982)

The first IEC standard (IEC 826-2) focusing on wind and temperature loadings on electrical overhead lines components was issued in 1985. In the 1990s, the CEN Technical Committee initiated the development of Eurocode standards for wind actions. The first experimental Eurocode for wind actions, ENV 1991-2-4, was published in 1995, followed by the publication of the Eurocode for "masts, towers, and chimneys," ENV 1993-3-1, in 1997. By the early 2000s, the final Eurocode standard for wind actions (EN 1991-1-4, 2005) and the final Eurocode standard for towers and masts (EN 1993-3-1, 2006) were both published. Furthermore, the first CENELEC standard (European Committee for Electrotechnical Standardization, EN 50341-1, 2001), dealing with the design of electrical overhead lines, was issued (Ducloux and Figueroa, 2016).

The Eurocodes are currently being revised and the main objectives of this maintenance are to incorporate the latest knowledge in the field and to minimize the number of nationally determined parameters to enhance the harmonization of the Eurocodes (Nielsen, 2019). Key changes in EN 1991-1-4 include deriving basic wind velocity from measurements at meteorological stations, employing probabilistic models for wind actions, and deriving design parameters from wind tunnel tests and numerical simulations (Malakatas, 2023).

1.2 Problem statement and motivation

Design formulae within the majority of structural design codes or standards, such as the Eurocodes, are based on the semi-probabilistic method using partial safety factors on both the resistance and action sides where design values should be conservative estimates. Some studies (Baravalle and Köhler, 2018; Vrouwenvelder and Scholten, 2010) pointed out that applying one single partial safety factor $\gamma_Q = 1.50$ for all unfavourable environmental variable actions may not be reasonable since these environmental actions, such as wind, snow and temperature, originate from different physical phenomena and are represented by different models. Moreover, it may underestimate the annual exceedance for a desired probability resulting in lower reliability than the Eurocode target value. On the other hand, according to the findings

of previous research (Georgakis et al., 2009; Nielsen, 2019) and our observations, extreme storms caused significantly less structural stress or even damage than expected. Hence, accurate modelling of wind load can be employed to demonstrate and verify that the actual utilization of telecommunication lattice towers is significantly lower than the design level according to the standards in several cases, allowing for the installation of additional antennae on the structure.

Therefore, the following questions are sought to be answered: What causes the discrepancy between the stresses calculated according to the Eurocode (EN 1993-3-1), and the measured values? Which parameter of the model can be adjusted to improve the alignment of the model with the real behaviour?

In the probabilistic modelling of structural performance, the consideration of the parameter estimation uncertainty (PEU) in extreme wind speed models is often overlooked. The PEU stems from the uncertainty associated with model parameters, which cannot be precisely determined using statistical methods. Nevertheless, several studies have demonstrated the substantial impact of PEU on the modelling of extreme environmental actions (Bakker et al., 2021; Baravalle & Köhler, 2018; Rózsás and Sýkora, 2016). In this study, the assessed parameters of the extreme wind speed model are treated as stochastic variables, allowing for the incorporation of PEU in the modelling of structural performance.

Furthermore, advancements in computer technology have paved the way for alternative design procedures that utilize fully probabilistic approaches and simulation techniques. Performance-based design (PBD) incorporates a comprehensive risk assessment that goes beyond structural safety considerations to include the cost of consequences. It means that the potential economic and social impacts of structural failure or underperformance are taken into account during the design process. Additionally, the approach allows for the incorporation of measurements and real-time monitoring of the structure. This information can be used to update various parameters, such as material properties, imperfections, and environmental influences, ensuring that the design remains adaptive and responsive to changing conditions throughout its lifecycle. This dynamic aspect of performance-based design has the potential to reduce uncertainties and enhances the ability to achieve and maintain optimal performance levels over time. The concept of PBD has emerged as a promising design methodology, and it has been extended and widely embraced in the field of wind

engineering, giving rise to Performance-based wind engineering (PBWE). The PBWE is gaining increasing popularity as it effectively addresses various wind engineering problems, making it a widely adopted approach in the field.

Therefore, the presented research work focuses on the integration of the Performance-based wind design (PBWD) framework with a monitoring system and finite element model to assess the structural reliability. Moreover, Bayesian analysis is introduced, an effective approach for combining various sources of information, including diverse measurements and probabilistic models for wind action, in order to determine the basic wind velocity. This integration signifies the development of the second generation of the Eurocodes, which aims to broaden its scope.

1.3 Research strategy

First, a thorough literature review examines prior research in the field of wind engineering, focusing on the impact of extreme wind conditions on towers. This includes modelling aspects related to the basic wind velocity, tower aerodynamics, and drag coefficient characterization. The research spans various disciplines, such as meteorology, probability theory, fluid dynamics, and structural analysis.

A performance-based design framework is then introduced for analysing the response of telecommunication lattice masts to extreme wind conditions. This framework is applied to investigate a freestanding lattice tower situated in the suburban area of Sződliget, Central Hungary. The tower is equipped with cup anemometer wind speed sensors at the top and middle, as well as strain gauges on the bottom chord members to measure its response to meteorological loads.

Additionally, data from Sződliget is augmented with information from other meteorological stations under the Hungarian Meteorological Service. Various procedures and parameters for extreme wind speed distribution models are used to estimate the basic wind velocity from different measurement datasets. Bayesian inference techniques are employed to synthesize information from these diverse sources.

The wind-structure interaction is modelled using the equivalent static method, following the EN 1993-3-1 standard. This involves the utilization of the drag coefficient, and the results are compared with drag coefficients obtained from wind tunnel experiments. A finite element model with beam elements is developed to simulate the structural response. This model considers self-weight and extreme wind effects. The

internal axial forces calculated from strain measurements on the bottom chord member are compared with numerical model results, which incorporate wind load drag coefficients determined according to EN 1993-3-1 and data from wind tunnel experiments.

The manuscript is structured as follows: Section 2 offers insights into the comprehensive literature review. In Section 3, detailed information about the investigated mast is provided, along with an explanation of the PBWE framework. This section encompasses discussions on wind velocity, aerodynamics, finite element models, and probabilistic analyses. Section 4 presents the results obtained from measurements and the probabilistic finite element model, followed by a corresponding discussion. Finally, Section 5 summarizes the conclusions of the dissertation, and Section 6 provides an overview of the new scientific findings from this research.

2 Literature review

Davenport's methodology acknowledges that wind loading on a structure results from the combined effects of the local wind climate, described statistically; the local wind exposure, influenced by terrain roughness and topography; the aerodynamic characteristics of the building shape; and the potential for load increases due to wind-induced resonant vibrations (Figure 1.1). Wind is defined as the movement of the Earth's atmosphere, the effects of wind on structures as aerodynamic effects, and the forces acting on structures as aerodynamic forces or wind loads. Drawing an analogy to a physical chain, the final outcome is determined by the weakest link or component in the process. Emphasizing strong links yields little gain, while neglecting the weak ones can result in significant losses. Therefore, the approach underscores the importance of addressing and understanding all aspects of the wind loading chain for accurate and reliable wind engineering assessments.

2.1 PBWE methodology

The general framework of PBWE was published first in 2004 within the framework of an Italian research project (Paulotto et al., 2004). Since then, several studies (Chuang and Spence, 2017; Huang et al., 2012; Petrini and Ciampoli, 2012) have illustrated the applicability and improvements of this methodology, while only few studies focused especially on lattice towers (Depina et al., 2021; Tessari et al., 2017). In wind engineering, design variables can be derived by following a chain of causes and effects. This PBWE event chain (Figure 2.1) is similar to Davenport's chain (Davenport, 1982); steps of the approach are the following:

I. Characterizing the wind field and its associated uncertainty is essential in modelling for wind engineering. Key parameters which describe sufficiently and efficiently the climate wind hazard should be chosen as intensity measure parameters (IM), e.g., wind velocity, wind direction, turbulence intensity.

II. Mechanical and material properties of the structure of interest, whose uncertainty may contribute significantly to the structural performance, should be considered as stochastic variable in structural parameters (SP).

III. The interaction phenomenon between the environment and the structure should be modelled in probabilistic terms and can be described with interaction parameters (*IP*). Davenport's work allows for the analysis of turbulent wind loads on structures by differentiating between static wind loads and gust loads. The forces (loads) due to the turbulence of the wind are called wind gust loads. Aeroelasticity is the interaction of aerodynamic forces and structural flexibility that can lead to excessive displacement and failure of the structure. The aerodynamic effects of turbulent flow can be treated separately from the aeroelastic effects.

IV. In order to perform the probabilistic analysis of structural response, relevant engineering demand parameters (*EDP*) should be defined, which are measurable quantities such as e.g., deformation or acceleration of the structure, internal forces, stresses, etc.

V. Damage measure parameters (*DM*) should be also defined by one or combination of more *EDP*s to quantify the structural damage, i.e., unacceptable performance of the structure. Relevant *EDP* and *DM* parameters can be identified based on the type of the considered problem. Typical *DM*s are associated with collapse or with other similar forms of structural failure or correspond to conditions beyond which specified service requirements are no longer fulfilled. Former one is low- and the latter one is high-performance level, respectively.

VI. The intended structural performances and consequence of damage are quantified through decision variables (*DV*). As mentioned above, low- and high- performance level should be distinguished, i.e., the ultimate limit state (ULS) and the serviceability limit state (SLS), respectively. Comprehensive and advanced model shall include loss analysis where decisional strategy is developed in order to minimalize the total risk or maximizing the defined utilization taking the whole lifetime into account. For the reason of ethical and practical difficulties of considering the economic losses or losses of lives, the assessment is simplified to the fulfillment of a limit state; cost analysis is not perfomed in the current study.

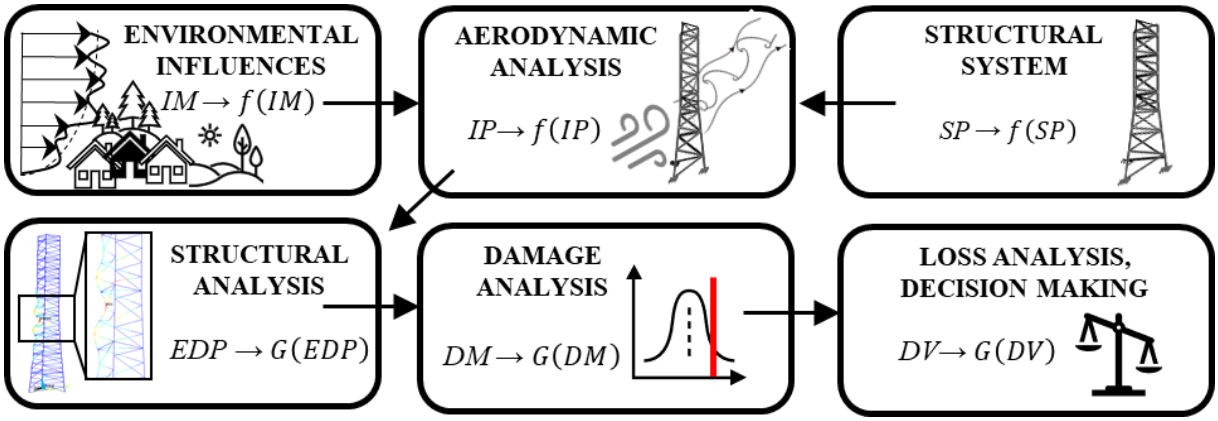

Figure 2.1. Framework of the Performance-based wind engineering

Detailed description of selected stochastic variables can be found in Section 3.3. The structural risk is defined as the probability of a relevant decision variable exceeding a threshold level dv, and can be expressed with a complementary cumulative distribution function (CCDF) in Eq. (2.1):

$$G(dv)=\mathrm{P}(DV>dv)=\int\int\int\int\int G(DV|\,DM)\;f(DM|\,EDP)\;f(EDP\,|\,IM,IP,SP)\cdot \\ \cdot f(IP|IM,SP)\,f(\,IM)\,f(SP)\;dDM\,dEDP\,dIP\,dIM\,dSP, \tag{2.1}$$

where $f(\cdot)$ is the probability density function of the relevant parameter (PDF), $f(\cdot|\cdot)$ is conditional probability density function and $G(\cdot)$ is a complementary cumulative distribution function.

If loss analysis is not carried out, and the chosen EDP is assumed as the measure of the structural damage ($EDP = DM$), furthermore, the limit state is quantified in terms of EDP, Eq. (2.1) is simplified to the following equation:

$$G(EDP)=\int\int\int G(EDP|\,IM,IP,SP)\,f(\,IP|IM,SP)f(\,IM)f(SP)\quad dIP\,dIM\,dSP. \tag{2.2}$$

Ciampoli et al. (2011) demonstrated the method by studying a long span suspension bridge. In their analysis, only the mean wind speed was considered as a stochastic IM parameter, and only accounting for aleatory uncertainty. The turbulent wind velocity time series have been generated as a multivariate stationary Gaussian process. The IP and SP, however, were treated as deterministic, while the structural analysis was conducted using a finite element model. The chosen EDPs, i.e., the rotational velocity, the longitudinal and vertical acceleration, were evaluated by Monte Carlo simulation.

Chuang and Spence (2017) proposed the PBWE framework that integrates probabilistic shakedown analysis with system-level damage and loss estimation models. Probabilistic shakedown analysis assesses the structural performance under repeated or fluctuating loads over an extended period in probabilistic terms. This methodology ensures that the structure will eventually reach a stable condition or "shakedown," where it does not undergo excessive and cumulative plastic deformation over time, mitigating the risk of failure.

Tessari et al. (2017) have applied the PBWE methodology for the case of a steel lattice tower utilizing finite element model combining with the First Order Reliability Method and crude and importance sampling Monte Carlo simulation techniques. It has been concluded that both probabilistic equivalent static wind load (ESWL) method and discrete dynamic method lead to very similar safety levels. The assumption of considering only the most unfavourable wind direction was found to be excessively conservative. Structural parameters, such as steel yield strength, dead load factor, which are often treated as stochastic, had minimal impact on failure probabilities due to the significant influence of wind field parameters.

Depina et al. (2021) investigated the performance of critical telecommunication infrastructure along the Croatian coastline under the influence of the Bora wind. The research implements relatively simple functions to assess losses directly associated with structural failure. The loss function considers various scenarios where ULS or SLS, including displacement- and rotation-based SLS, might be exceeded, and it accounts for different loss levels associated with the corresponding limit states. The estimated risks arising from the combination of rotation-based serviceability and the ultimate limit state are found to be moderate, reaching up to 13% of the total structural value for low rotational limits. On the other hand, the estimated risks for displacement-based serviceability are remarkably low.

The estimation of point estimates and uncertainty in parameters is part of the modelling process and the relationship between the parameter uncertainty and the uncertainty of the DV should be determined. Briggs et al. (2012) provides comprehensive guidelines regarding the evaluation and reporting of uncertainty, covering both deterministic sensitivity analysis techniques and probabilistic methods.

In the PBWE modelling, three sources of uncertainty can be taken into account:

i) aleatory uncertainty arising from the unpredictable nature of a variable, which cannot be eliminated.

ii) epistemic uncertainty resulted by the incompleteness and errors of measurements, which can be reduced by gathering more data or by refining the model.

iii) model uncertainties due to the limitations of our knowledge.

2.2 Extreme wind phenomena and their modelling

2.2.1 Meteorological Basics

At its most fundamental level, wind flows are a result of the sunrays striking the Earth, with the Equator receiving more energy per unit area than the Poles. Consequently, the warmer air at the Equator rises, while the colder polar air sinks, leading to the development of a flow pattern with the primary goal of transporting this excess heat from the Equator to the Poles, seeking to achieve equilibrium. The rotation of the Earth introduces the Coriolis force, causing the wind to veer or turn, resulting in a significantly more complex and intricate wind flow pattern.

There is a wind gradient in the wind flow just a few hundred meters above the Earth's surface due to aerodynamic drag. The height of this so-called Surface layer primarily varies with the time of day and atmospheric stability. The Ekman layer, located above the Surface layer, is characterized by a three-component force balance involving the pressure gradient, friction, and Coriolis forces. Collectively, the two abovementioned layers of the lower atmosphere form the planetary boundary layer and it goes up to about 1 km. Above the Ekman layer lies the 'free atmosphere', which is defined as the layer where the influence of surface friction becomes negligible. This layer is no longer affected by the surface. Landberg's book (2015) offers a comprehensive insight into the meteorological aspects of wind loads and wind energy.

The study of the atmosphere encompasses various areas that vary based on time and spatial scales. Understanding these scales helps us analyse winds at different levels, ranging from global to local, and how various weather systems simultaneously influence a specific site. Meteorology divides into micro-, meso-, synoptic- and global scale meteorology, focusing on timescales ranging from minutes to months (Table 2.1 and

Figure 2.2). In Europe, the common severe wind events that can damage lattice towers are extra-tropical storms. These synoptic winter storms are considered the ideal "academic winds" as they possess statistical properties of a Gaussian process, making them suitable for applying Davenport's model. In the following I will only deal with the characterisation and impact of these time-averaged synoptic winds.

Table 2.1. The scales of atmospheric flow, the typical length and time scales

Scale	**Length scale [m]**	**Time scale**	**Phenomenon**
Global	10^7	Weeks to months	Transport of heat from the tropics to the poles
Synoptic	10^6	Days	Extratropical cyclones, frontal zones, jet streams
Meso	10^5	Hours to weeks	Thunderstorms, fronts, tropical and extratropical cyclones
Micro	10^2	Minutes to hours	Individual thunderstorms, clouds, and local turbulence caused by buildings and other obstacles

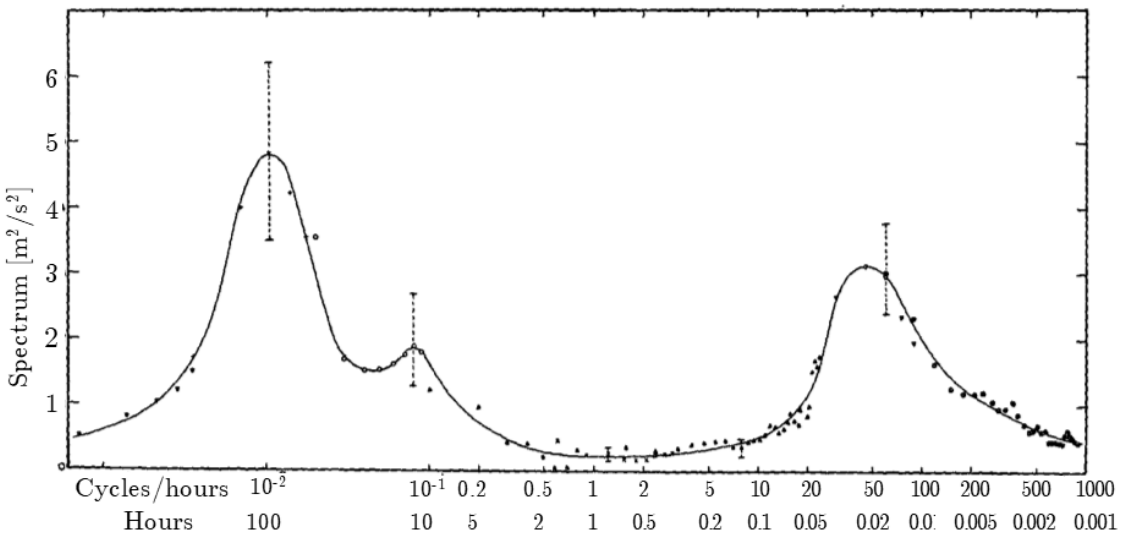

Figure 2.2. Horizontal wind-speed spectrum at Brookhaven National Laboratory at about 100 m height (Hoven, 1956)

In civil engineering practice, local extreme wind speed for a constructed structure is determined according to structural design standards. Typically, this approach assumes that the wind environment will remain constant over a large spatial scale. This assumption is generally valid for flatlands and plateaus, where strong wind events are typically macro-scale or meso-scale occurrences. However, Ma et al (2023) introduced a novel extreme wind speed model suitable for mountainous regions affected by mixed climates, distinguishing local-scale and large-scale synoptic winds. Their approach involves converting and integrating synoptic wind speeds from nearby meteorological stations with local wind measurements to derive the probability distribution function for extreme wind speeds.

Another significant aspect is atmospheric stability. In the surface layer, changes in temperature with height, and consequently, alterations in atmospheric stability are primarily caused by solar radiation from the Sun. The Sun's radiation reaches the Earth's atmosphere and is absorbed by the Earth's surface, resulting in its heating. The resulting infrared radiation from this heating is emitted towards the atmosphere from below, and since the atmosphere is mostly opaque to this infrared radiation, it absorbs it, further heating the atmosphere. Hence, it is the ground, not directly the Sun, that heats the atmosphere. Thus, during the day, heat is added to the atmosphere from below, leading to air rising and creating an unstable atmosphere due to convection. Conversely, at night, the opposite occurs, resulting in a stable atmosphere. True neutral conditions, where no heat is added to or removed from the atmosphere, only occur briefly around sunrise and sunset. In most cases, neutral atmosphere is assumed for simplification, and this model prove effective at higher wind speeds based on experimental evidence, which saves their accuracy (Landberg, 2015).

2.2.2 Wind profile

The instantaneous wind velocity at a height z can be decomposed into the time-averaged velocity $\overline{v}(z)$ and the fluctuating component $\tilde{v}(z,t)$ as in Eq.(2.3). The turbulent component of wind velocity has a mean value of zero and a standard deviation σ. Then, the peak value can be expressed using the standard deviation σ and the peak factor g:

$$v(z,t) = \overline{v}(z) + \tilde{v}(z,t) = \overline{v}(z) + g\,\sigma(z). \tag{2.3}$$

Wind speed fluctuations are accounted for through the turbulence intensity I_v, which is defined based on the standard deviation σ of wind speeds recorded during the specified averaging period:

$$I_v(z) = \frac{\sigma(z)}{\bar{v}(z)}. \tag{2.4}$$

The wind profile describes the relationship between the height above ground level and the corresponding horizontal wind speed. The average wind speed increases with increasing height above the ground (but the rate of change of the wind speed decreases with height), starting from zero due to the no-slip condition. (Figure 2.3.) The obstacles have significant influence on the flow near the surface. This effect causes the reduction of the wind velocity and introduce random vertical and horizontal velocity components at right angles to the main direction of flow. The vertical distribution of horizontal average wind speeds within the atmospheric boundary layer can be described with the help of the empirical power law or the semi-empirical log wind profile. Furthermore, there are lot of real wind profiles in addition to the two classics, e.g., Leipzig profile (Lettau, 1950; Mildner P., 1932) and Høvsøre profiles (Peña et al., 2014).

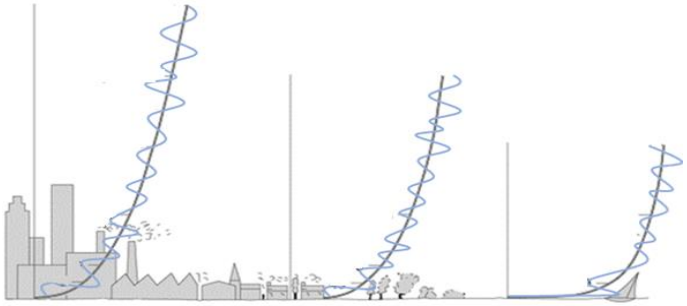

Figure 2.3. The vertical distribution of horizontal average and fluctuating wind speed for different terrain (Oke, 1987)

The equation to estimate the average wind speed v at height z above the ground is according to the log law:

$$v_z = \frac{u_*}{\kappa}\left[\ln\left(\frac{z-d}{z_0}\right) + \psi(z, z_0, L)\right], \tag{2.5}$$

where u_* is the friction velocity, κ is the von Kármán constant (~0.41), d is the zero-plane displacement (to lift the profile), z_0 is the surface roughness (in meters), ψ is a stability parameter for all atmospheric stabilities, L is the Monin-Obukhov length.

To obtain the wind profiles discussed, averaging is necessary due to the frequent fluctuations in wind speed. The wind profile varies between day and night, and also from season to season, primarily due to atmospheric stability. Liu et al. (2016) conducted an autocorrelation analysis of the variogram time-series for wind speed and identified the presence of a diurnal periodicity in the variogram time-series of a wind farm in Inner Mongolia Province. Hence, selecting the appropriate averaging time is crucial. An averaging period of 10 minutes to 1 hour is adequate to eliminate all the turbulent components of the atmospheric boundary layer (Harris and Cook, 2014). Standard practice of the World Meteorological Organization is to average over 10 minutes (WMO, 2021). Averaging times for basic wind velocity and wind-induced response differ across various codes and standards. For instance, ASCE, AS/NZ, ISO, and IWC standards define the basic wind speed as the 3 second gust speed, while other standards use an average wind speed (10-minute mean in AIJ, CNS, EU, and 1-hour mean in NBCC). However, all codes and standards employ a longer averaging period, such as 10 minutes or 1 hour, in the calculation of wind-induced response (Kwon and Kareem, 2013).

In EN 1991-1-4, the basic wind velocity v_b, which is defined as a function of wind direction and time of year at a height of 10 meters above the ground for terrain category II, can be calculated as follows:

$$v_b = c_{dir}\, c_{season}\, v_{b,0}, \tag{2.6}$$

$$v_m = c_r(z)\; c_o(z)\; v_b, \tag{2.7}$$

where c_{dir} is the directional factor for various wind directions and set to 1.0, c_{season} is the season factor and set to 1.0, v_{b0} is the fundamental value of the basic wind velocity which is the characteristic 10-minute mean wind velocity, irrespective of wind direction and time of the year, at 10 m above ground level in open country terrain with low vegetation. The roughness factor c_r, and orography factor c_o are taken as 1.0. The roughness factor c_r takes into consideration how the mean wind velocity at the structure's site varies with the height above ground level and the roughness of the terrain upwind of the structure in the relevant wind direction and it is calculated by:

$$c_r(z) = 0.19 \cdot \left(\frac{z_0}{z_{0,II}}\right)^{0.07} \ln\left(\frac{z}{z_0}\right), \tag{2.8}$$

where z_0 is the roughness length, and $z_{0,\mathrm{II}}$ is 0.05 m (terrain category II).
The relationship of the peak velocity pressure $q_\mathrm{p}(z)$ and the basic velocity pressure q_p, corresponding to 10-minute averaging time, can be described by the exposure factor:

$$c_e(z) = \frac{q_p(z)}{q_\mathrm{b}}. \tag{2.9}$$

2.2.3 Wind measurement

The currently applicable Eurocode (EN 1991-1-4, CEN, 2005) lacks any recommendations for installing wind measurement equipment or deriving wind speed model parameters from measurements. However, the forthcoming second generation EN 1991-1-4 will include guidance on these aspects, covering the derivation of basic wind velocity from measurements at meteorological stations, the use of probabilistic models for wind actions, and the incorporation of design parameters from wind tunnel tests and numerical simulations.

Most wind energy practitioners commonly refer to the IEC 61400-50-1:2022 (IEC, 2022) international standard, which provides detailed recommendations for mounting instruments on meteorological masts. The positioning of the anemometer should aim to minimize flow distortions, particularly those caused by the mast and boom. The measuring system shall include at least a top-mounted anemometer and a control anemometer. The top anemometer cups should be at least 1.5 m above the tower and no parts, i.e., sources of disturbance, should extend outside of an 11:1 half-cone whose vertex is coincident with the anemometer cup. Regardless of the mounting arrangement, the boom structure shall be adequately stable to prevent notable vibrations. Careful consideration should be given where the mast is of large cross-sectional area and consequently a side-mounted anemometer is subject to more significant tower interference effects. At a distance of 20 boom diameters, the influence of a round tubular beam is 0.5 %. An anemometer operating in the wake of the mast is highly disturbed, therefore it may not be allowable to use wake-effected measurements. However, the correction of flow distortion is permitted and described. Minimum distortion is obtained when the flow direction is perpendicular to the mast face and the anemometer is placed at an angle of 90° to the flow direction.

One of the reliable and robust instruments for measuring wind speed is the cup anemometer, which is also used in the monitoring system, discussed in Section 3.1. It

operates without the need for external power, as it harnesses the airflow's movement to rotate the cups, which, in turn, drives a small electric generator. The generator produces a voltage that can be converted into a wind speed measurement. There is a slight time delay before the cups of the anemometer reach the wind-forced rate, causing a lag. However, this lag is not symmetrical for wind speed increases and decreases. The cups take longer to slow down due to inertia, leading to a bias known as over-speeding. Consequently, the mean speed recorded is slightly higher than the actual wind speed. The extent of this over-speeding varies based on the cup anemometer design, and it is possible to minimize this effect through appropriate cup design. Moreover, dealing with icing on instruments like the cup anemometer can be challenging. One common method to address this issue is by using heated instruments.

2.2.4 Extreme wind velocity model

The basis of wind loading in each standard is the value of fundamental basic wind velocity $v_{b,0}$. In the Eurocode, it is defined as the characteristic value corresponding to the 0.98 quantile, which is equivalent to a mean return period of 50 years of the annual extreme value distribution of 10-minute mean wind velocities at 10 m above ground of terrain category II, irrespective of wind direction (EN 1991-1-4 2005). Nevertheless, the stochastic modelling of the fundamental basic wind velocity $v_{b,0}$ is an open issue, even now.

According to the classical extreme value theory (Fisher and Tippett, 1928; Gnedenko, 1943), the distribution of extreme events x has an asymptotic limit, now universally known as the generalized extreme value, GEV, distribution with shape ξ, scale σ and location μ parameters (Eq. (2.10)).

$$F_{\xi,\sigma,\eta}(x) = \begin{cases} \exp\left(-\left(1+\dfrac{\xi(x-\mu)}{\sigma}\right)^{-\frac{1}{\xi}}\right) & \text{for } \xi \neq 0, \\ \exp\left(-\exp\left(-\dfrac{(x-\mu)}{\sigma}\right)\right) & \text{for } \xi = 0. \end{cases} \tag{2.10}$$

Three types of the GEV family can be distinguished based on the shape parameter ξ value, i.e., Gumbel ($\xi = 0$), Fréchet ($\xi > 0$), and Weibull ($\xi < 0$), also known as type I, II, and III extreme value distributions, respectively. The Fréchet distribution has a

lower limit and the Gumbel distribution is unlimited which results unlimited values as the return period increases. The Probabilistic Model Code (Joint Committee on Structural Safety (JCSS), 2001) recommends the use of the Weibull distribution to represent $v_{b,0}$ in Europe. While the Gumbel distribution predicts unlimited wind velocity as the return period increases, the Weibull distribution may be more appropriate for modelling extreme wind speeds based on geophysical reasons (Cook and Ian Harris, 2001; Holmes and Moriarty, 1999, 2001; Lechner et al., 1992; Lee et al., 2017). However, due to the limited amount of available data, there is a risk of obtaining unreasonable Weibull parameters and predictions for extreme wind velocities. In other words, the estimated shape parameter of Weibull distribution may be subject to high statistical uncertainty, potentially leading to unreasonable values (Baravalle and Köhler, 2018). Consequently, in Hungary, the value of the fundamental basic wind velocity has been conservatively determined in the National Annex, employing the Gumbel distribution.

Cook (2019) has emphasized the challenge of finding a single-component distribution that universally represents wind climates, as different mechanisms contribute to these climates. Previous studies focused solely on wind speed PDFs, relying on statistical indicators like the coefficient of determination (R^2), root-mean-square error (RMSE), Chi-squared χ^2, and the Kolmogorov-Smirnov test to determine the best-fitting distribution empirically rather than a physics-based model. Cook have introduced the Offset Elliptical Normal (OEN) mixture model, supported by a global analysis of 128 stations. It is based on the concept that mean wind speed at a particular site and time is a result of various statistically independent causes, allowing the application of the Central Limit Theorem, allowing the problem to be modelled in terms of normally distributed random variables. The OEN model may provide a physically plausible representation of joint and marginal wind speed and direction distributions, offering a promising approach to modelling wind climates.

The techniques available for determining the characteristic wind speed for a 50-year return period were reviewed and summarized in the works of Palutikof et al. (1999) and Cooley (2016). The traditional method to derive extreme wind speeds is the Annual Maximum (AM) approach when GEV distribution is fitted to yearly maxima. It has a great advantage that solely few decisions are required during the calculation of the distribution parameters. Nevertheless, the main drawback is the considerable data

reduction, i.e., a significant amount of information contained in the weather data is not taken into account in the analysis. Therefore, wind measurement must be long, at least 10-20 extremes should be used to determine reliable results (Cook, 1985). To improve the efficiency, three main techniques have been developed: block method, peaks-over-threshold (POT) method (Baravalle and Köhler, 2018; Coles, 2001; Cook, 1982), and method of independent storms. This study primarily concentrates on the POT method, as it incorporates the most data, i.e., it involves the least amount of data reduction.

2.2.5 The peaks-over-threshold (POT) method

The POT method is based on a conditional distribution, i.e., the exceedances over a specified threshold. The generalized Pareto distribution (GPD) is the asymptotic distribution to model the tails of the GEV distribution under certain condition (Pickands III, 1975). Several papers deal with the application of GPD to extreme value analysis (Cook and Harris 2001; Holmes and Moriarty 1999, 2001; Pickands III 1975; Kang and Song 2017). The cumulative distribution function (CDF) of GPD:

$$F_{\xi,\sigma,\eta}(x) = \mathrm{P}\{X\text{-}u \le x \mid X > u\} = \begin{cases} 1\text{-}\left(1+\dfrac{\xi_1\left(x\text{-}\mu_1\right)}{\sigma_1}\right)^{-\frac{1}{\xi_1}}, & \text{for } \xi_1 \neq 0, \\ 1\text{-}\exp\left(-\dfrac{x\text{-}\mu_1}{\sigma_1}\right), & \text{for } \xi_1 = 0, \end{cases} \tag{2.11}$$

where u is the selected threshold; ξ_1, σ_1 and μ_1 are the shape, scale and location parameters of GPD, respectively. The shape parameter ξ_1 of the GPD is the same as for the GEV distribution (Pickands III 1975). The GEV and GPD parameters have the following relationship (Coles, 2001):

$$\sigma_1 = \sigma + \xi\left(\mu_1 - \mu\right). \tag{2.12}$$

The selection of the threshold and a minimum separation distance between extremes have strong impact on the result, and it is a compromise between bias and variance. While choosing a lower threshold can reduce variance, it may also bias the estimation if it is not a true extreme in an epoch. However, the bias decreases and the variance increase with higher threshold (Holmes and Moriarty, 1999). Procedures of threshold selection on visual basis are widely used, e.g., mean excess plot or mean residual life plot, which involves plotting the average of the excesses over the chosen wind velocity threshold against the threshold itself. The conditional distribution is in the domain of

attraction of the GPD if the mean excess plot follows a straight line. This requires subjective interpretation of the plot, which can introduce associated errors (Coles, 2001). Therefore, a pragmatic automated, simple and computationally inexpensive threshold selection technique has proposed by Thompson et al. (2009).

Six estimation methods for GPD parameters and extreme quantiles were studied and compared in the research conducted by Kang and Song (2017). Two methods were based on the maximum likelihood estimation (MLE), three on the Nonlinear Least Squares (NLS) and the last one utilized the Hill estimator. They observed that the MLE outperforms the other methods in most cases. However, it is essential to note that the MLE is only valid when $\xi > -0.5$, as stated by Cooley (2016).

2.3 Bayesian inference

From a meteorological point of view, it is evidently advantageous to encompass the complete spectrum of extreme variability, which might require a long time series. However, the analyst might be constrained by having only a limited number of years of available data. To extend the available dataset and resolve the problem, several strategies have been developed. One approach is the method outlined in the European Wind Atlas (Troen and Petersen, 1989), which extrapolates wind data from one location to another, primarily for wind energy estimation. This extrapolation incorporates considerations of terrain features as well as local factors such as roughness and shelter in the siting area (Palutikof et al., 1999).

Gatey and Miller (2007) found a significant correlation in the 50-years return period wind speeds among inland stations. The method, proposed by Pop et al. (2016), estimates Gumbel distribution parameters for wind gust speeds at stations, establishes a relationship with general wind climate, and applies it to existing wind climate maps. This approach shares similarities with the IEC (2005) technique.

Bayes' rule outlines how we can integrate information from on-site measurement data with prior information, obtained from wind data at different locations, to formulate the posterior distribution. First, uncertainty or the "degree of belief" is quantified using probability about the desired variables, forming the prior distribution. Subsequently, the observed data are employed to update the prior information or beliefs, resulting in updated posterior information or beliefs:

$$p(\boldsymbol{\theta}|D)=\frac{p(D|\boldsymbol{\theta})\,p(\boldsymbol{\theta})}{p(D)} \tag{2.13}$$

where D denotes the data, $\boldsymbol{\theta}$ is a vector denoting the set of parameters, $p(\boldsymbol{\theta}|D)$ is the posterior distribution, $p(\boldsymbol{\theta})$ is the prior distribution. The probability of the observed data, denoted as $p(D)$ and referred to as the marginal likelihood, can be determined through numerical integration. The concept of converting prior parameter information into posterior information can be extended indefinitely, facilitating probabilistic prediction and sequential updates. With the accumulation of additional information, typically through increased data collection, the Bayesian approach updates uncertainties associated with parameters and predictive distributions (Lee and Wagenmakers, 2013). A Bayesian-updated parameter vector $\boldsymbol{\theta}$ could include an extreme wind speed distribution parameter, as exemplified in the current research, where it is refined based on additional wind measurements D. Alternatively, the parameter might pertain to material characteristics, such as the compressive strength of a concrete cube, or a model parameter representing the rate of corrosion on a steel plate. In these cases, the parameter is updated through additional tests/measurements D or information derived from other calculation methods.

In the simulation study conducted by Fawcett and Green (2018), it was found that the posterior predictive return level yields more precise estimates of exceedance probabilities compared to estimative summaries of posteriors, such as the mean, mode, or 95% credible intervals. Moreover, even if an incorrect assumption regarding the temporal or spatial dependence of samples is made while using all excesses as in the study of Fawcett and Walshaw (2016), the posterior predictive return level still provides exceedance probabilities that align more closely with expectations compared to other estimative summaries. In addition, considering practitioners' preference for a single point summary that adequately accounts for estimation uncertainty, the adoption of the posterior predictive return level within the framework is deemed the optimal summary for practitioners.

2.4 Wind – structure interaction

2.4.1 Equivalent static wind load method

Another significant source of uncertainty in the wind-induced response of structures stems from the uncertain interaction phenomenon and its characterization. Estimating the expected peak values of wind-induced load effects and responses, such as deflections, bending moments, and support reactions, can be challenging, regardless of the presence of significant resonant dynamic response. Similar to how wind speed can be decomposed into its average speed and fluctuations (Eq. (2.1)), the structure's response can be decomposed into mean (time-averaged) and fluctuating components (Figure 2.4). The time-averaged response primarily aligns with the along-wind direction. The fluctuating response comprises an irregular and slowly varying component known as the "background response," as well as an oscillating component with distinct frequencies, termed the "resonant response". These fluctuations are observed both in the direction of the wind flow and perpendicular to it. Thus, the pulsating effect of wind vortices can induce a certain level of structural dynamic response, varying based on the dynamic properties of the structure (Davenport, 1993).

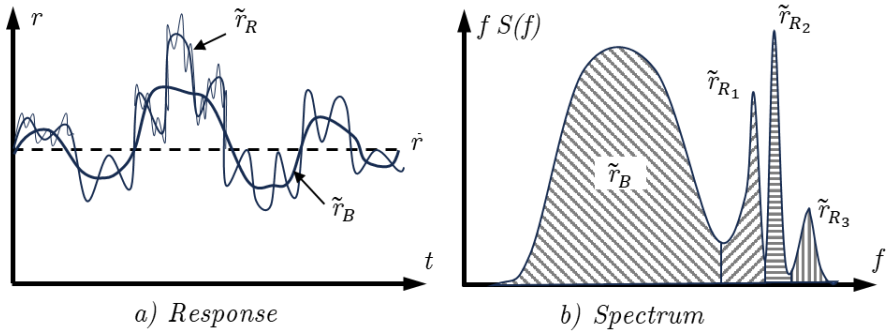

Figure 2.4. Characteristic of fluctuating response of structures (based on Davenport (1993))

In the 1960s, a simplified approach to wind-induced dynamic response was introduced, employing a 'gust response factor'. This alternative approach is presenting wind loading through equivalent static load distributions, generating peak load effects rather than the effects themselves. This approach assumes that the equivalent static load distribution corresponding to the maximum response follows the same shape as the mean wind load distribution.

The peak response can be written in the following formula:

$$r = \bar{r} + g\sqrt{\tilde{r}_B^2 + \sum \tilde{r}_{R_i}^2}, \tag{2.14}$$

where $\bar{r}$ is the time-averaged response, $\tilde{r}_B$ is the root mean square (rms) of the background response, $\tilde{r}_R$ is the rms of the resonant response peak in the j^{th} mode of vibration and g is the statistical peak factor, generally in the range of 3 to 4.

This investigation focuses on the aerodynamic along-wind force $F(z,t)$ acting on the tower (Eq.(2.15)), which is influenced by the relative wind speed in relation to the structure's movement. For sufficiently rigid structures, the relative wind speed equals the oncoming wind speed. However, flexible structures experience motion, causing the relative wind speed to vary over time, depending on the difference between the fluctuating oncoming wind speed and the structure's speed.

$$F(z,t) = \frac{1}{2}\rho c_f(z) A[\bar{v}(z)+\tilde{v}(z,t)-\dot{x}(z,t)]^2, \tag{2.15}$$

where ρ represents the air density, which is 1.25 kg/m^3 at a temperature of 20 $^\circ$ C, c_f is the drag/force coefficient at z, A is the reference area, $\dot{x}$ is the time-dependent along-wind velocity of the building at elevation z. It is assumed that the structure is well-designed to avoid unfavourable aeroelastic responses when subjected to real extreme wind loads. Therefore, this investigation does not take aeroelastic effects into account, and it assumes that the structure is sufficiently rigid with $\dot{x} = 0$. The equivalent static method in EN 1993-3-1 includes an allowance for the dynamic amplification of response that is typical of the majority of towers which are simple and regular structures, provided that the stiffness and mass proportions adhere to the criterion specified in Eq. (3.13). If the tower exhibits complex geometry, irregularities, or dynamic characteristics that significantly deviate from standard assumptions, or categorized as having higher importance, a more sophisticated dynamic analysis may be necessary.

The peak velocity pressure acting on the structure, also known as dynamic pressure, is the kinetic energy per unit volume of a fluid particle. In the context of incompressible fluids, dynamic pressure is quantified by the expression provided in Eq.(2.16), and it can also be decomposed similarly to Eq.(2.1):

$$q(z,t) = \frac{1}{2}\rho\, v^2(z,t) = \frac{1}{2}\rho\left(\bar{v}^2(z) + 2\bar{v}(z)\,\tilde{v}(z,t) + \tilde{v}^2(z,t)\right). \tag{2.16}$$

The squared member of the fluctuation is negligible in comparison to the others, resulting in a linearized form of the peak velocity pressure:

$$q(z,t) = \frac{1}{2}\rho\,\overline{v}^2(z) + \frac{1}{2}\rho\,2\overline{v}(z)\,\tilde{v}(z,t) \;=\; \overline{q}(z) + \tilde{q}(z,\,t), \tag{2.17}$$

where $\overline{q}(z)$ is the mean velocity pressure and $\tilde{q}(z,\,t)$ is the fluctuations around the average. The peak velocity pressure can be described using the peak factor:

$$q(z,t) = \frac{1}{2}\rho\,\overline{v}^2(z)\left(1+2\frac{\tilde{v}}{\overline{v}}\right) = \overline{q}(z)(1+2gI_v). \tag{2.18}$$

While these assumptions are reasonably valid for smaller and straightforward cantilevered structures, it often produces results acceptable for the level of precision anticipated in wind loading codes or standards (Holmes, 2002). The equivalent static method considers an allowance for the dynamic amplification of response, particularly noticeable in higher tower panels, especially when accommodating concentrated ancillary items or using a concave outline profile.

2.4.2 Reynolds number

The value of the drag/force coefficient c_f in Eq. (2.15) depends on the fluid flow patterns around the structure, and these patterns can be predicted using the Reynolds number, Eq.(2.19):

$$\mathrm{Re} = \frac{v\,L}{\upsilon}, \tag{2.19}$$

where v is the is the flow velocity, L is a characteristic length, ν is the kinematic viscosity of the fluid. The Reynolds number Re is a dimensionless parameter that quantifies the relationship between inertial and viscous forces. Figure 2.5 illustrates a flow pattern around the cylinder. Notably, at Reynolds numbers below 4, there is no separation of the flow. Within the range of Reynolds numbers between 5 and 40, flow separation occurs, leading to the formation of a symmetric pair of vortices in the near wake. As the Reynolds number increases further, typically within the range of 80 to 200, the wake becomes unstable, and vortex shedding is initiated. Within the subcritical Reynolds number range of 300 to $3.5{\cdot}10^5$, the laminar boundary layer separates approximately 80 degrees downstream from the front stagnation point, resulting in strong and periodic vortex shedding. With a continuous increase in Reynolds number, the flow transitions to the critical regime, characterized by a sharp decrease in the drag

coefficient. In the supercritical range ($Re > 3.5{\cdot}10^5$), regular vortex shedding is re-established, accompanied by a turbulent boundary layer on the tube's surface.

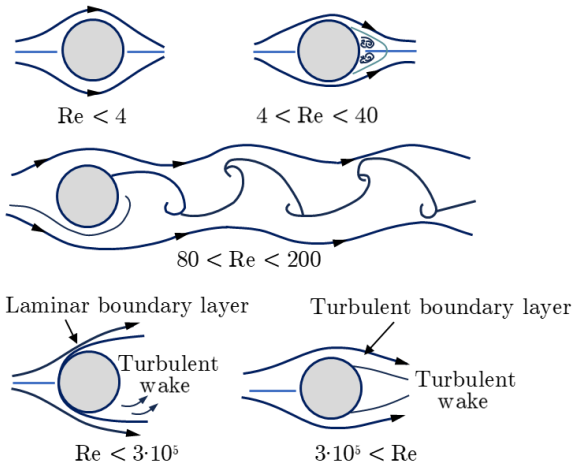

Figure 2.5. Flow patterns around a cylinder at different Reynolds numbers (Kundu et al., 2016)

2.4.3 Wind tunnel tests

Investigations (Georgakis et al., 2009; Koss and Srouji, 2015; Nielsen, 2019) including wind tunnel test on full-scale sections of a lattice mast configurations have shown that the drag coefficients of a mast section under smooth flow condition, or for low velocities, are underestimated, while the drag coefficients corresponding to high wind velocity and turbulent flow conditions are overestimated in EN 1993-3-1 (2006). The full-size mast structure, i.e., prototype, was also tested at a reduced scale of 1:6 in 2008 (Georgakis et al., 2009). These tests were conducted in two different flow conditions: one with a smooth flow characterized by a longitudinal turbulence intensity of 1.1%, and the other with turbulent flow featuring a turbulence intensity of 9.6%. A replica of a scaled mast design, which had been originally tested by the National Maritime Institute (NMI) in the UK in 1977, was included in this study. Reconstructing the NMI tests provides valuable insights into the model's design and allows for consideration of scaling effects in the results. In Figure 2.6, the results for turbulent flow are presented, comparing the predicted aerodynamic drag coefficient from wind tunnel tests with calculated values based on NMI, EN 1993-3-1, and the Engineering Science Data Unit (ESDU) standards. EN 1993-3-1 distinguishes between circular members in the subcritical and supercritical range, defining the transition at $Re = 4{\cdot}10^5$ while conservatively omitting the critical range. Both full-size and scaled wind tunnel

tests show drag coefficients entering the critical range with the expected aerodynamic drag coefficient C_D decrease as Reynolds numbers increase. Some standardized data seem to reflect model-scale force coefficients more than full-scale behaviour. This prompts the need, from a codification perspective, for a conservative envelope curve to account for such uncertainties. Given the industry's aim to save resources and costs through precise load data, determining the Reynolds number at which drag coefficients drop becomes a significant challenge.

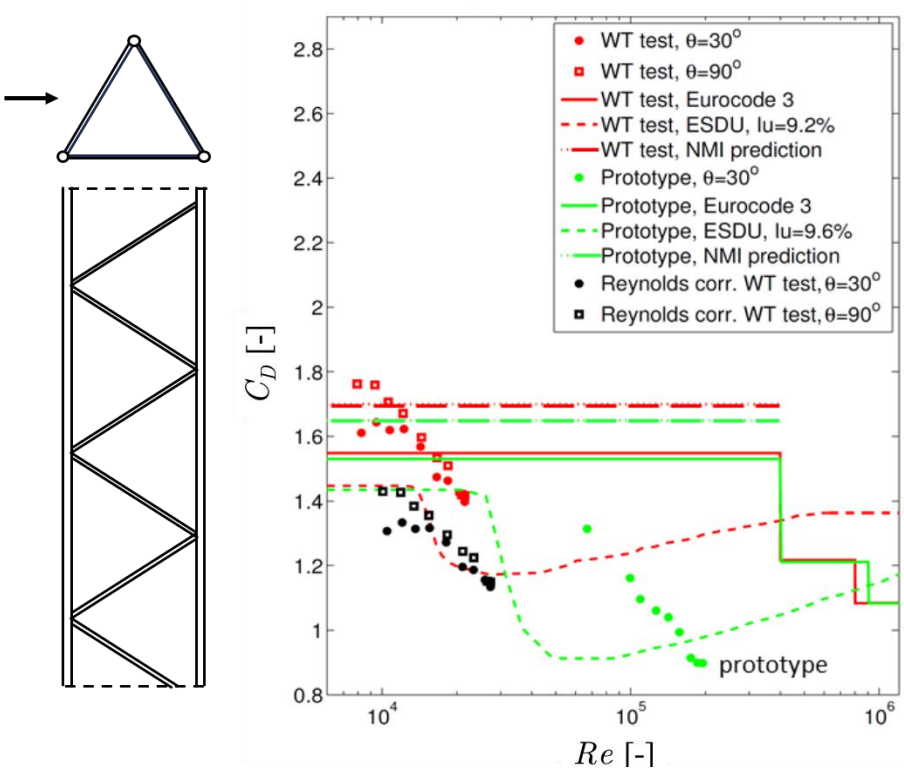

Figure 2.6. The mast tested at reduced scale (WT) in turbulent flow, the full size (prototype) study and estimated drag values from literature and codes corresponding to the scaled and full size masts (Koss and Srouji, 2015)

Hence, drag coefficients derived from scaled tests in the UK in the 70's, might need to be re-examined and further full-scale wind tunnel tests and computational fluid dynamics simulations are required. Calotescu et al. (2021) conducted wind tunnel tests on a 1:5.7 scale sectional model of a telecommunication lattice tower to analyse the influence of linear and discrete ancillary elements on aerodynamic coefficients. The test models had circular cross-sections for leg members and angle or circular cross-sections for bracing elements. It was observed that angle cross-section bracings lead to larger

drag and lift coefficients than circular cross-sections. Moreover, the angle of attack yielding the highest drag coefficients is insignificant for the test of bare models, as their drag coefficients remain relatively constant. However, this angle becomes significant when testing models equipped with ancillaries.

On the other hand, Balczó et al. (2006) performed wind tunnel tests and computational fluid dynamics (CFD) simulations on a mast section that is being investigated in the presented study. These tests involved a bare mast section with a triangle cross-section with width of 1300 mm and a length of 1600 mm, constructed using hot-dip galvanized circular hollow sections with diameters of $D = 108$ mm for chord members and $D = 75$ mm for the bracing members. In comparison to the wind force calculated according to EN 1993-3-1, Balczó et al. observed a lower wind force. This finding also indicates that the formulae in EN 1993-3-1 tend to overestimate the drag coefficient of the mast section at high wind velocities and turbulence intensities.

Furthermore, major international wind codes and standards were compared in previous studies to identify the differences and similarities between them (Gatey and Miller, 2007; Kwon and Kareem, 2013; Lungu et al., 1996). One of the main conclusions is that alongwind responses are fairly consistent in the codes/standards but there are discrepancies in acrosswind responses. Moreover, most of these codes use the global method, i.e., the solidity ratio and global shielding factors. The solidity ratios are calculated as:

$$\phi = \frac{A_S}{A_C}, \tag{2.20}$$

where A_S is the sum of the projected area of the members of the face projected normal to the face corresponding to each angle of attack, and A_C is the area enclosed by the boundaries of the face projected normal to the face, as depicted in Figure 2.7.

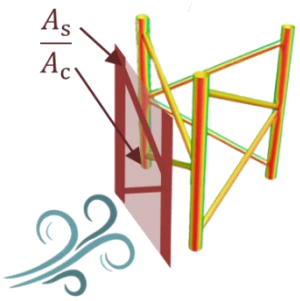

Figure 2.7. Projected panel area used to calculate solidity ratio ϕ

Although this approach is very effective for conventional structures, it is difficult to apply for atypical configurations. As recommended by Prud'homme et al. (2018), an empirical local method could be used to determine the wind loads in such a case. Their approach is based on the reduction of wind velocity in a turbulent wake and account the shielding effect on each member.

Therefore, specifically, for the equivalent static method, the drag coefficient and the gust response factor play key roles.

2.5 Structural behaviour and analysis

Numerous papers have been published focusing on lattice tower performance, involving full-scale tests and/or numerical studies. Lu et al. (2016) examined the behaviour of a steel lattice transmission tower. Their findings highlighted that the dominant failure mode was buckling in the compressive legs, with failure initiating in the lower part due to elastic buckling of a bracing member. This subsequently triggered buckling of the main diagonal bracing member, inducing compression leg buckling and ultimately causing the tower to collapse. However, as reported in the study of Ducloux and Figueroa (2016), the structural behaviour and response of a tangent suspension tower and a radio tower are quite different.

Bezas et al. (2022) have demonstrated that the current version of EN 1993-3-1 does not adequately address the buckling instability mode known as segment instability, which involves the buckling of multiple members.

In this study, finite element method (FEM) based PBWE assessment of a telecommunication steel lattice tower located in Central Hungary is presented. Reliability analysis and FEM-based investigation can be conducted to assess risk and determine damage grades in situations where the use of partial safety factors from Eurocode standards is not applicable or efficient, such as in the case of corroded members (Kövesdi et al., 2022). Currently under development, the new standard prEN 1993-1-14 (2020) aims to establish design rules for the FEM-based design of steel structures. The integration of site-specific wind loading models into the standardized FEM-based design will prove to be a powerful tool for design engineers.

3 Materials and methods

3.1 Lattice mast in Sződliget - case study

An investigation is conducted on a freestanding telecommunication lattice tower located in the suburban area of Sződliget, Central Hungary, utilizing the PBWE framework. The lattice mast has a total height of 49.70 m and triangular cross-section. Width of the structures varies along the vertical direction, the maximum width at the bottom is 4.80 m, while it is reduced to 3.00 m at the top. Both the chord members and bracings have circular hollow sections with various diameter (76 - 159 mm) and wall thickness (2.9 - 12.5 mm); structural steel grade is S235. Cross-sectional dimensions and section types are presented in detail in Section 3.7 and in Figure A.1 in the Appendix. Main dimensions of the structure are shown in Figure 3.1. The tower is equipped with linear ancillaries, i.e., with ladder and cables, and a total of 23 sector and microwave antennae are installed. Details of the antennae are summarized in Table A.1 and Figure A.2 in the Appendix. Antenna numbering, section numbering (divisions shown in Figure 3.1 for wind load calculation), notations for face numbering (shown in Figure 3.2a), antenna type and total antenna area A_{ant} are listed in this table. For sector antennae, multiplication factors of 1.1 and 1.5 are used for taking the projected area of anchorage ancillaries into account as a conservative assumption.

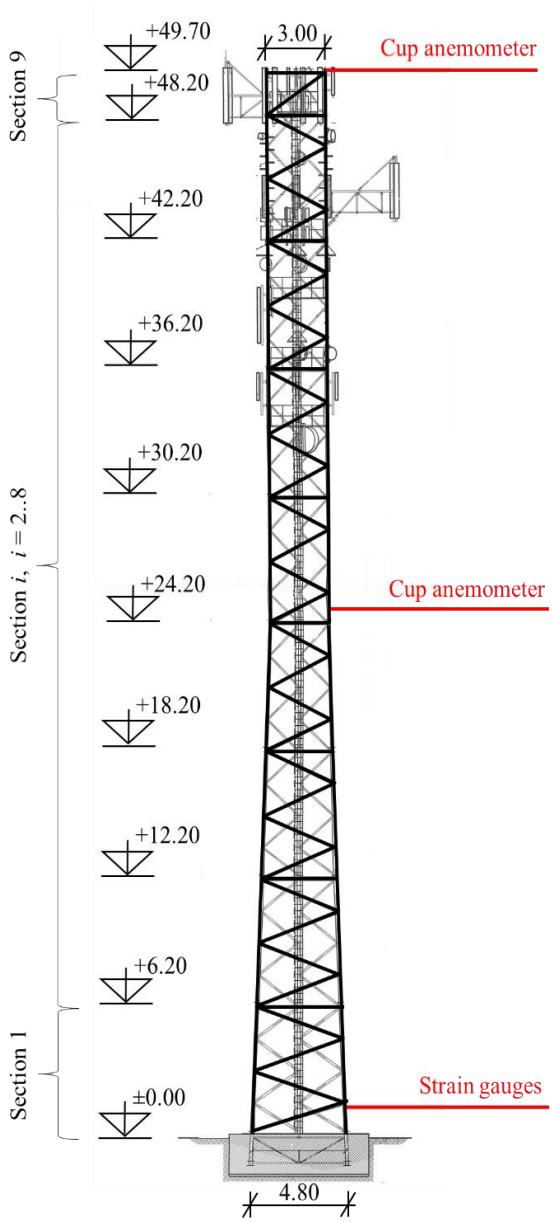

Figure 3.1. Main dimensions of the analysed telecommunication mast in Sződliget, Central Hungary

Force coefficient $c_{f,A,0}$ for the antenna appropriate to the wind direction and wind speed is obtained from wind tunnel tests provided by the manufacturer. Minimum and maximum wind directions α_{min} and α_{max}, respectively are listed in the Table A.1 where each antenna is taken into consideration in the wind load calculation. Vertical position Z of each antenna is summarized as well. Notations for wind direction α and chords with O159×13 tubular cross section (S_1, S_2 and S_3) are shown in Figure 3.2a.

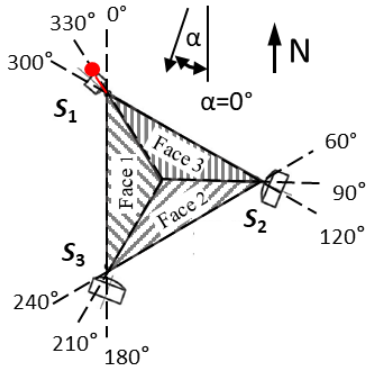

a)

b)

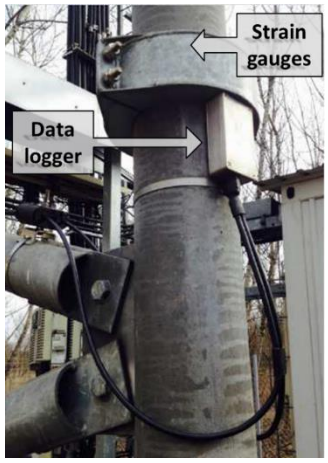

c)

Figure 3.2. a) notations of wind direction α and chords (S_1, S_2 and S_3); b) cup anemometer at the middle of the tower; c) detail of a chord with strain gauges

The tower is equipped with cup anemometer wind speed sensors, an air thermometer, and strain gauges to measure its response. The wind speed was measured for the period between August 2011 and March 2015 with a sampling rate of 0.9 s at the middle and the top of the lattice tower, i.e., 25 m and 49.70 m above ground level. Since cup anemometer wind speed sensors have been used, the measured wind speeds have a duration of at least 2 seconds. The anemometers used for measurement have a measuring range of 1-67 m/s for wind velocity and 0-360° for wind direction. The accuracy of the measurements is within 5% for wind velocity and ±7° for wind direction. The resolution of anemometers is 0.1 m/s for wind velocity and 1° for wind direction. Since wind speed sensors is installed directly on the chord member of the mast at the height of 25 m (Figure 3.2b), the data undergoes filtering to exclude wind directions ranging from 60° to 270° for the calculation of the roughness length. Additionally, filtering is performed to discard invalid data, such as those affected by icing (minimum temperature of 1°C) or incorrect data recording, such as timeouts, read errors, memory

write errors, out-of-memory events resulting in data loss, and warm-up errors. The measuring device labels the incorrect measurement data, providing a basis for subsequent filtering. Full-bridge strain gauges, with temperature compensation, are installed on chord members at 4.8 m above ground level (Figure 3.2c).

Because of Hungary's geographical position, the prevailing wind direction is from the northwest, while southerly winds showing a secondary maximum. The lattice tower is located in the suburban area of Sződliget, on the south-eastern side of the town (Figure 3.3). Thus, the north-western area is characterized by dense urban development, featuring buildings and trees that are 6-10 meters in height. The terrain category falls between EN 1991-1-4 terrain categories III and IV. This classification suggests a recommended roughness coefficient ranging between 0.3 and 1, which is a wide range.

Figure 3.3. Map and terrain category of Sződliget

3.2 Observations of the Hungarian Meteorological Service

Furthermore, in line with European Union directives, the Hungarian Meteorological Service (HMS) will make its observation and measurement data (from 2002 onwards) freely available for use via an open data server (https://odp.met.hu/) from 1 January 2021. The map with the locations of the wind measurement meteorological stations used in the research is shown in Figure 3.4.

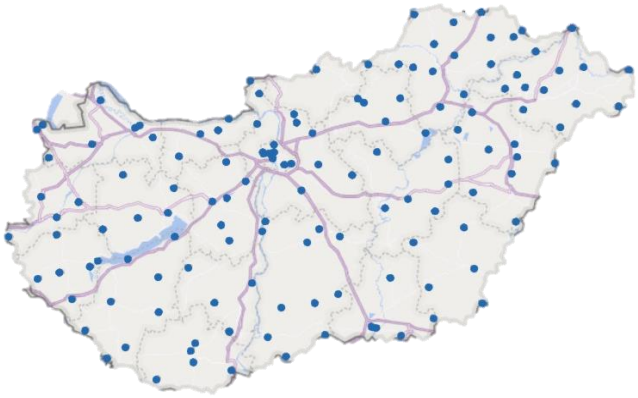

Figure 3.4. Meteorological stations of Hungarian Meteorological Service (HMS)

In this way, the information from Sződliget will be enhanced by incorporating measurement data series from various locations across the country. This approach assumes that the wind environment will remain constant over a large spatial scale (100-1000 km). This assumption is generally valid for flatlands and plateaus, where strong wind events are typically macro-scale or meso-scale occurrences (e.g., Hungary). Annual maximum wind velocity data have been collected from 169 stations, and among these, 67 stations possess a minimum of 20 years of data. The annual maxima are derived from the 12 measurement extremes over a one-month period. At the meteorological measurement stations, recorded wind gust speeds up to 2 seconds, as well as the 10-minute average wind speeds, are accessible. Alternatively, the possibility of augmenting the information from Sződliget with wind data obtained from the nearest HMS meteorological station, Penc, is being considered (Figure 3.5).

Figure 3.5. Map and terrain category of Sződliget and Penc

The following cases have been examined, and the corresponding notation system is provided in the following table, Table 3.1:

Table 3.1. Cases under investigation and their notations

Notation	Description
Sződliget GPD	GPD distribution fitted to the data series of Sződliget.
Hungary - peak	GEV parameters are calculated using the mean and standard deviation derived from the HMS Hungarian wind gust measurement data series, in accordance with the EN 1991-1-4 Hungarian National Annex.
Hungary - 10 min	GEV parameters are calculated using the mean and standard deviation derived from the HMS Hungarian 10-minute mean wind measurement data series, in accordance with the EN 1991-1-4 Hungarian National Annex.
Hun - Sződliget	Utilizing the GEV distribution of the "Hungary - 10 min" case as the prior distribution and employing Bayesian updating with the Sződliget dataset.
Hun - Kriging	GEV parameters related to Sződliget are derived from wind gust measurement data series through Kriging, a spatial interpolation technique.
Hun - Kriging - 10 min	GEV parameters related to Sződliget are derived from 10-minute mean wind measurement data series through Kriging, a spatial interpolation technique.
Hun - Kriging - Sződliget	Utilizing the GEV distribution of the "Hun - Kriging - 10 min" case as the prior distribution and employing Bayesian updating with the Sződliget dataset.
Penc - 10 min	GEV parameters are fitted to the 10-minute mean wind measurement data series of Penc using MLE.
Penc - Sződliget	Utilizing the GEV distribution of the "Penc - 10 min" case as the prior distribution and employing Bayesian updating with the Sződliget dataset.

3.3 The PBWE methodology

Advanced investigation on quantitative assessment of structural performance is carried out based on the PBWE framework shown in Figure 3.6. In this analysis, the uncertain relation between the mean and short-term fluctuation of wind speed is taken into account through the exposure factor c_e which is the product of the gust c_g and roughness factor c_r. Hence, these two factors are treated as random variables in this study. The roughness factor c_r describes the variation of the mean velocity pressure with height above ground and terrain roughness as a function of the reference velocity pressure. The gust factor c_g for velocity pressure represents the ratio of the peak velocity pressure to the mean velocity pressure of the wind. The *IM* and *SP* parameters are assumed to be independent and not correlated in this analysis.

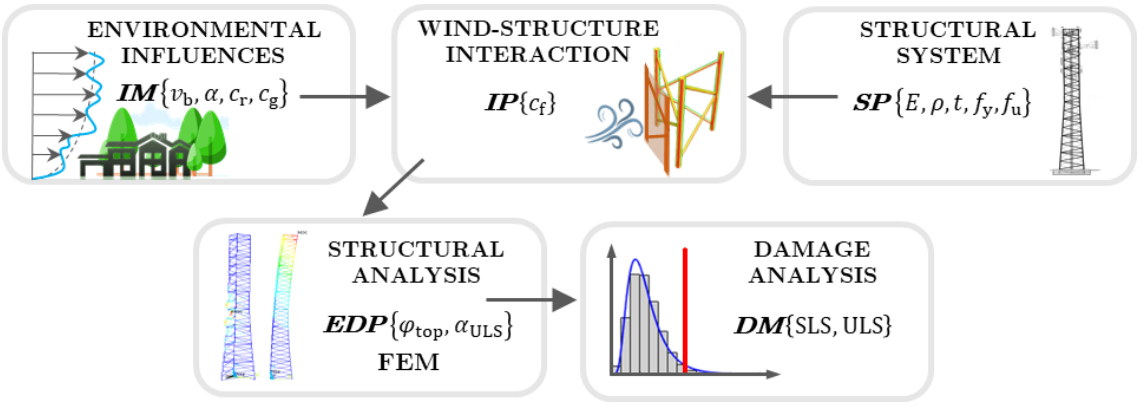

Figure 3.6. The implemented PBWE framework

The flowchart of the proposed analysing framework is depicted in Figure 3.7, where D denotes the data, σ_i and μ_i represent the scale and location parameters of the distributions of interest.

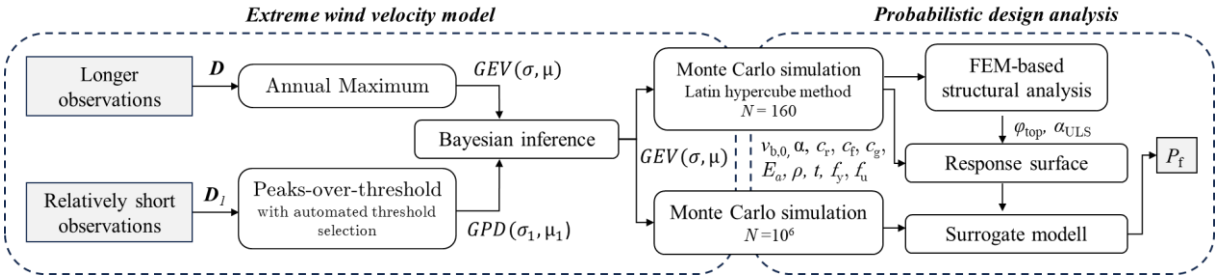

Figure 3.7. The flowchart of the proposed analysing framework

Eq. (2.2) is assessed using Monte Carlo simulation with random Latin hypercube sampling. Quadratic response surfaces are fitted for output variables, such as the rotation of the top of the mast φ_{top} for SLS, while load amplification factor α_{ULS}, i.e. the ratio of the ultimate capacity of the structure to the applied load, is used for ULS for response surface fitting. Monte Carlo simulations, with $N = 10^6$ simulation loops, are performed on the derived response surfaces to gain the distribution functions of EDPs and the probabilities of exceeding the targeted limit value.

The Probabilistic Design System (PDS) module of a general-purpose finite element software (ANSYS v19.0) is used for performing probabilistic calculations for both SLS criterion and load-bearing capacity for ULS. For high performance level, maximum allowable rotation of the top of the tower φ_{top} is defined as 0.5° as per the telecommunication service provider's specifications. A selection of probability design variables has been made, encompassing those with potential significant (e.g. c_f, c_r, c_g) or minimal effects (ρ, E_a) on the engineering demand parameter. Probabilistic design variables and the corresponding distribution functions and parameters are summarised in Table 3.2 for SLS and ULS simulations based on the recommendations of JCSS (Joint Committee on Structural Safety, 2001) and measurement results. A range of coefficients of variations (CV) values are defined in the probabilistic model code of JCSS for describing wind effects (c_f, c_r, c_g); the larger values are used in the stochastic analyses for dealing with uncertainties which results in conservative results. The probabilistic analysis is performed using Monte Carlo simulation with random Latin hypercube sampling which method ensures to have independent samples without accumulation of clusters of samples by having a memory of previous simulations. On the other hand, extreme ends of distribution functions are also considered in sampling process. A total of $n = 160$ samples is used in the simulation dividing each random input variable into intervals of equal probability ($p = 1/n$), while random sampling is carried out within each interval. Number of simulation loops, i.e., samples, required in a Monte Carlo simulation to fit a quadratic response surface depends on the number of random input variables. This sample size is chosen based on the number of probabilistic design variables, which is 9 for SLS and 11 for ULS, following the guidelines provided in the advanced analysis techniques guide of the software. The required sample

size for 9 and 11 random variables are 147 and 151, respectively. A sample size of 160 is chosen for each simulated scenario.

Table 3.2. Probabilistic design variables for PBWE

Limit state	Probabilistic input variable		Distribution function	Distribution parameters	
SLS and ULS	Wind direction α		Gaussian	$\alpha_{mean} = 299.719°$ $\sigma_\alpha = 18.621°$	see Section 4.2.1
	Fundamental basic wind velocity $v_{b,0}$ ($\xi = 0$)	Scale σ	Gaussian	see Table 4.3	
		Location μ	Gaussian	see Table 4.3	
	Force coefficient c_f		Gaussian	$c_{f,mean}$ according to EN 1993-3-1 or wind tunnel test	CV = 0.15
	Roughness factor c_r		Gaussian	$c_{r,mean}$ according to EN 1991-1-4	CV = 0.20
	Gust factor c_g		Gaussian	$c_{g,mean}$ according to EN 1991-1-4	CV = 0.17
	Young's modulus E_a		Lognormal	$E_{mean} = 210\,000$ MPa $\sigma_E = 0.03 \times E_{mean} = 6300$ MPa	
	Density ρ		Gaussian	$\rho_{mean} = 7700$ kg/m^3 $\times 1.05 = 8085$ kg/m^3 $\sigma_\rho = 0.01 \times \rho_{mean} = 80.85$ kg/m^3	
	Wall thickness t		Gaussian	$t_{mean} = t_{nom}$ (see Table 3.3) $\sigma_t = 0.05 \times t_{mean}$	
ULS only	Yield strength f_y		Lognormal	$f_{y,mean} = 235\text{MPa} \times 1.00 \times e^{2.0 \times 0.07} - 20\text{MPa} = 250.3\text{MPa}$ $\sigma_{fy} = 0.07 \times f_{y,mean} = 17.5$ MPa	
	Ultimate strength f_u		Lognormal	$f_{u,mean} = 1.5 \times f_{y,mean} = 375.5$ MPa $\sigma_{fu} = 0.04 \times f_{u,mean} = 15.0$ MPa	

It should be noted that ANSYS PDS module supports multiple distribution functions such as Gaussian, lognormal (LND), uniform, Weibull, etc. However, generalized Pareto and extreme value distribution function, describing the distribution of measurement data, are not among them. Therefore, the corresponding cumulative distribution functions are added manually in the macro file using inverse transform sampling.

Response surfaces are fitted for output variables for SLS for the rotation of the top node $\varphi_{top,}$ while load amplification factor α_{ULS} is used for ULS for response surface fitting. Forward-stepwise-regression model with linear and quadratic terms including cross-terms is used with confidence level of 0.95 for filtering out irrelevant terms of the model.

It leads to smaller number of coefficients resulting in increased accuracy of the remaining terms. In addition, Monte Carlo simulation is performed on the derived response surfaces in MATLAB environments. The simulations allow for fast calculations and evaluation of the *EDP*s using approximation functions. As a result, the probability distribution of the selected *EDP*s, namely φ_{top} and α_{ULS}, can be represented by a posterior predictive distribution. This distribution yields more accurate estimates of exceedance probabilities compared to estimative summaries of the posterior distribution of the extreme wind speed model, such as the mean, mode, or 95% credible intervals. The posterior predictive sampling is achieved by the Monte Carlo simulations with $N = 10^6$ simulation loops on the derived response surfaces and lognormal distribution is fitted on the outcomes. The probability of the exceedance of the limit state is assessed according to Eq. (3.1).

$$\Pr\{Y \leq \mathrm{y} \mid D\} = \int_{\boldsymbol{\theta}} \Pr\{Y \leq \mathrm{y} \mid \boldsymbol{\theta}\}\, \mathrm{p}(\boldsymbol{\theta} \mid D)\, \mathrm{d}\boldsymbol{\theta}, \tag{3.1}$$

where Y denotes EDPs, $\boldsymbol{\theta}$ is a vector indicating the parameter set of input stochastic variables.

After determining the probability of the EDP exceeding the specified limit, which is set at 0.5° for the maximum allowable rotation of the top of the tower φ_{top} for the SLS and 1 for the limit of the load amplification factor for the ULS, the reliability index β is selected and computed as a conventional measure of reliability by Eq.(3.2).

$$\beta = -\Phi^{-1}(P_{\mathrm{f}}), \tag{3.2}$$

where P_{f} is the probability of the *EDP* exceeding the specified limit, i.e., the probability of failure, Φ^{-1}denotes the inverse cumulative distribution function of Gaussian distribution.

3.4 Model of extreme wind velocity

3.4.1 Processing of long-period neighbourhood wind velocity measurements

The dissertation presents the Bayesian updating of wind velocity model parameters, which combines information from measurements collected at the site of the tower over a relatively short duration with a more extensive dataset from measurement locations across the country provided by the HMS. In utilizing the 20 year-long measurement

data series from the nearest station, Penc, as substantive prior information, MLE fitting is employed to evaluate the GEV parameters. In the "Hungary - peak" scenario, the parameters of the Gumbel distribution ($\xi = 0$) are calculated by utilizing the prior information provided by the measurement data series from all stations of the HMS. The mean of the σ and μ parameters of the Gumbel distribution can be calculated from the mean $\overline{V}_1$ and standard deviation (STD) s_1 of the annual maxima wind speed data as follows (Eqs. (3.3) and (3.4)):

$$\sigma = \sqrt{\frac{6\ {s_1}^2}{\pi^2}}, \tag{3.3}$$

$$\mu = \overline{V}_1 - \sigma\,\gamma, \tag{3.4}$$

where $\gamma = 0.577$, is the Euler–Mascheroni constant. The STD of the parameters are evaluated using the delta method, relying on the standard error of the mean (SEM) $s_{\overline{V}_1}$ and STD s_{s_1} (Ahn, S. and Fessler, 2003), as shown below (Eqs. (3.5) and (3.6)):

$$s_{\overline{V}_1} = \frac{s_1}{\sqrt{n}}, \tag{3.5}$$

$$s_{s_1} = \frac{s_1}{\sqrt{2(n\text{-}1)}}, \tag{3.6}$$

where n is the number of observations.

After that, the characteristic wind gust speed lasting a few seconds can be directly computed based on the estimated parameters as the characteristic value corresponding to the 0.98 quantile. However, according to clause 4.2(1)P of EN 1991-1-4, the fundamental basic wind velocity $v_{b,0}$ shall be determined on the basis of the 10-minute average wind speed. For the conversion, the exposure factor $c_e(z)$ in paragraph 4.5(1) of the standard, with a value of 2.352 for terrain category II at a height of 10 m above ground level, can be applied. The square root of this value is then applied to the wind velocity, allowing the fundamental basic wind velocity to be calculated in accordance with the Hungarian National Annex as follows (Eq. (3.7)):

$$v_{b,0} = \frac{v_{98}}{\sqrt{2.352}}. \tag{3.7}$$

After determining the fundamental base wind speed $v_{b,0}$, the EN 1991-1-4 is used to calculate both the base wind speed v_b and the average wind speed v_m by Eqs. (2.6)-(2.7). This process was applied consistently to both the HMS dataset and Sződliget dataset.

In the "Hun - Kriging" scenario, the Kriging spatial interpolation technique is used to model and estimate GEV parameters at unsampled locations, i.e. at Sződliget, based on HMS measurement points. The method leverages the spatial correlation and covariance structure between observed data points, allowing for the creation of a predictive spatial distribution model. The DACE (Design and Analysis of Computer Experiments) MATLAB Kriging Toolbox (2002) is employed, utilizing a second-order polynomial regression function with a cubic correlation function, to construct the Kriging approximation model. The HMS meteorological measurement points are divided into two groups for the training and validation datasets to optimize the parameter of the correlation function. Only one split is performed and analysed, and the correlation function parameter with the smallest mean squared error at validation points is selected.

3.4.2 Processing of short-period neighbourhood wind velocity measurements

The wind velocity data points, averaged over a 10-minute interval, are extracted from the wind velocity record. Since the time series of wind velocity exhibits memory, the initial step involves conducting an autocorrelation analysis to ascertain dependencies among the data and identify statistically independent events.

The logarithmic wind velocity profile is then employed to estimate the wind velocity at a height of 10 m:

$$v(z) = \frac{u_*}{0.4} \ln\left(\frac{z}{z_0}\right) v_{b,0}, \tag{3.8}$$

where u_* is the friction velocity, z is the height of interest, z_0 is the roughness length, $v_{b,0}$ is the fundamental basic wind velocity. Emphasizing the importance, it should be noted that wind information, such as basic wind speed, wind profile, terrain conditions, turbulence intensity, etc., obtained from a standard may frequently deviate from the actual conditions observed at the site. This discrepancy can introduce sources of epistemic or model/load uncertainty when assessing the effects of wind loading on structures. In this study, the roughness length is determined based on the measured

wind velocities at heights of 25 m and 50 m utilizing the logarithmic profile for wind speed averages greater than 10 m/s where the averaging period is 10 minutes. The wind speed threshold of 10 m/s corresponds to a height of 25 m.

As reported in the literature, when statistical uncertainty is neglected, the GPD distribution with a negative shape parameter consistently provides a better fit to the data compared to the shape parameter of zero, due to the third additional parameter. This implies that the distribution tail converges toward a limit value, establishing a right-bounded domain (Baravalle and Köhler, 2018). However, due to the limited amount of available data, there is a risk that the estimated shape parameter may exhibit high statistical uncertainty, potentially resulting in unreasonable predictions for extreme wind velocities. For this reason, and to facilitate the update of the scale σ and location μ parameters of the GEV distribution with a bivariate normal distribution in the Bayesian update process, the shape parameter ξ is set to zero. Hence, the value of the fundamental basic wind velocity has been conservatively determined.

3.4.3 The POT method

The POT approach is implemented to determine the parameters of the distribution of the extreme wind speeds at Sződliget, due to the relatively short length of available measurement data series. The automated threshold selection technique, proposed by Thompson et al. (2009) and described in Eqs. (3.9) and (3.10), is applied in this study and verified using conventional graphical diagnostics. According to their recommendations, suitable values of equally spaced candidate thresholds u_j should be chosen for the automated threshold selection between the median and the 0.98 quantile of the dataset, unless fewer than 100 values exceed this value, in which case the upper bound should be set to the 100^{th} data value in descending order. Let define

$$\tau_{u_j} = \hat{\sigma}_{u_j} - \hat{\xi}_{u_j} u_j, \qquad j = 1 \dots n. \tag{3.9}$$

The differences

$$\tau_{u_j} - \tau_{u_{j-1}}, \qquad j = 2 \dots n, \tag{3.10}$$

should approximately follow normal distribution with mean value of zero. The Pearson's Chi-square test is applied as a goodness-of-fit test, and the threshold with the lowest value is selected to satisfy this condition. This technique aligns with

Coles (2001) that the reparametrized scale parameter should remain constant beyond a valid threshold for excesses to follow the generalized Pareto distribution.

The parameters of the GPD, along with their STD are assessed, and the estimation uncertainty of the parameters is taken into consideration in the probabilistic model (Figure 3.7). For data analysis, including fitting probability distributions to data and conducting hypothesis tests, the MATLAB (R2022a) software is employed, the fitting of parameters for GPD distributions is performed using maximum likelihood estimation.

3.5 Bayesian inference

Flowchart of the POT method with Bayesian inference is depicted in Figure 3.8.

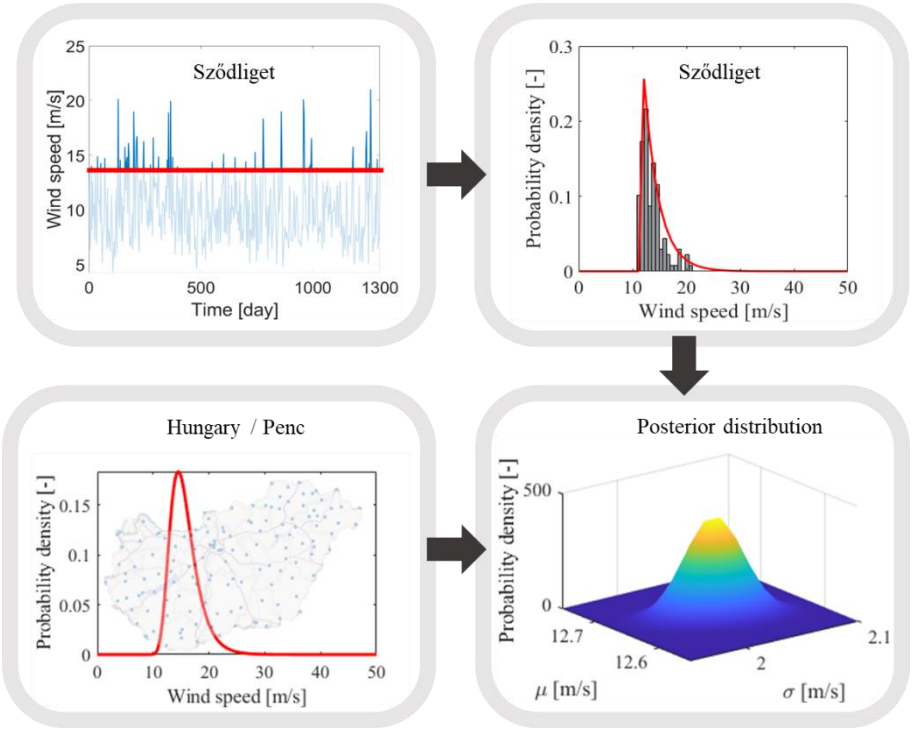

Figure 3.8. Flowchart of the POT method with Bayesian inference

Bayesian inference is employed to update the bivariate normal distribution of σ and μ, which is associated with the GEV distribution of 20-year-long data series:

$$p(\sigma, \mu|D) = \frac{p(D|\sigma, \mu)\, p(\sigma, \mu)}{p(D)}, \tag{3.11}$$

where D denotes the data, $p(\sigma,\mu|D)$ is the posterior distribution of GEV parameters, $p(\sigma,\mu)$ is the prior distribution associated with Penc and Hungary, specifically the following cases: Hungary - 10 min, Hun - Kriging - 10 min, Penc - 10 min. The probability of the observed data, denoted as $p(D)$ and referred to as the marginal likelihood, is determined through trapezoidal numerical integration using MATLAB (R2022a). The likelihood function $p(D|\sigma,\mu)$ is derived from the data D collected at Sződliget by fitting using MATLAB and calculating it through the negative log-likelihood. It is important to note that the posterior distribution combines our pre-existing knowledge (prior distribution information) with the insights gained from the data.

Finally, the 10-minute mean wind velocity having the probability of 0.02 for an annual exceedance is calculated using the inverse cumulative distribution function (ICDF) of the Gumbel distribution with the assessed parameters.

The presented estimation process assumes that past recordings of the variable being studied are still representative of its stochastic behaviour in the present and future. This assumption is based on the notion of stationarity, which assumes that the underlying process remains constant over time and assume constant parameter values throughout time.

3.6 Wind – structure interaction

3.6.1 Eurocode recommendation

Equivalent static wind force acting on the structure is evaluated based on the procedure formulated in EN 1991-1-4 and EN 1993-3-1 (CEN, 2006). The force coefficient is chosen as interaction parameters (IP), since it is affected by significant uncertainty according to previous researches (Georgakis et al., 2009; Koss and Srouji, 2015; Nielsen, 2019). The analysis takes into account the uncertainty associated with both the aerodynamic coefficients of the structure and the antennae.

The wind force F_{w} acting upon a structure or structural component can be directly calculated according to EN 1991-1-4:

$$F_{\mathrm{w}} = \mathrm{c_S}\, c_{\mathrm{d}}\ c_{\mathrm{f}}\ q_{\mathrm{p}}(z_{\mathrm{ref}})\ A_{\mathrm{ref}}, \tag{3.12}$$

where $c_S c_d$ is the structural factor, c_f is the force coefficient, $q_p(z_{ref})$ is the peak velocity pressure at reference height z_{ref}, A_{ref} is the reference area of the structure or structural element. As discussed in Chapter 2.4, it is assumed that the structure is sufficiently rigid to avoid unfavourable aeroelastic responses when subjected to real extreme wind loads. Therefore, the effect of the structure's turbulence vibrations (c_d) on wind effects is neglected, and the structural factor $c_S c_d$ is set to 1. Consequently, in addition to the above approximation, the non-simultaneous occurrence of wind pressure peaks (c_S) acting on the surface is not taken into account. The check for applicability of the static procedure according to equation B.12 in EN 1993-3-1 is checked:

$$\frac{7\, m_T}{\rho_S\, c_{f\,T} A_T \sqrt{d_B \tau_0}} \left(\frac{5}{6} - \frac{h_T}{h}\right)^2 = 0.4683 < 1, \tag{3.13}$$

where $c_{f\,T} A_T$ is the sum of the panel wind forces (including ancillaries), commencing from the top of the tower (in m^2), m_T is the total mass of the panels making up $c_{f\,T} A_T$ (in kg), ρ_S is the density of the material of the tower structure (in kg/m^3), h is the height of the tower (in m), h_T is the total height of the panels making up $c_{f\,T}$ but not greater than $h/3$ (in m), τ_0 is a volume/resistance constant taken as 0,001 m, d_B is the depth in the direction of the wind.

For a lattice structure with a square or equilateral triangular plan form, having equal areas on each face, the total wind force coefficient for a section in the direction of the wind is calculated as follows:

$$c_{f,S} = K_\theta\, c_{f,S,0}\, \frac{A_S}{A_{ref}}, \tag{3.14}$$

where K_θ is the wind incidence factor, $c_{f,s,0}$ represents the overall normal drag (pressure) coefficient of a section without considering end-effects, and it depends on the solidity ratio ϕ. A_S is the total area projected normal to the face of the structural components, including those ancillaries treated as structural elements, of the considered face within one section height at the level concerned, A_{ref} is the reference area of the structure or structural element, i.e., the sum of the projected area of the members of the face projected normal to the face.

The structure is divided into 9 sections (shown in Figure 3.1) with nearly identical panels to enable the wind loading to be adequately modelled for the global analysis. The tower sections are also divided into three faces and all ancillary components are allocated to each face as shown in Figure 3.2a. The solidity ratios and force coefficients are evaluated corresponding to each angle of attack.

Figure 3.9a shows solidity ratios for various angles of attack corresponding to three stages, i) the bare structure, ii) structure equipped with linear ancillaries, and iii) structure equipped with discrete ancillaries. The calculated force coefficients are also represented in Figure 3.9b; however, the wind load acting on discrete ancillaries are calculated and applied separately in the numerical model.

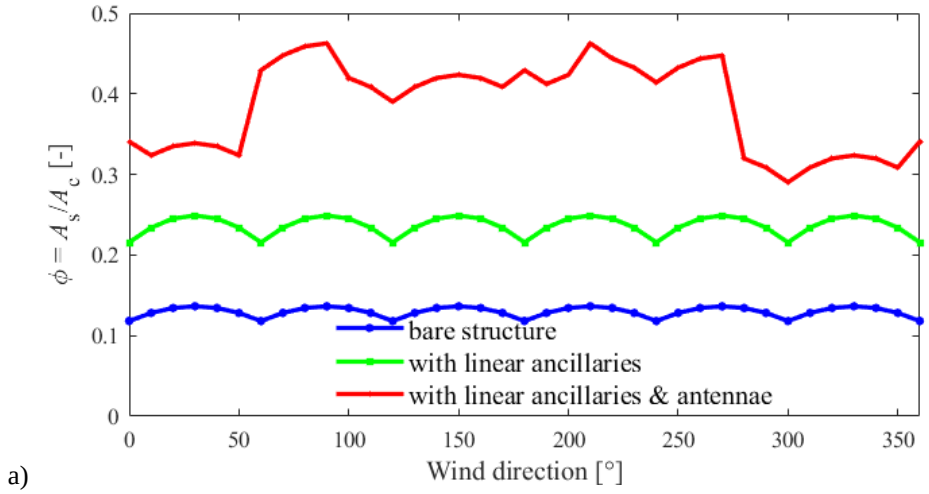

a)

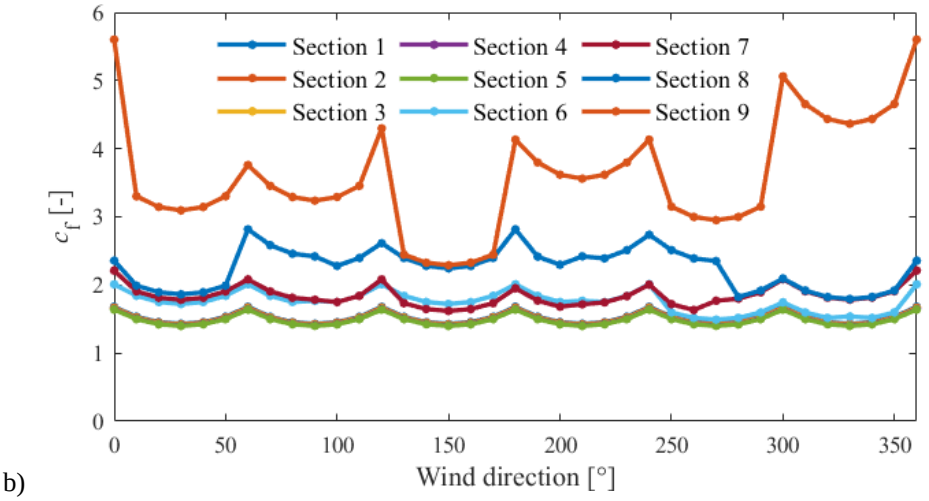

b)

Figure 3.9. a) Solidity ratio and b) force coefficients for various angles of attack of the wind

3.6.2 Wind tunnel test

In comparison to the wind force calculated according to EN 1993-3-1, the structural performance is determined by applying the wind force obtained from wind tunnel tests conducted by Balczó et al. (2006), as well. The wind tunnel tests were conducted on a mast section with a diameter of $D = 108$ mm for the hot dip galvanized legs and $D = 75$ mm for the bracing members as depicted in Figure 3.10.

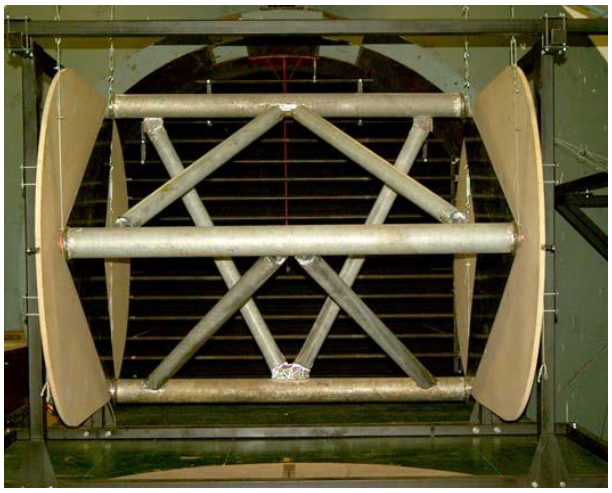

Figure 3.10. Mast section in the wind tunnel (Balczó et al., 2006)

The drag coefficient of the bare structure fluctuates between 0.87 and 1.03, contingent on the wind direction and computed in accordance with EN 1993-3-1. Conversely, it falls within the range of 0.75 to 0.85 based on wind tunnel measurements conducted within the Reynolds numbers range of 2.7-2.8·10^5 (Figure 3.11).

The problem arising from differences between wind load coefficients derived from wind tunnel tests on full-size structures and on reduced-scale models is to be avoided. These differences are reflected not only in the coefficient magnitude but also in the wind velocity range (Reynolds number) at which they occur. Therefore, the measured values from the wind tunnel tests are utilized only for tower sections 7-9, because these sections align with the ones utilized in the wind tunnel experiments. Standard wind forces are applied to sections 1-6. The performance of the investigated mast is calculated by utilizing the wind load obtained from wind tunnel tests and according to EN 1993-3-1. The results of both calculations are then compared.

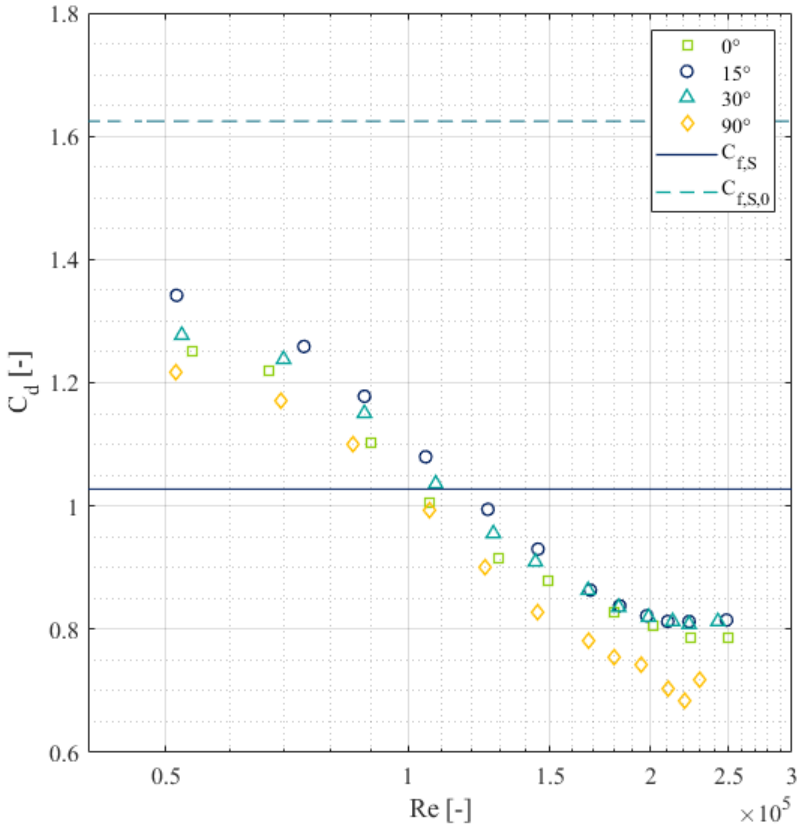

Figure 3.11. The drag coefficient of the mast section for different Reynolds numbers

3.7 Structural analysis

3.7.1 Geometry

The numerical model of the telecommunication mast subjected to wind loading is developed in a general-purpose finite element software (ANSYS v19.0), in order to predict wind load-induced structural response. Main dimensions of the structure and designations of chords and bracings are shown in Figure 3.12. Nominal cross-sectional properties of the corresponding structural elements are summarised in Table 3.3, such as section type numbering, section name (OD_{nom}×t_{nom}: circular hollow section O, nominal diameter D_{nom} [mm], nominal wall thickness t_{nom} [mm]), cross-sectional area A, area moment of inertia I, and approximate characteristic length L. Note that the mean density of steel is increased by 5% in order to indirectly consider additional self-weight of welds, bolts, gusset plates, etc.

Table 3.3. Nominal dimensions of chords and bracings (*approximate length of chord/bracing)

Section type #	Section name	A [mm^2]	I [mm^4]	L [mm]
1	O159×13	5963	1.60×10^7	3100
2	O133×12.5	4732	8.68×10^6	3000
3	O133×10	3864	7.36×10^6	3000
4	O108×5	1618	2.15×10^6	3000/4980*
5	O89×3.2	863	7.95×10^5	4440
6	O76×3.2	732	4.86×10^5	3970
7	O76×2.9	666	4.46×10^5	3350

3.7.2 Finite element mesh

Three-dimensional two-node beam elements (BEAM188), with quadratic shape functions an internal node in the interpolation scheme, are used in the finite element model which is suitable for analysing slender to moderately thick beams. The applied element type is based on Timoshenko beam theory including shear-deformation effects using first-order shear-deformation theory, i.e., cross-sections remain plane and undistorted after deformation. Six nodal degrees of freedom (DOF) option is chosen for the analysis with unrestrained warping (optional seventh degrees of freedom) of cross-sections. Finite element mesh of the telecommunication mast is shown in Figure 3.12. Mesh sensitivity analysis is carried out using element sizes ranging from 250 mm to 1000 mm, regarding the rotation of the top of the tower and its load-bearing capacity, in order to verify the applied mesh scheme. This resulted in expected structural failure probabilities ranging from $4.9\cdot10^{-5}$ to $3.1\cdot10^{-4}$, with a probability of $3.1\cdot10^{-4}$ observed for element sizes of 500 mm. In general, average element size is ~ 500 mm; thus, at least six elements are defined along lines between joints. The number of nodes and elements are 2508 and 1317, respectively. Stub hollow sections are embedded in the foundation, while the superstructure is connected by using moment-resisting end plates with bolts. Therefore, translational and rotational DOFs of nodes representing the supports are constrained (Figure 3.12c).

3.7.3 Applied loads

Nodal wind force loads are defined in accordance with the Eurocodes or wind tunnel tests detailed in Section 3.6. Forces are defined in the nodal coordinate system, which is rotated with respect to the actual wind direction for each simulated case (Figure

3.12d and Figure 3.12e for antennae and structure with linear ancillaries, respectively). Rigid beams are defined for antennae 1, 6 and 10 in order to take into account the eccentric wind loading (Figure 3.12d and Table A.1).

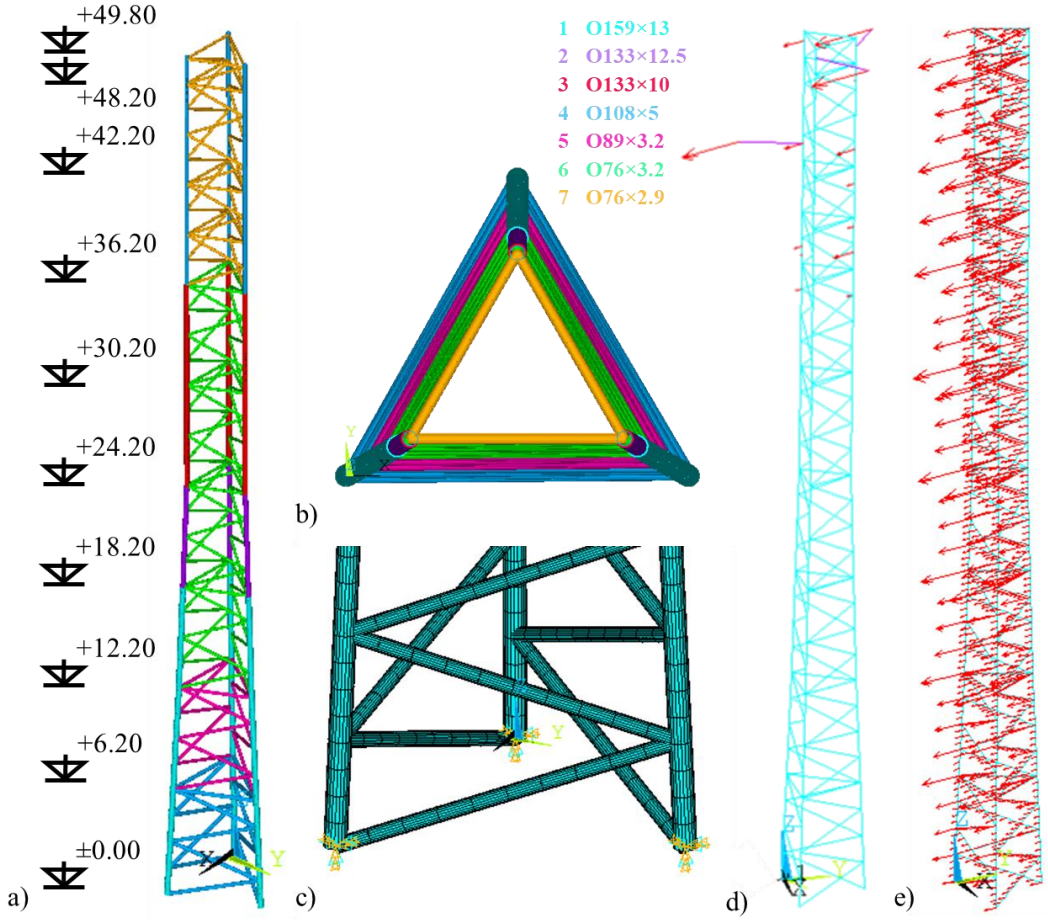

Figure 3.12. Finite element mesh of the mast: a) section types and changes in cross sections, b) top view, c) boundary conditions, nodal loads for d) antennae and e) structure with linear ancillaries

This investigation does not consider actions from ice, including their gravitational effects or their impact on wind actions. When determining wind forces under iced conditions, it's important to increase the projected areas of structural elements and ancillaries to properly account for the thickness of ice as necessary.

The analysis does not account for the impact of one-sided solar radiation and the consequent temperature difference. Nevertheless, it was modelled and assessed by considering the temperature variance within the cross-section of the chord members. In the model, a temperature difference of ± 0.5°C on both sides of the cross-section was

defined, which resulted in a stress of 1.5 MPa (Figure 3.13). Additionally, measurements conducted in September, at a sunny air temperature of 25 °C, on a circular hollow section with a diameter of 140 mm and a plate thickness of 4.5 mm. In this case, the temperature difference between both sides of the section was approximately 5 °C. Based on measurements at the Sződliget tower, it was determined that the expected value of temperatures for wind velocity above 10, 15 and 20 m/s are 10, 9, and 8 °C, respectively (Figure 3.14). These conditions result in a stress of less than 2 MPa. Consequently, the effect of one-sided solar temperature difference is considered negligible when modelling and estimating structural reliability for extreme wind effects.

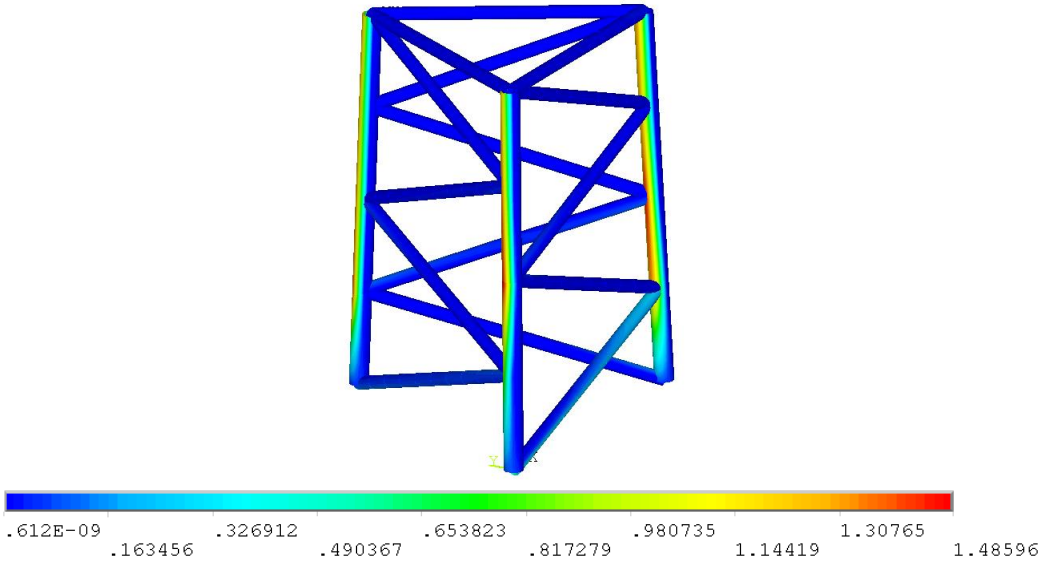

Figure 3.13. First principal stresses induced by temperature variation across cross-section of chord members

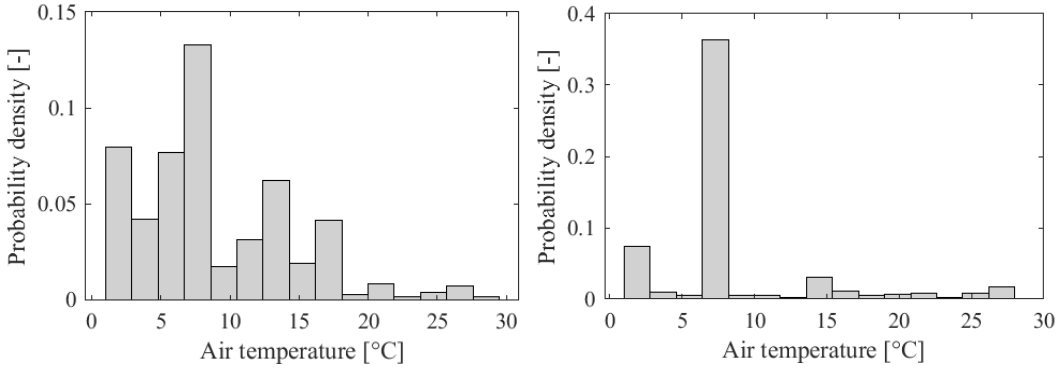

Figure 3.14. Air temperature at Sződliget with wind velocity above 15 (left) and 20 m/s (right)

3.7.4 Material model

Linear material model, with Young's modulus E_a and Poisson's ratio $v = 0.3$, is applied in the model for predicting rotations and displacements in serviceability limit state (SLS). Large deflection effects are included in all the simulations. On the other hand, nonlinear material properties, and equivalent geometrical imperfections are included as well in the geometrically and materially nonlinear analysis with imperfections (GMNIA) for assessing load-bearing capacity in ultimate limit state (ULS). Quad-linear isotropic hardening material model is defined for S235 structural steel grade according to Gardner et al. (2019) and prEN 1993-1-14 (CEN, 2020) in order to accurately capture yield plateau and strain-hardening behaviour of normal strength steels (Figure 3.15). The mean yield strength is calculated by $f_{y,nom} \times a \times e^{-u\nu} - C$ according to the probabilistic model code of JCSS, where $f_{y,nom}$ is the nominal value, a is spatial position factor ($a = 1.00$ for cold formed sections), u is assumed to be -2.0, ν is coefficient of variation, while C is a constant for reducing the yield strength with a value of 20 MPa.

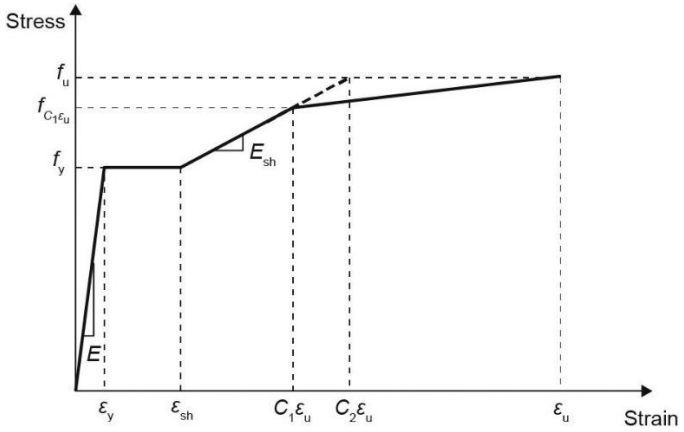

Figure 3.15. Quad-linear isotropic hardening material model (Gardner et al., 2019)

3.7.5 Equivalent geometrical imperfections

The global (sway imperfection of the entire mast) and local (combined flexural buckling-type imperfection of bracing and chord) imperfections are also taken into consideration. The amplitude of initial sway imperfection (global) is defined as $2/3 \times H/200$, where H is the total height of the structure in accordance with Section 5.3.2 in EN 1993-1-1. Local bow imperfections are defined with an amplitude of $L/150$,

where L is the characteristic length, according to Table 5.1 and in Table 6.2 (curve 'c' for cold formed hollow sections) in EN 1993-1-1 and EN 1993-1-5. Equivalent geometrical imperfections (Figure 3.16), covering the influence of manufacturing-induced geometrical imperfections and residual stresses, are defined in the model based on linear analysis (with prescribed displacement) and first eigenshape calculated by linear buckling analyses for global and local imperfections, respectively. The plane of sway imperfection is identical to the plane defined by the wind direction, while local imperfection is based on the first eigenshape in all the analysed cases for the actual wind loads with variable wind direction and magnitudes.

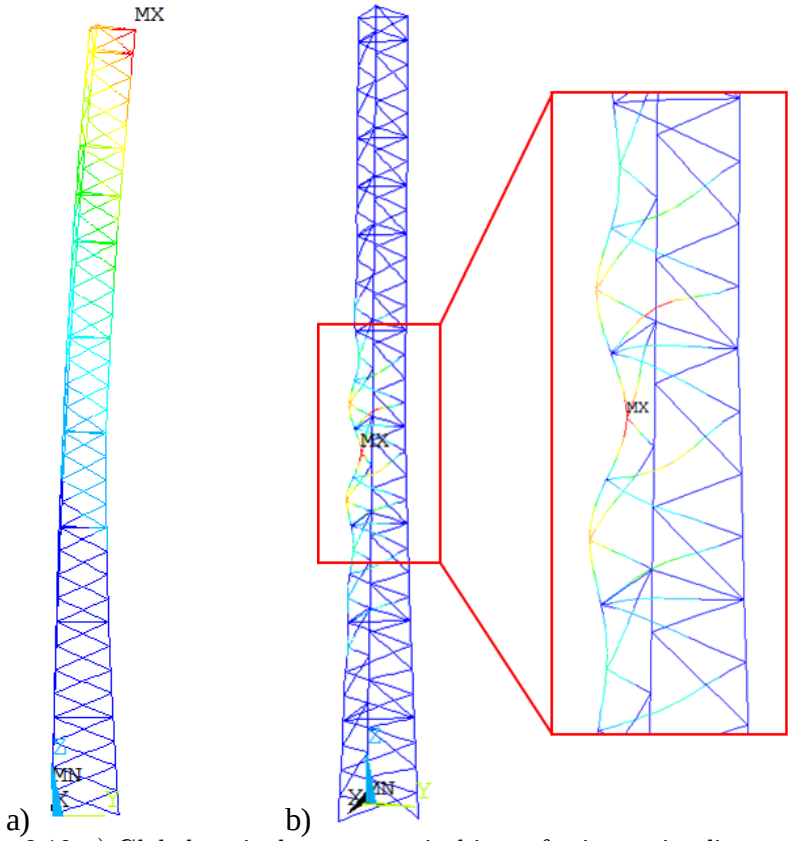

Figure 3.16. a) Global equivalent geometrical imperfections using linear analysis, b) local equivalent geometrical imperfections of chord using eigenshape

4 Results and discussion

4.1 Annual maxima of the HMS

The mean and STD of the annual maximum peak wind velocity for Hungarian meteorological stations (2002-2022), the current values in the EN 1991-1-4 Hungarian National Annex (2007), and the nearest station of the HMS, Penc (1999-2022), are summarized in Table A.4. The standard error of the mean $s_{\bar{V}_1}$ and standard deviation s_{s_1} are 0.082 and 0.058, respectively, for Hungarian meteorological stations (2002-2022). The wind velocity $v_{0.98}$, with a probability of 0.02 for an annual exceedance at the Penc station, is 17% lower compared to the averaged Hungarian $v_{0.98}$ for the period 1999-2022, and it is 22% lower compared to the value $v_{0.98}$ in the Hungarian National Annex. The parameters σ and μ of the fitted Gumbel distribution are 3.076 m/s and 22.257 m/s according to Eqs. (3.3)-(3.6) and can be found in Table 4.3.

Table 4.1. Means, STDs of the annual maximum peak wind velocity and wind velocities with $p = 0.02$ for an annual exceedance [m/s]

	Mean	STD	$v_{0.98}$
Hungary (1999-2022)*	24.032	3.945	34.257
Hungary (EC National Annex)	24.143	3.489	36.186
Penc	21.714	2.770	28.895

* Source: Hungarian Meteorological Service

The Kriging spatial distribution plot of the location μ and scale σ parameter of the GEV distribution are presented in Figure 4.1. The estimated parameters at Sződliget and the corresponding fundamental basic wind velocity can be found in Table 4.3.

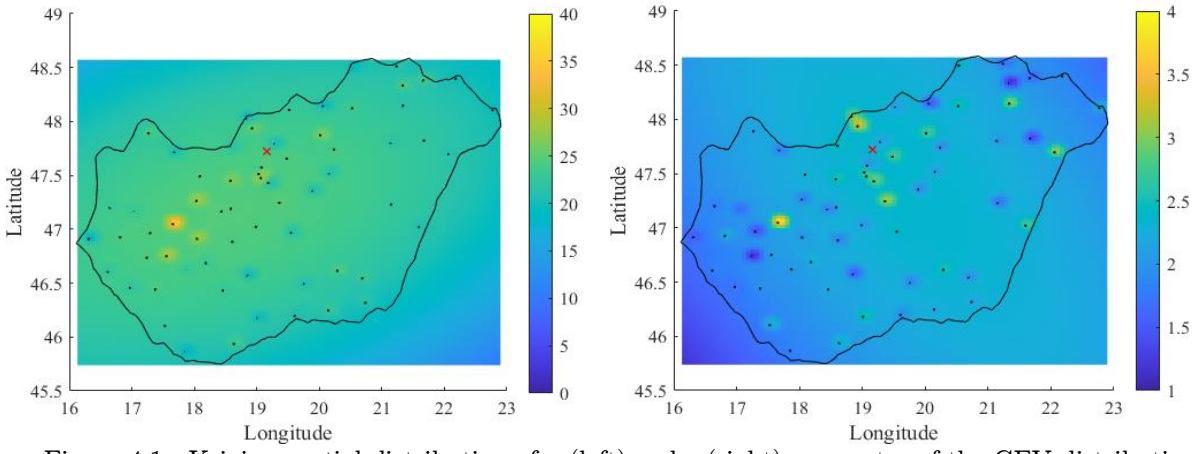

Figure 4.1. Kriging spatial distribution of μ (left) and σ (right) parameter of the GEV distribution

4.2 Wind data series of Sződliget

4.2.1 Wind direction

Figure 4.2 shows the wind direction distribution of Sződliget, where the north-western prevailing wind direction can be observed. Gaussian distribution is fitted to the data within the interval [240°, 360°] and distribution parameters μ and σ are assessed as 299.72° and 18.62°, respectively.

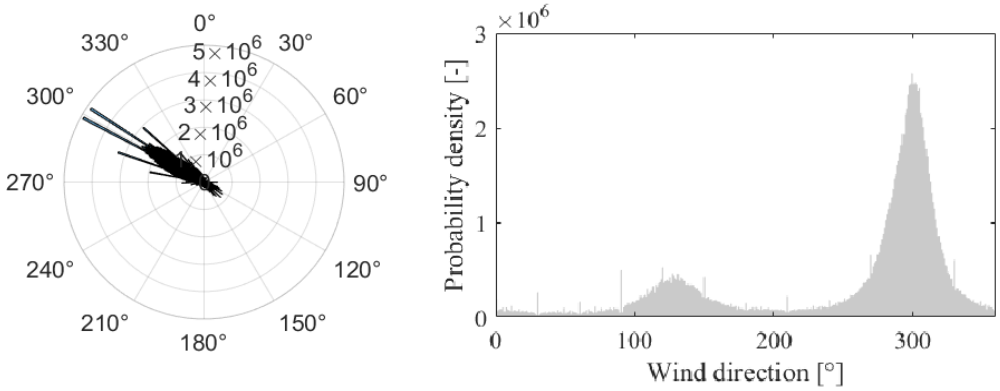

Figure 4.2. Polar histogram and histogram of wind direction distribution

4.2.2 The gust factor

The turbulence intensity, the peak factor, and the wind gust factor for both 10-minute and 1-hour averaging period are presented in Table 4.1 and Figure 4.3. The JCSS recommendation suggests an expected peak factor value of 3.2 for a 1-hour averaging time, along with a coefficient of variation of 0.125. The measurements taken at Sződliget closely align with this recommendation, indicating an expected value of 3.356 and a coefficient of variation of 0.160.

Table 4.1. Turbulence intensity, peak factor, and the gust factor for 10-minute and 1-hour averaging

	Averaging time	**Expected value**	**CV**
Turbulence intensity I_v	10 min	18.32%	0.233
	1 hour	21.72%	0.302
Peak factor g	10 min	2.786	0.156
	1 hour	3.356	0.160
Gust factor c_g	10 min	2.020	0.144
	1 hour	2.460	0.218

It's worth noting that the JCSS recommendation indicates that the 10-minute gust factor should be around 70% of the 1-hour gust factor. However, based on measurements at Sződliget, this ratio is approximately 82%.

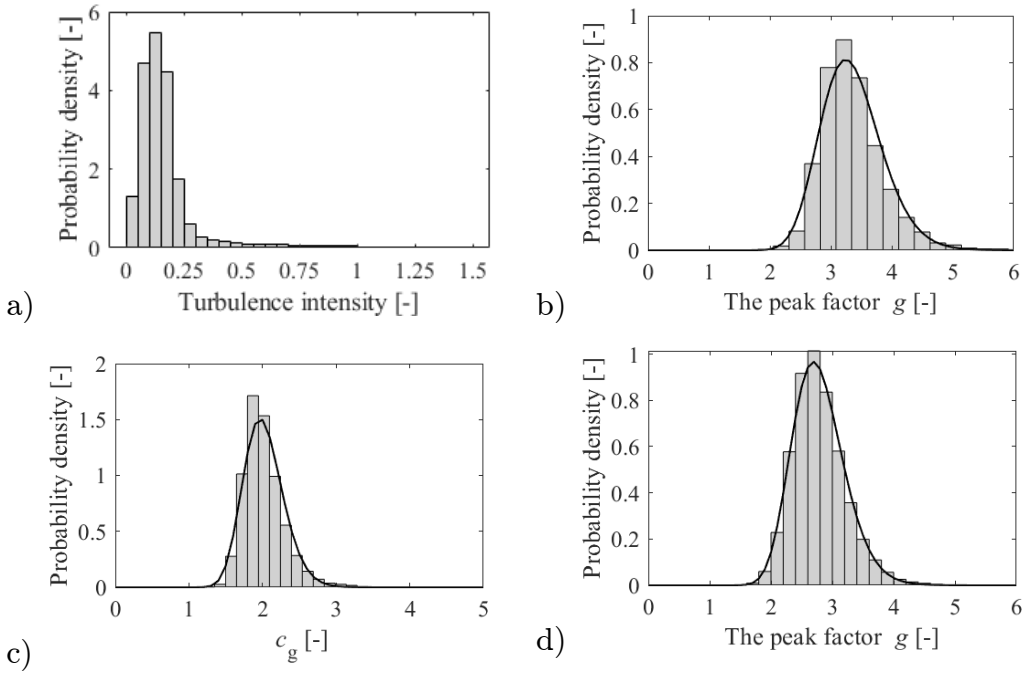

Figure 4.3. Histogram of turbulence intensity (a) and peak factor for 1 hour (b) and 10 min (d) averaging, and gust factor (c)

4.2.3 Roughness length

The expected value of the roughness length z_0 is estimated as 0.877 m based on the measurement excluding wind directions ranging from 60° to 270° because wind speed sensor is installed directly on the chord member of the mast at the height of 25 m (Figure 4.4). The logarithmic wind velocity profile with the assessed z_0 is then employed to estimate the wind velocity at a height of 10 m.

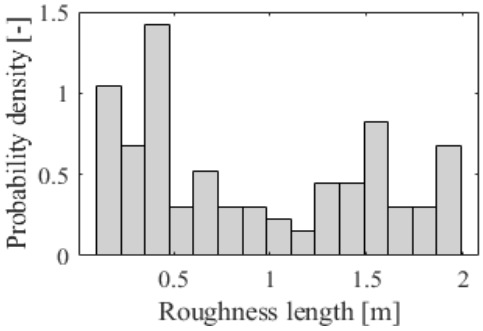

Figure 4.4. Histogram of the roughness length

4.2.4 Measurement of Sződliget

The time series records of maxima for 1, 3 and 7 days are shown in Figure 4.5-Figure 4.7.

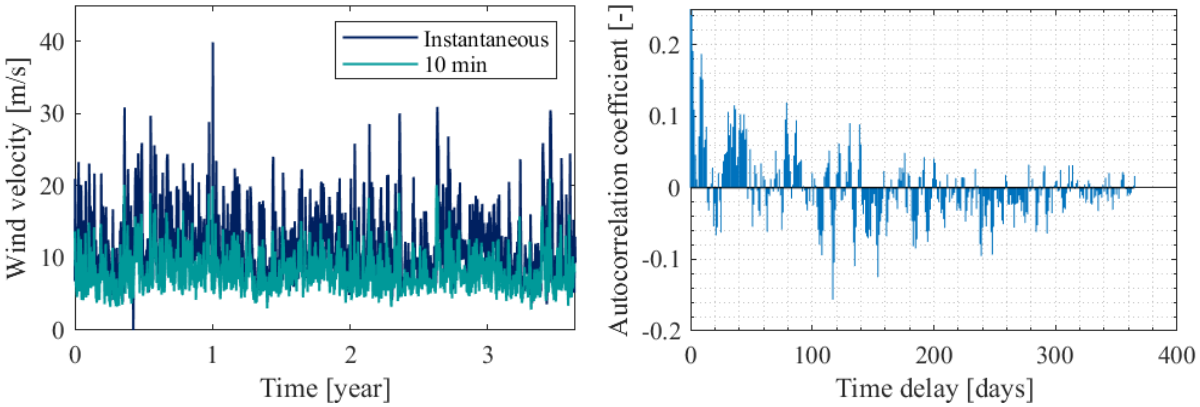

Figure 4.5. Time series plot and autocorrelation function of daily maxima of Sződliget

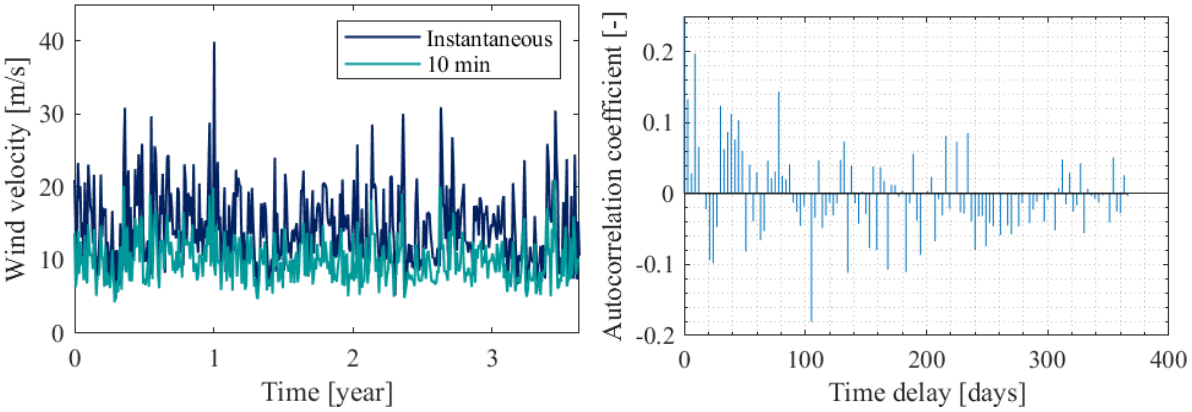

Figure 4.6. Time series plot and autocorrelation function of maxima for 3 days of Sződliget

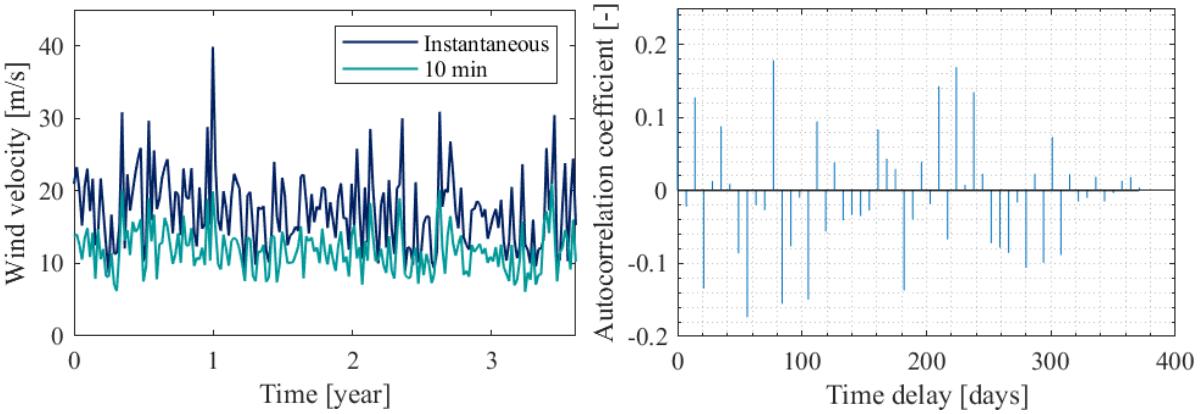

Figure 4.7. Time series plot and autocorrelation function of maxima for 7 days of Sződliget

The autocorrelation functions reveal low correlation coefficients for the 1, 3, and 7-day maxima. Nonetheless, in the case of 7-day maxima, the correlation falls to zero after the first lag confirming the statistical independence of events. This pattern differs for daily or 3-day maxima, where more distinct trends emerge, and the correlation drops to zero after a greater number of lags. Therefore, the maxima for 3 and 7 days are analysed in this study. This selection results in 441 and 189 data, respectively.

4.2.5 The POT method

The 10-minute averaged wind velocity data points are extracted from the wind speed record of Sződliget as detailed in Section 3.4.2 (Figure 4.5-Figure 4.7). Statistically independent events are determined using autocorrelation analysis and maxima for 3 days is assumed as independent events.

The automatic threshold selection method is verified and compared with traditional graphical diagnostics. The conditional distribution is in the domain of attraction of the GPD if the mean excess plot follows a straight line (Figure 4.8). Hence, the proper threshold should be selected beyond the graph appears to be linear. In this case, linearity occurs between 4 and 8 m/s. The grey band represents the 95% confidence intervals computed using the delta method. The decreasing behaviour of the mean excess plot indicates lighter tail (shape parameter $\xi < 0$).

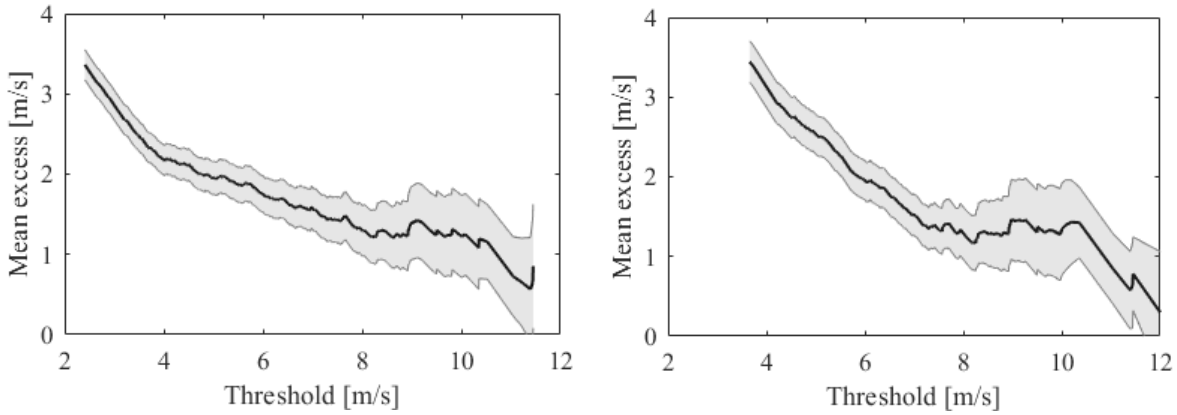

Figure 4.8. Mean excess plot for the maxima for 3 (left) and 7 days (right)

Furthermore, the suitable threshold can be selected with the help of shape and scale parameter plots (Figure 4.9-Figure 4.10). One should find the point where the shape parameter remains constant, and the scale parameter follows a linear pattern. This

holds true between 5-8 m/s for 3-day maxima and 7-8 m/s for 7-day maxima. For threshold values exceeding 9 m/s, the shape parameter drops below -0.5, resulting in the maximum likelihood converging to a boundary point within the parameter space. Consequently, the confidence intervals and standard errors cannot be computed reliably.

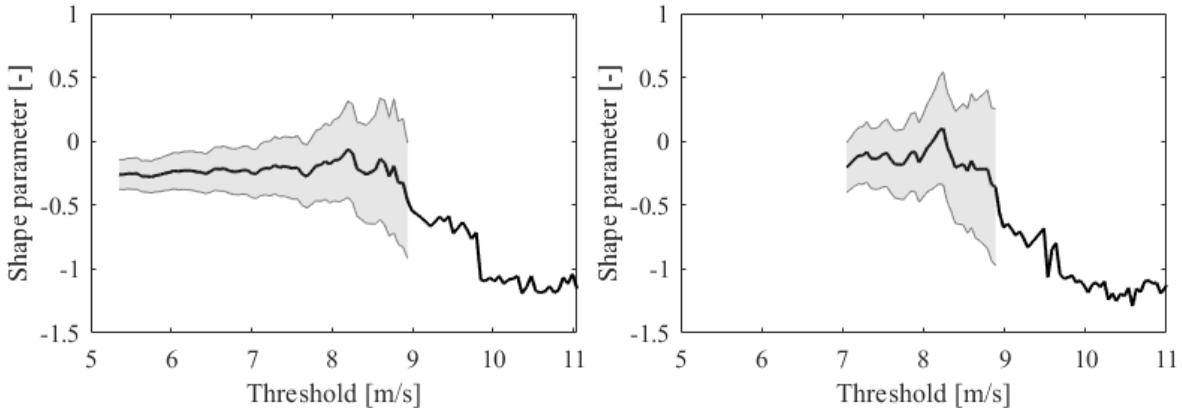

Figure 4.9. Shape parameter for the 3 (left) and 7-day (right) maxima

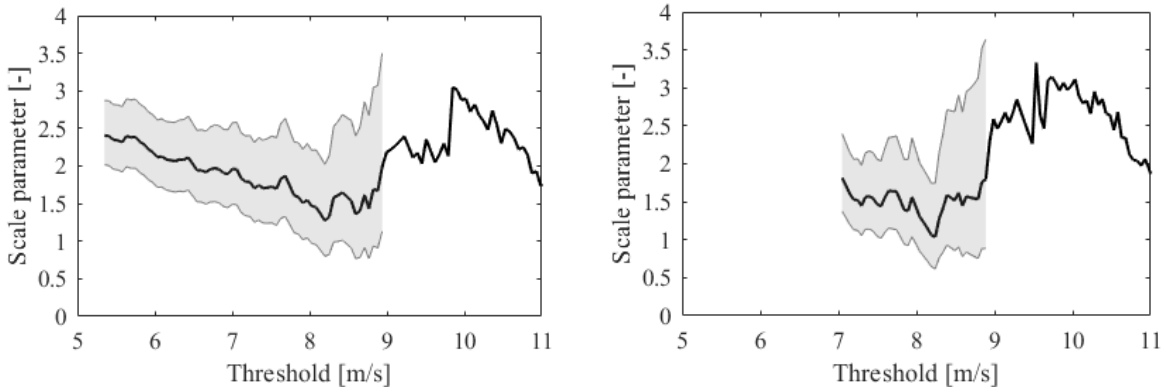

Figure 4.10. Scale parameter for the 3 (left) and 7-day (right) maxima

As outlined in Section 3.4.3, the reparametrized scale parameter τ is defined, and an appropriate threshold is automatically selected. This threshold is chosen above which the differences between two adjacent τ values follow normal distribution with a mean of zero. The red vertical line indicates the automated threshold selection choice (Figure 4.11). For the 3 and 7-day maxima, wind velocities of 6.379 m/s and 7.632 m/s are identified as suitable thresholds, with 129 and 67 samples, respectively, exceeding these values. In both scenarios outlined here, the automatic threshold selection adheres

to the conventional graphical diagnostic criteria. The chosen threshold falls within the range where the mean excess plot exhibits a linear pattern, the shape parameter remains relatively constant, and the scale parameter shows a linear pattern.

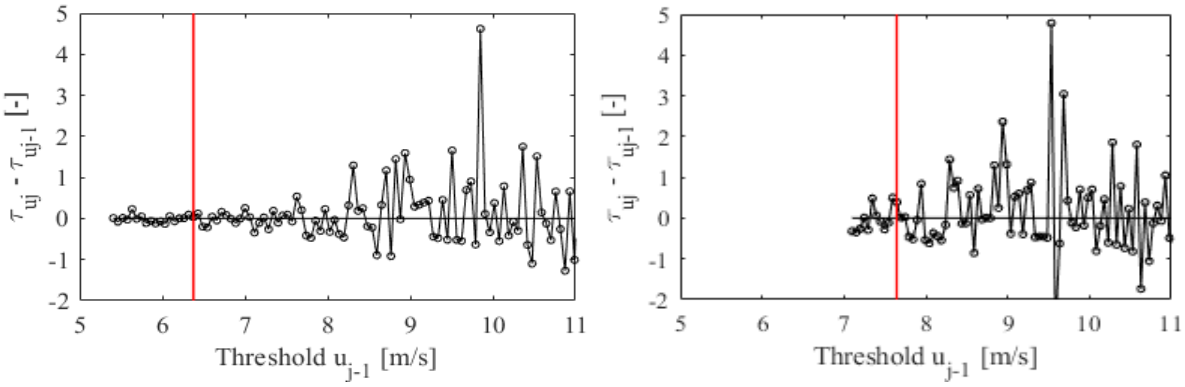

Figure 4.11. Graph of the differences τ_{uj} - τ_{uj-1} for the 3 (left) and 7-day (right) maxima

The GPD distribution is fitted to the data, and the estimated parameters can be seen in Table 4.2. When statistical uncertainty is neglected, the GPD distribution with a negative shape parameter consistently provides a better fit to the data compared to the shape parameter of zero, due to the third additional parameter (Baravalle and Köhler, 2018), as depicted in Figure 4.12. However, the CV for the shape parameter is notably high, ranging from 0.3 to 0.7, and the CV for the scale parameter ranges from 0.11 to 0.18. The CV for the case with a shape parameter of zero is in the range of 0.05 to 0.07.

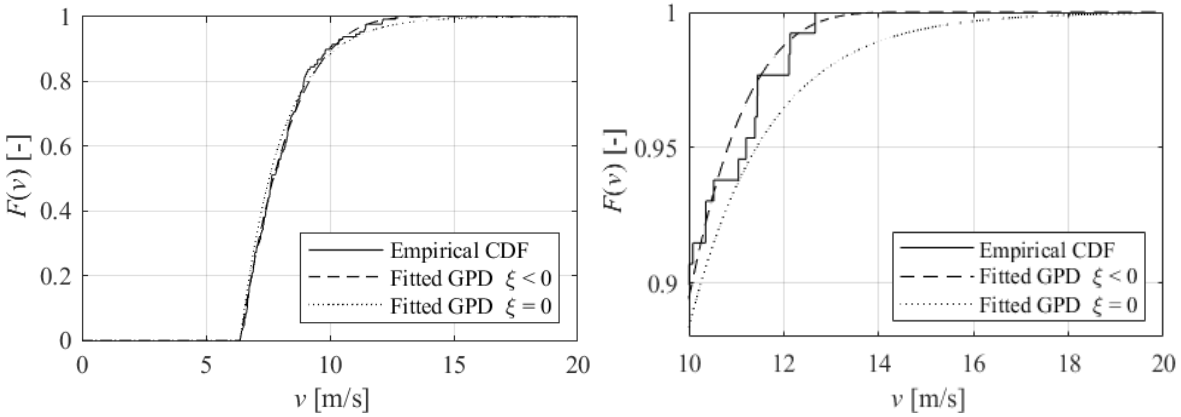

Figure 4.12. Empirical and fitted GPD cumulative distribution functions for 3-day maxima

Table 4.2. Estimated parameters for the fitted GPD distributions

	Maxima	$E(v_{0.98})$	95% confidence interval	μ [m/s]	ξ_{mean}	ξ_{std}	σ_{mean} [m/s]	σ_{std} [m/s]
$\xi < 0$	3-day	11.641	[10.906, 12.377]	6.379	-0.249	0.079	2.105	0.245
	7-day	12.268	[11.105, 13.431]	7.632	-0.171	0.134	1.624	0.293
$\xi = 0$	3-day	12.966	[11.091, 14.842]	6.379			1.684	0.098
	7-day	13.043	[10.762, 15.325]	7.632			1.383	0.095

The quantile plot (Figure 4.13) shows the quantiles of resampled estimates in comparison to the theoretical quantiles from a normal distribution. This allows for the verification that the estimated parameter follows the normal distribution. Subsequently, the delta method can be employed to calculate the 95% confidence interval of parameters.

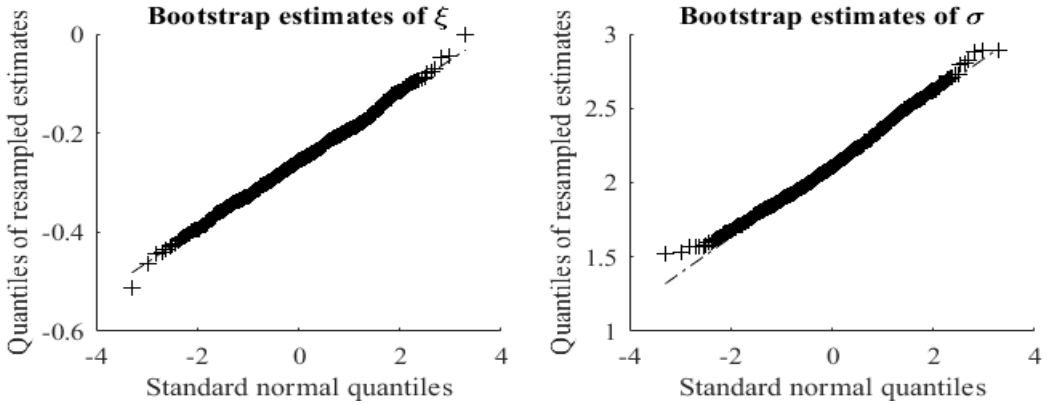

Figure 4.13. Quantile plot of the GPD parameters for 3-day maxima

4.2.6 Wind return level

After the parameter estimates are established, the wind velocity corresponding to a specific return period is calculated from the GPD formula as follows:

$$V_R = \begin{cases} \mu + \frac{\sigma}{\xi}\left[\left(\frac{1}{R}\right)^{-\xi}\right] & for\ \xi \neq 0, \\ \mu - \sigma\, ln\left(\frac{1}{R}\right) & for\ \xi = 0, \end{cases} \tag{4.1}$$

where R is the return period. The return-period wind extremes are derived using both the estimated shape parameter and a shape parameter of zero. These plots (Figure 4.14 and 4.15.) distinctly illustrate the bounded and unbounded characteristics of the two distributions.

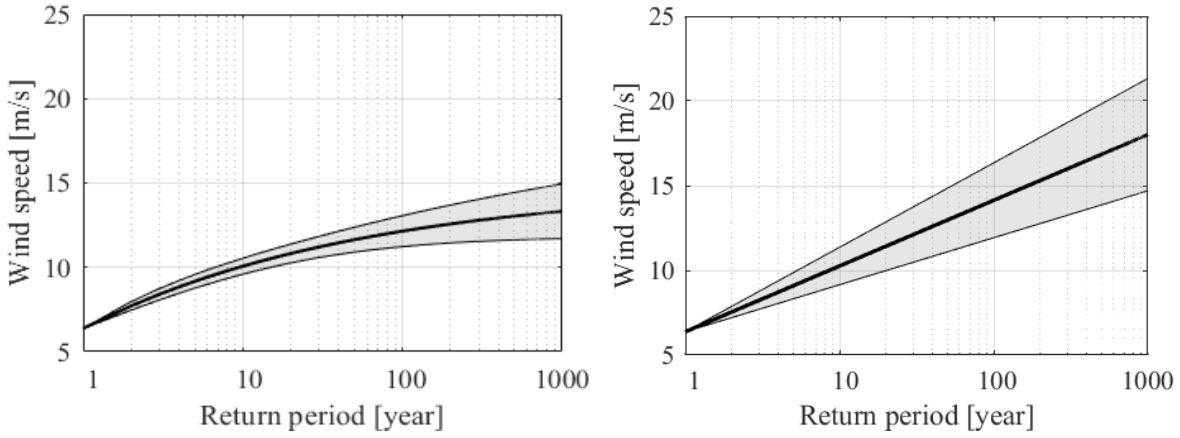

Figure 4.14. Return-period extremes plot for 3-day maxima with $\xi < 0$ (left) and $\xi = 0$ (right)

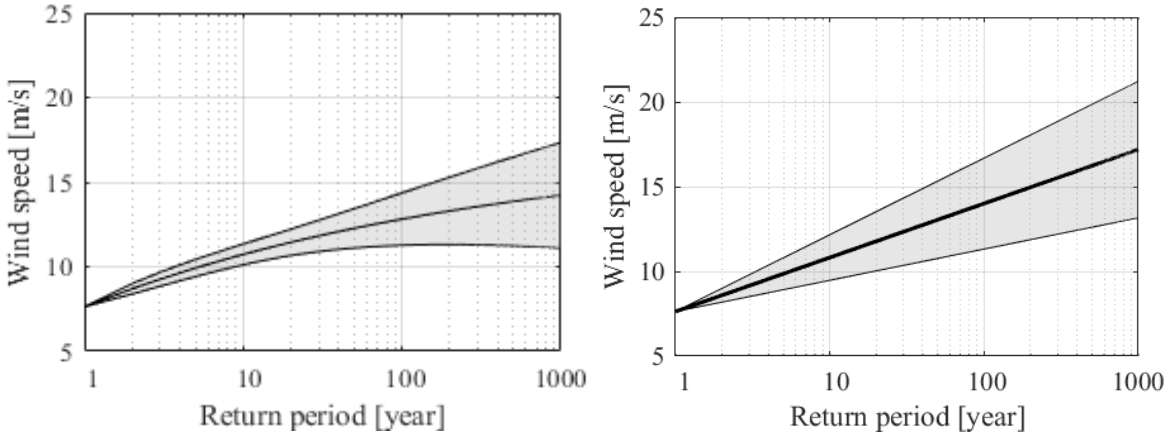

Figure 4.15. Return-period extremes plot for 7-day maxima with $\xi < 0$ (left) and $\xi = 0$ (right)

The shape parameter $\xi = 0$ results in a basic wind velocity estimate that is 6-10% greater than the estimate with $\xi < 0$. The CVs for the 50-year return period wind velocities are 0.03 and 0.07 for 3-day maxima in the cases of $\xi < 0$ and $\xi = 0$, respectively. For the 7-day maxima, the CVs are 0.05 and 0.09 for $\xi < 0$ and $\xi = 0$, respectively. Notably, in the case of 7-day maxima, the CVs are 40% higher for $\xi < 0$ and 19% higher for $\xi = 0$. Clearly, the width of the 95% confidence interval increases as the return periods increase.

4.2.7 Epistemic uncertainties

The fragility curve describes the probability of an *EDP* exceeding a capacity level of *edp* at a given *IM*, in this case, for a given wind velocity v. The general equation to develop fragility or conditional probability is expressed by:

$$G(EDP) = \mathrm{P}\{EDP > edp \mid \ V = v\}. \tag{5.1}$$

Fragility curves are evaluated using numerical probabilistic simulations for both SLS criteria and load-bearing capacity for ULS, as discussed in Section 3.3. Lognormal distributions are fitted to the data points calculated with the finite element model. The resulting curves are illustrated in Figure 4.16.

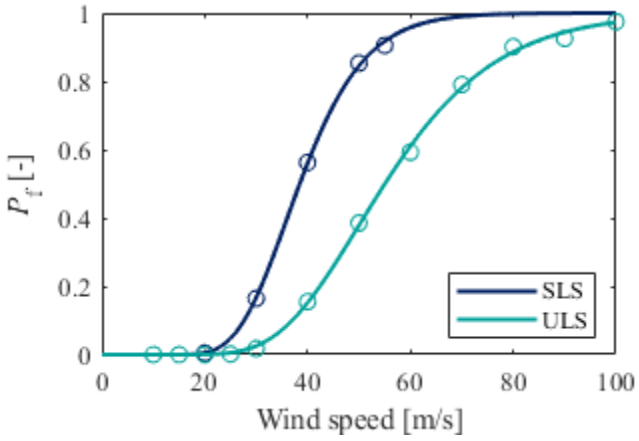

Figure 4.16. Fragility curves for the ULS and SLS limit states

To assess the epistemic uncertainties related to the number of samples, the following framework is employed which is illustrated in Figure 4.17.

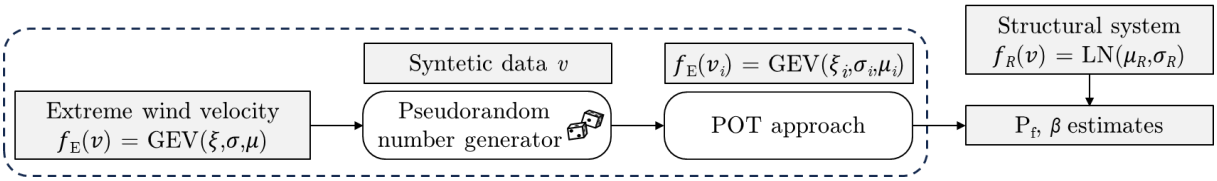

Figure 4.17. The framework for assessing the epistemic uncertainties

The expected value of the estimate converges to the true value as the number of realizations increases and the bandwidth shrinks accordingly. The horizontal line denotes the estimated reliability index β derived from the initial GEV distribution and fragility curve corresponding to ULS. Its value is 5.471 for $\xi < 0$ and 4.967 for $\xi = 0$ (Figure 4.18).

For $\xi<0$, the SEM is 5% for 100 realizations and falls below 1% with more than 200 realizations. The CV related to the number of realizations in this procedure is 9% for 100 realizations, decreases to below 3% with 200 realizations, and further reduces to below 2% with 500 realizations. In case of $\xi = 0$, the SEM stays below 3% for 100 realizations, decreases to below 1% for 200 realizations, and further reduces to 0.1% for 6000 realizations. The CV related to the number of realizations of this procedure is 5% for 100 realizations, drops to below 3% for 200-300 realizations, and further decreases to below 2% for 400 realizations.

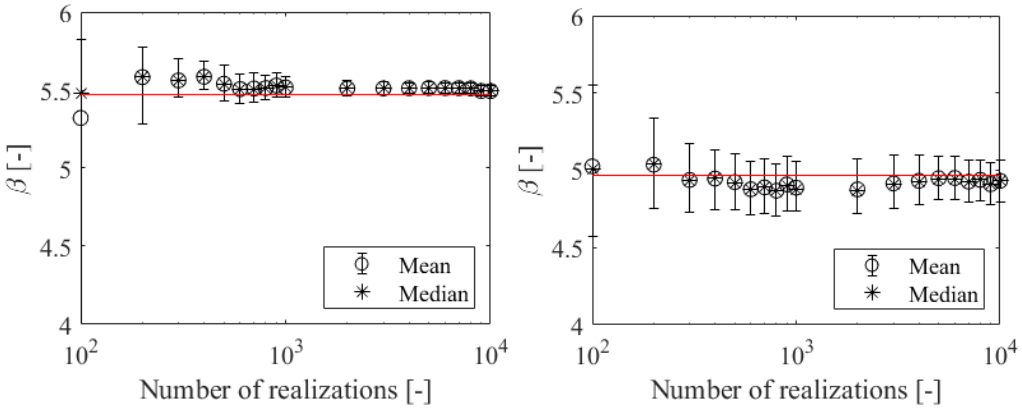

Figure 4.18. The estimated β for various number of realizations, $\xi < 0$ (left) and $\xi = 0$ (right)

The impact of varying CV values of the lognormal distribution representing the resistance side has also been investigated. PDFs of the effect-side fitted GPD and lognormal distributions with different CV representing the structural resistance are plotted on Figure 4.19. For example, the CV of the distribution of tensile strength of concrete can be assumed to be 0.3, while the CV corresponding to material properties of structural steel is about 0.03-0.07 (JCSS, 2001).

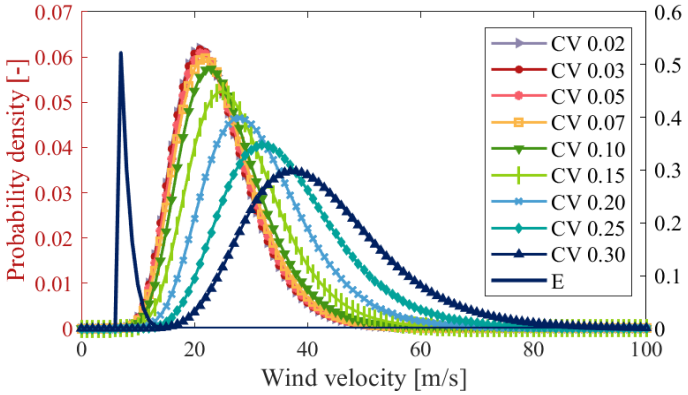

Figure 4.19. The PDF of the effect-side fitted GPD and lognormal distributions with different CV representing the structural resistance

The confidence interval of the reliability index is decreasing with increasing CV of the LND due to spread of the distribution function. In other words, uncertainties of the action side have smaller impact on the assessed uncertainty of the reliability index when there is a larger uncertainty associated with the resistance side (Figure 4.20). The CV for β is 0.04 when the CV of the lognormal distribution representing the resistance is below 0.07. It decreases to less than 0.02 when the CV of the lognormal distribution is greater than 0.25.

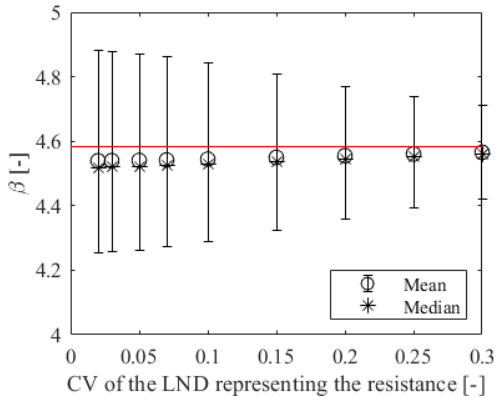

Figure 4.20. Assessed β associating with various CV of the lognormal distributions representing the resistance

4.3 Bayesian inference

Due to challenges in handling a higher-dimensional non-singular multivariate normal distribution and the potential for significant errors in estimating the shape parameter ξ, this study focuses on the distribution with ξ of 0. This choice is applied in the subsequent processes of Bayesian updating and the probabilistic analysis of the structure. Hence, the bivariate normal distribution of parameters σ and μ of the Gumbel distribution are evaluated from these means and STDs and can be seen in Figure 4.21a, Figure 4.22a and Table 4.3 (ρ denotes the correlation between σ and μ). Thus, the data series from Hungary and Penc serve as the prior distribution of parameters, which is then updated with data from Sződliget using Bayesian inference. The cases under investigation are detailed in Section 3.2. The resulting posterior distributions are depicted in Figure 4.21b, Figure 4.22b, and the parameters can be found in Table 4.3 under the labels "Hun - Sződliget ", "Hun - Kriging - Sződliget" or "Penc - Sződliget".

Applying the POT approach to the 10-minute average wind speed dataset of Penc, the scale σ and location μ parameters of the GEV distribution with shape parameter ξ of zero are obtained, which are estimated to be 0.861 and 8.800, respectively. The fundamental basic wind velocity $v_{0.98}$, with a probability of 0.02 for an annual exceedance, is calculated to be 12.4 m/s using this method. This value is approximately 2% lower than the result obtained through the traditional annual maxima method, indicating good agreement between the two approaches. However, the $v_{0.98}$ corresponding to the Penc and "Sződliget - GPD" are lower by 57% than the $v_{0.98}$ corresponding to Hungarian meteorological stations. The standard deviation of the GEV distribution parameters calculated by Kriging interpolation ("Hun - Kriging", "Hun - Kriging - 10 min") is larger than that calculated by the delta method ("Hungary - peak", "Hungary - 10 min").

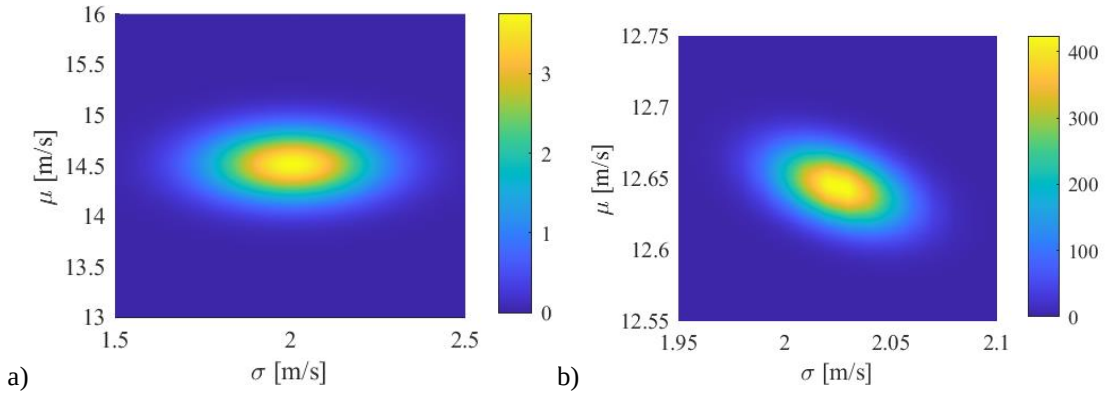

Figure 4.21. The bivariate normal distribution of parameters σ and μ of the Gumbel distribution - Hungary, 10-minute averaged wind speed, a) prior distribution b) posterior distribution

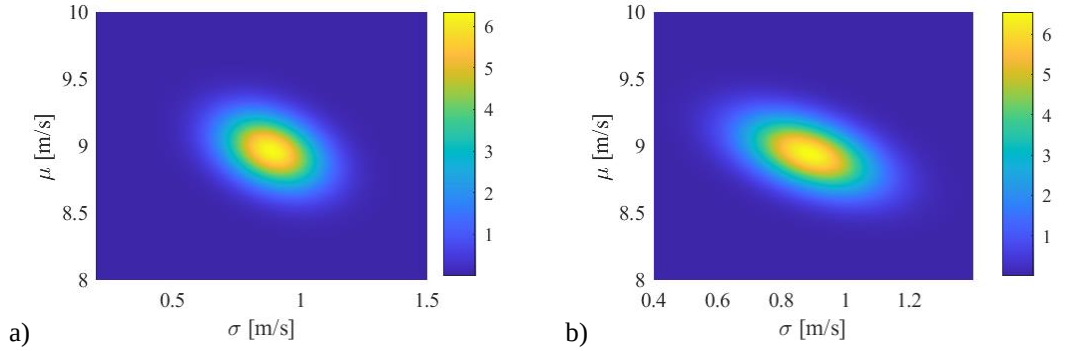

Figure 4.22. The bivariate normal distribution of parameters σ and μ of the Gumbel distribution - Penc, 10-minute averaged wind speed, a) prior distribution b) posterior distribution

Table 4.3. Evaluated parameters of extreme wind speed models [m/s]

	μ mean	μ std	σ mean	σ std	ρ	$v_{0.98}$
Sződliget GPD	6.379	-	1.684	0.098	-	12.966
Hungary - peak	22.257	0.094	3.076	0.045	-	34.258
Hungary - 10 min	14.511	0.247	2.005	0.172	-0.395	22.337
Hun - Kriging	23.423	2.393	2.317	0.480	-	32.465
Hun - Kriging - 10min	15.272	1.560	1.511	0.313	-	21.168
Penc - 10 min	8.964	0.192	0.888	0.138	-0.330	12.430
Hun - Sződliget	12.644	0.019	2.025	0.021	-0.394	20.547
Hun - Kriging - Sződliget	11.818	0.580	1.710	0.510	-0.394	18.489
Penc - Sződliget	8.941	0.194	0.887	0.141	-0.456	12.402

4.4 Structural analysis

4.4.1 Characteristic failure modes

Figure 4.23 illustrates the characteristic failure modes. In case (a), flexural buckling of lower chord member are observed, typically arising from wind directions around 280°. In the case of failure mode (b), failure is primarily governed by the yielding of the lower chord member and tends to occur at a wind direction of approximately 330°. Lastly, in failure mode (c), the loss of stability in a lattice truss element within section 3 is noticed, with typical occurrences at wind directions approximately around 300°.

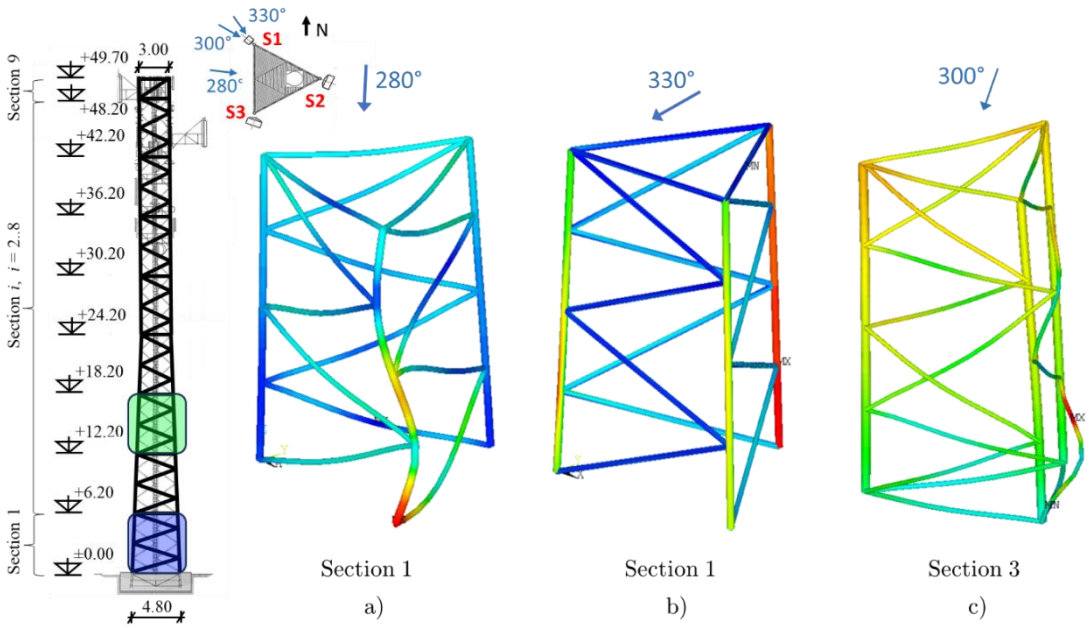

Figure 4.23. Characteristic failure modes: flexural buckling for a) and c), and yielding for b)

4.5 Internal axial forces in chords

Assuming uniaxial stresses in chord members, internal axial forces are evaluated applying the Hook's model and using the Young's modulus E_a (210000 MPa) and the cross-sectional area of the measured chords (5963 mm^2). Internal axial forces in chords S_1, S_2 and S_3 are sorted corresponding to wind speed of $v = 10$, 15, 20, 30 m/s, and turbulence intensity of 10, 20, 30%. Then, sinusoidal functions are fitted to these data points and expected values are extracted regarding the interesting directions for the triangular section tower, i.e., 270°, 300° and 330° (Table A.2 in the Appendix). Two examples can be seen in Figure 4.24 and 4.25, for the case of wind speed $v = 15$ m/s.

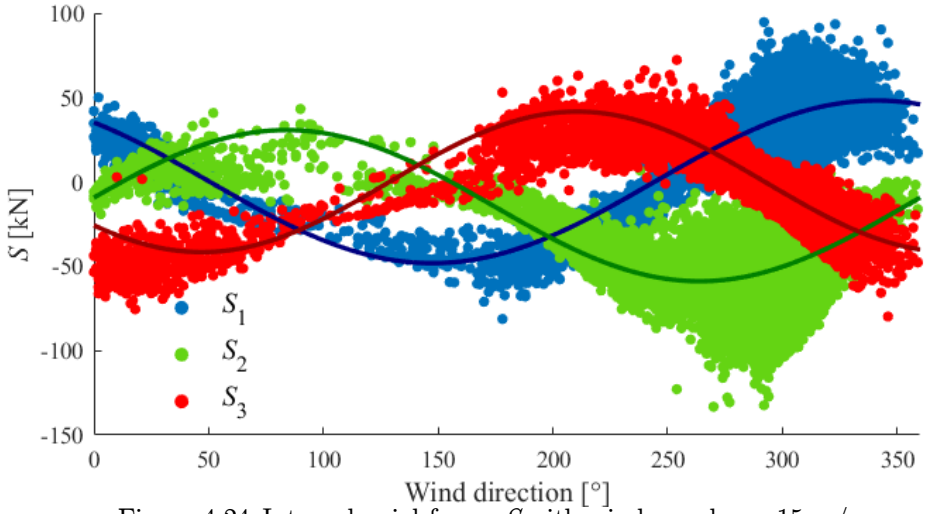

Figure 4.24. Internal axial forces S with wind speed $v = 15$ m/s

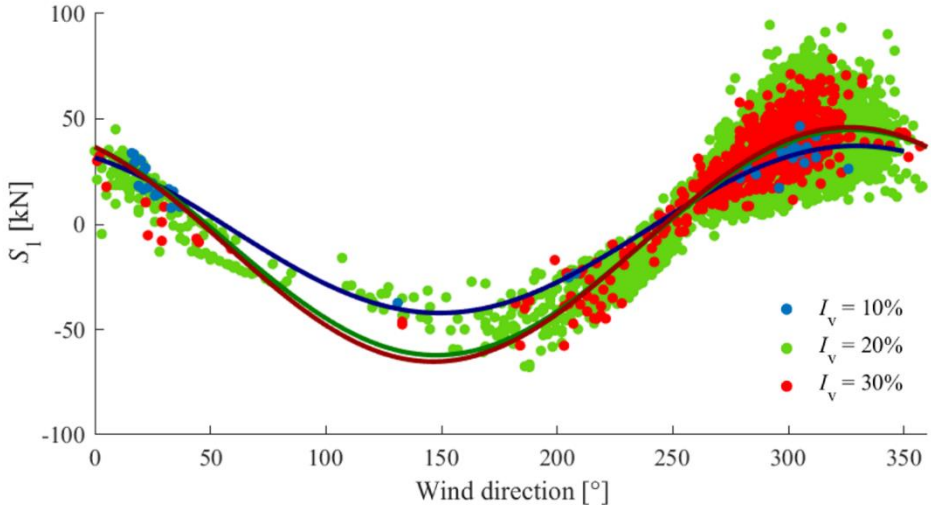

Figure 4.25. Internal axial force S_1 at $v = 15$ m/s and turbulence intensities of 10, 20, 30%

4.6 Discussion of force coefficients

The results of the deterministic numerical model based on EN 1993-3-1, specifically internal axial forces in chord members, are compared to the extracted values from measurements (Table A.3). The distinction between the "EC" and "wind tunnel" cases lies solely in the wind load values. In the "EC" case, these values are calculated following the EN 1993-3-1 standard. Conversely, in the "wind tunnel" case, the wind load values derived from the wind tunnel tests (Balczó et al., 2006) were incorporated into the numerical model. Due to the north-western prevailing wind direction, the S_3 axial force is in the vicinity of the neutral axis; therefore, these values are not presented here.

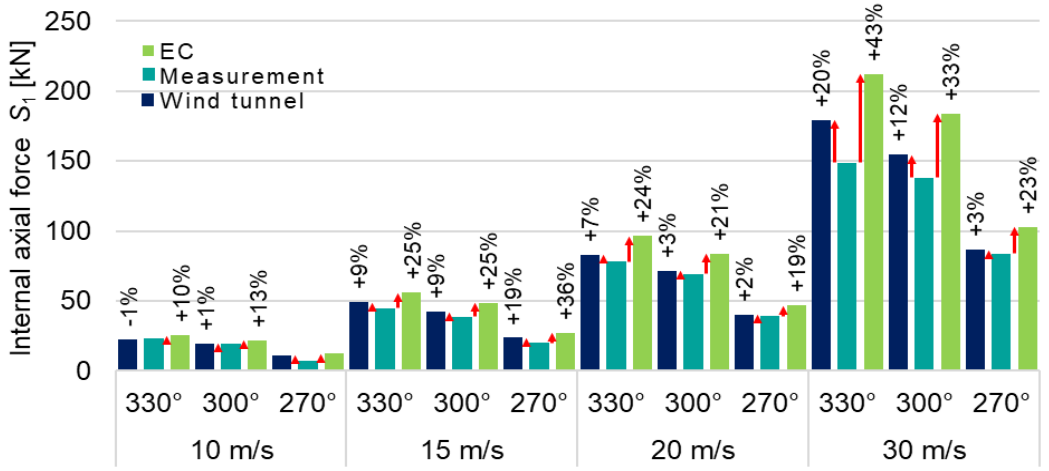

Figure 4.26. Internal axial force S_1 for $I_v = 20\%$, and for various wind velocity, wind direction

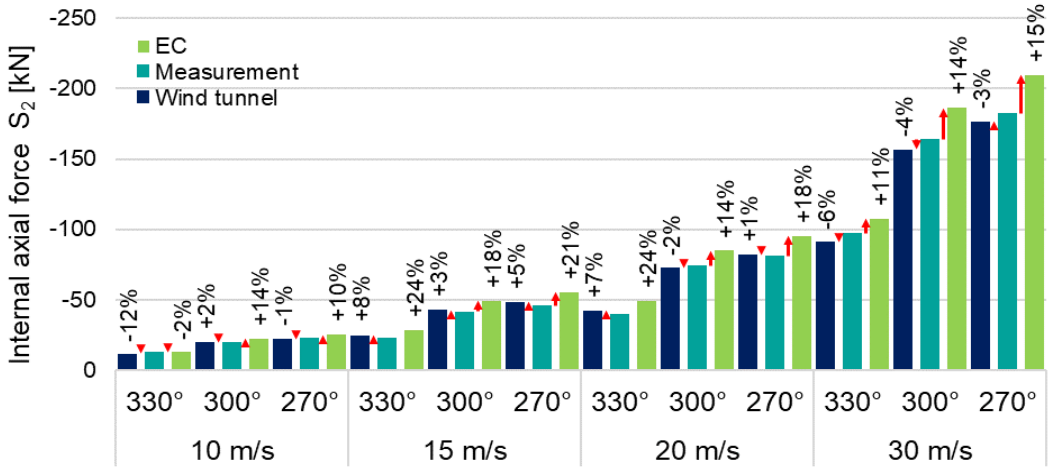

Figure 4.27. Internal axial force S_2 for $I_v = 20\%$, and for various wind velocity, wind direction

In the case of S_1, which is subjected to tension, a noticeable difference of approximately 20-40%, can be observed for high wind velocities (Figure 4.26). In the case of S_2, the differences for high wind velocities are lower, ~ 10-25% (Figure 4.27). By utilizing wind forces measured in the wind tunnel tests, the model was able to reduce these differences to approximately 10-20%. The differences for low wind velocities are less than 14%.

4.7 Damage analysis

The results of Monte Carlo simulation combined with Latin Hypercube (MCS) sampling are presented for high performance level, i.e., SLS, in Figure 4.28a. A limit value of 0.5° is used for the rotation of the top of the tower φ_{top} based on the specifications of telecommunication suppliers, and it is represented as a horizontal line in the figure. The probability distribution functions of the chosen *EDP* are evaluated (Figure 4.28c). The results of Monte Carlo simulations with $N = 10^6$ simulation loops, performed on the derived response surfaces (RSM), are shown in Figure 4.28b and d. Normal, lognormal, and Gumbel distributions were fitted to the samples, and the lognormal gave the best fit using the chi-square goodness-of-fit test. In Table A.4-Table A.5, the parameters of fitted lognormal distributions are summarized based on MCS and RSM for SLS and ULS.

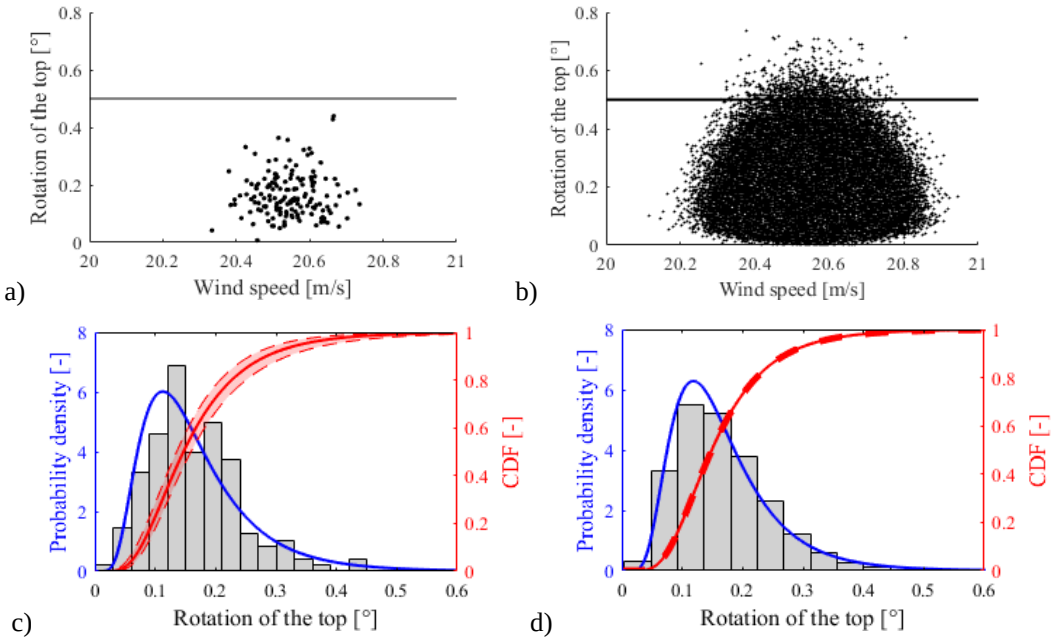

Figure 4.28. The rotation of the top φ_{top} in SLS: a) and b) sample data, c) and d) PDF, histogram, and CDF with confidence interval of 95% for MCS and RSM simulations, respectively

The MCS simulation requires slightly more than one hour when running on a computer with the following parameters: Intel(R) Core(TM) i9-10900 CPU 2.80GHz, RAM 64.0 GB. The RSM simulation requires 1 second.

The results of the probabilistic analysis on the load-bearing capacity of the mast, i.e., the load amplification factor α_{ULS}, are presented in Figure 4.29. The MCS simulation requires approximately eight hours on the same personal computer. The value associated to the ultimate limit state is 1 and represented as a horizontal line in the figure. The RSM simulation requires 1 second, as well.

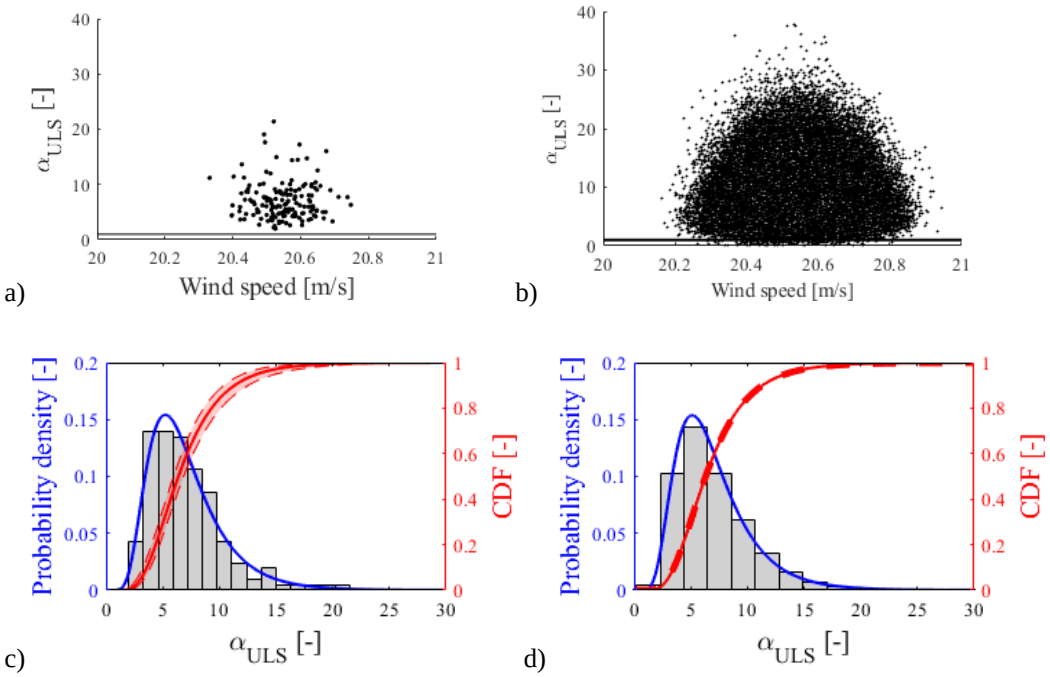

Figure 4.29. The load amplification factor α_{ULS} in ULS: a) and b) sample data c) and d) PDF, histogram, and CDF with confidence interval of 95% for MCS and RSM simulations, respectively

4.8 Discussion of the reliability of the structure

The probabilities of exceeding the serviceability limit and the structural failure P_f are calculated based on fitted lognormal distributions of RSM simulations (Figure 4.30-Figure 4.31). The level of safety for reliability class RC2, in other words, the target probability of exceeding the limit for reference periods of 50 years is $6.68 \cdot 10^{-2}$ for SLS and $7.23 \cdot 10^{-5}$ for ULS, respectively (EN 1990:2002, 2002). For the SLS and ULS

calculation, the average differences between the estimated reliability indices of the MCS and RSM are 2% and 5%, respectively, with a maximum difference of 9% and 17%.

By utilizing the force coefficient c_f derived from wind tunnel tests, the estimated P_f is reduced by approximately two orders of magnitude. Assuming a roughness length z_0 of 0.3 m, as specified according to the EN 1991-1-4 standard for suburban terrain, instead of using the value of 0.877 m based on measurement, leads to an increase in the P_f by approximately half an order of magnitude for the SLS and one order of magnitude for the ULS. Due to the considerably lower observed wind speeds at Sződliget and Penc compared to the Hungarian average, the P_f for Sződliget and "Penc - Sződliget" are significantly lower. The associated P_f are lower by approximately three orders of magnitude for the SLS and around eight orders of magnitude for the ULS. Taking into account raw wind field data from a nearby monitoring station with longer measurements as prior information when estimating the parameters of an on-site extreme wind speed model for a structure may be considered unconservative, as demonstrated in the case of "Penc - Sződliget ". The topography around Sződliget is characterized by the town on flat terrain, with the Danube River situated behind it. In contrast, the surroundings of Penc feature hills with forested areas, which may contribute to lower wind speeds and assessed failure probabilities for „Penc" and „Penc - Sződliget" due to the influence of the terrain.

Using Kriging spatial interpolation to calculate wind speed values at the site of interest from data sets of other stations, and even updating it with field measurement information, leads to a more reliable and consistent result in line with other estimated exceedance probabilities. The estimated exceedance probabilities of the "Hun - Kriging" are slightly smaller, by an order of magnitude for SLS, than the "Hungary" case.

Bayesian updating of the prior information or beliefs associated with the Hungarian average by incorporating the observed data from Sződliget can reduce the probability of failure P_f by approximately one order of magnitude compared to the case of "Hungary".

The probability of exceeding the serviceability limit and the structural failure in accordance with the 95% confidence bounds based on MCS and RSM simulations are summarized in Table 4.4 and Table 4.5.

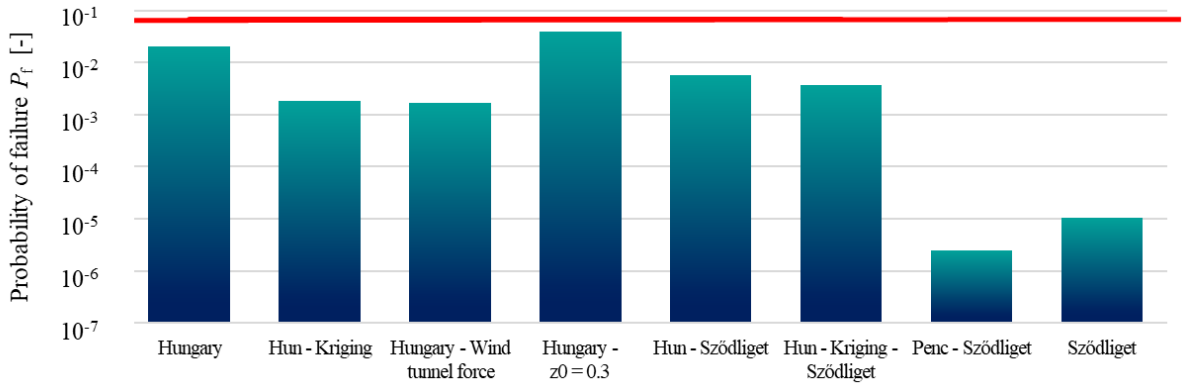

Figure 4.30. The probability of exceeding the serviceability limit for different scenarios and the target P_f according to EN 1990 (EC RC2)

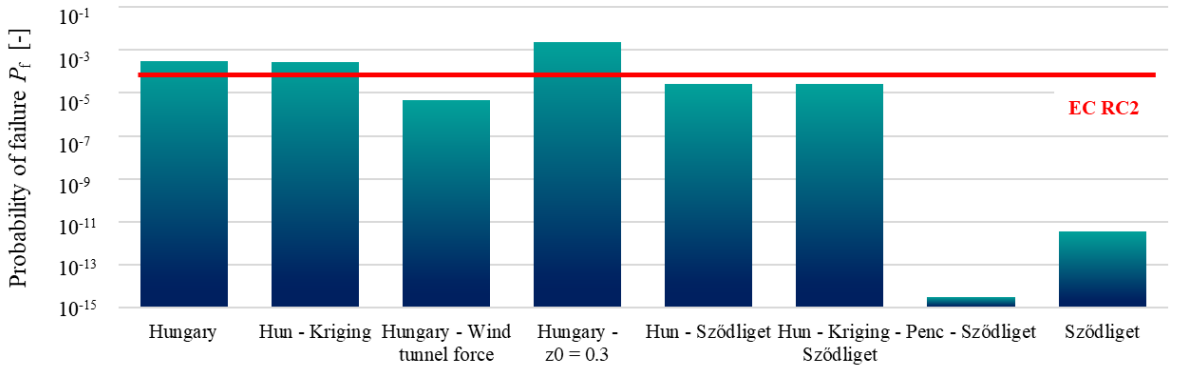

Figure 4.31. The probability of structural failure P_f for different scenarios and the target P_f according to EN 1990 (EC RC2)

Note, that reliability index β is calculated based on P_f assuming Gaussian distribution according to EN 1990:2002 (2002). However, performance function does not follow the Gaussian distribution, therefore, it is only an informative measure of the reliability in this case. The target reliability index β for reliability class RC2 and reference periods of 50 years is 1.5 for SLS and 3.8 for ULS, respectively. In several instances, it is noticeable that while the probability of failure does not surpass the prescribed limit defined by the EC, the value of β falls below the specified threshold. Consequently, β does not accurately indicate the actual frequency of structural failure.

Table 4.4. The probability of exceeding the serviceability limit with the 95% confidence interval (*Gaussian distribution)

	Simulation type	P_f [-]	P_f [-]		β*
Hungary	MCS	$1.72 \cdot 10^{-2}$	$8.28 \cdot 10^{-3}$	$3.31 \cdot 10^{-2}$	2.12
	RSM	$2.04 \cdot 10^{-2}$	$2.02 \cdot 10^{-2}$	$2.06 \cdot 10^{-2}$	2.05
Hun - Kriging	MCS	$1.51 \cdot 10^{-3}$	$4.38 \cdot 10^{-4}$	$4.60 \cdot 10^{-3}$	2.97
	RSM	$1.84 \cdot 10^{-3}$	$1.81 \cdot 10^{-3}$	$1.87 \cdot 10^{-3}$	2.90
Hungary - Wind tunnel force	MCS	$1.89 \cdot 10^{-3}$	$5.75 \cdot 10^{-4}$	$5.51 \cdot 10^{-3}$	2.90
	RSM	$2.71 \cdot 10^{-3}$	$2.68 \cdot 10^{-3}$	$2.75 \cdot 10^{-3}$	2.78
Hungary - $z_0 = 0.3$ m	MCS	$5.71 \cdot 10^{-2}$	$3.50 \cdot 10^{-2}$	$8.90 \cdot 10^{-2}$	1.58
	RSM	$5.54 \cdot 10^{-2}$	$5.50 \cdot 10^{-2}$	$5.57 \cdot 10^{-2}$	1.59
Hun - Sződliget	MCS	$8.77 \cdot 10^{-3}$	$3.69 \cdot 10^{-3}$	$1.92 \cdot 10^{-2}$	2.38
	RSM	$5.62 \cdot 10^{-3}$	$5.55 \cdot 10^{-3}$	$5.68 \cdot 10^{-3}$	2.54
Hun - Kriging - Sződliget	MCS	$2.73 \cdot 10^{-3}$	$9.01 \cdot 10^{-4}$	$7.44 \cdot 10^{-3}$	2.78
	RSM	$3.69 \cdot 10^{-3}$	$3.64 \cdot 10^{-3}$	$3.74 \cdot 10^{-3}$	2.68
Penc - Sződliget	MCS	$2.21 \cdot 10^{-6}$	$1.53 \cdot 10^{-7}$	$2.43 \cdot 10^{-5}$	4.59
	RSM	$2.46 \cdot 10^{-6}$	$2.38 \cdot 10^{-6}$	$2.54 \cdot 10^{-6}$	4.57
Sződliget	MCS	$8.24 \cdot 10^{-6}$	$7.67 \cdot 10^{-7}$	$6.98 \cdot 10^{-5}$	4.31
	RSM	$1.03 \cdot 10^{-5}$	$9.97 \cdot 10^{-6}$	$1.05 \cdot 10^{-5}$	4.26

Table 4.5. The probability of structural failure P_f with the 95% confidence interval (*Gaussian distribution)

	Simulation type	P_f [-]	P_f [-]		β*
Hungary	MCS	$8.73 \cdot 10^{-5}$	$1.37 \cdot 10^{-5}$	$4.63 \cdot 10^{-4}$	3.75
	RSM	$3.13 \cdot 10^{-4}$	$3.07 \cdot 10^{-4}$	$3.19 \cdot 10^{-4}$	3.42
Hun - Kriging	MCS	$2.4 \cdot 10^{-4}$	$4.70 \cdot 10^{-4}$	$1.0 \cdot 10^{-4}$	3.49
	RSM	$2.6 \cdot 10^{-4}$	$2.5 \cdot 10^{-4}$	$2.6 \cdot 10^{-4}$	3.4
Hungary - Wind tunnel force	MCS	$4.83 \cdot 10^{-6}$	$3.99 \cdot 10^{-7}$	$4.55 \cdot 10^{-5}$	4.42
	RSM	$5.50 \cdot 10^{-6}$	$5.34 \cdot 10^{-6}$	$5.67 \cdot 10^{-6}$	4.40
Hungary - $z_0 = 0.3$ m	MCS	$1.29 \cdot 10^{-3}$	$3.64 \cdot 10^{-4}$	$4.06 \cdot 10^{-3}$	3.01
	RSM	$2.26 \cdot 10^{-3}$	$2.23 \cdot 10^{-3}$	$2.29 \cdot 10^{-3}$	2.84
Hun - Sződliget	MCS	$1.72 \cdot 10^{-5}$	$1.89 \cdot 10^{-6}$	$1.26 \cdot 10^{-4}$	4.14
	RSM	$2.58 \cdot 10^{-5}$	$2.52 \cdot 10^{-5}$	$2.65 \cdot 10^{-5}$	4.05
Penc - Sződliget	MCS	$1.49 \cdot 10^{-15}$	$8.59 \cdot 10^{-19}$	$1.20 \cdot 10^{-12}$	7.89
	RSM	$3.09 \cdot 10^{-15}$	$2.84 \cdot 10^{-15}$	$3.37 \cdot 10^{-15}$	7.80
Sződliget	MCS	$2.61 \cdot 10^{-13}$	$4.91 \cdot 10^{-16}$	$7.29 \cdot 10^{-11}$	7.22
	RSM	$3.52 \cdot 10^{-12}$	$3.29 \cdot 10^{-12}$	$3.77 \cdot 10^{-12}$	6.86

The presented estimation process assumes that past recordings of the variable being studied are still representative of its stochastic behaviour in the present and future. This assumption is based on the notion of stationarity, which assumes that the underlying process remains constant over time and assume constant parameter values throughout time. In order to account for potential changes in extreme events, Prosdocimi and Kjeldsen (2021) have formulated a model that assumes a constant coefficient of variation, allowing the location and scale parameters to change simultaneously. This approach, known as non-stationary analysis, allows for the examination of how the behaviour of extremes may have changed over time.

4.9 Sensitivity analysis

The probabilistic sensitivities of Spearman rank-order correlation coefficients are also determined, assuming a nonlinear monotonic increasing correlation between inputs and output. (Figures 4.32 and 4.33). However, it is acknowledged that the certainty of this assumption regarding a monotonically increasing relationship is not guaranteed.

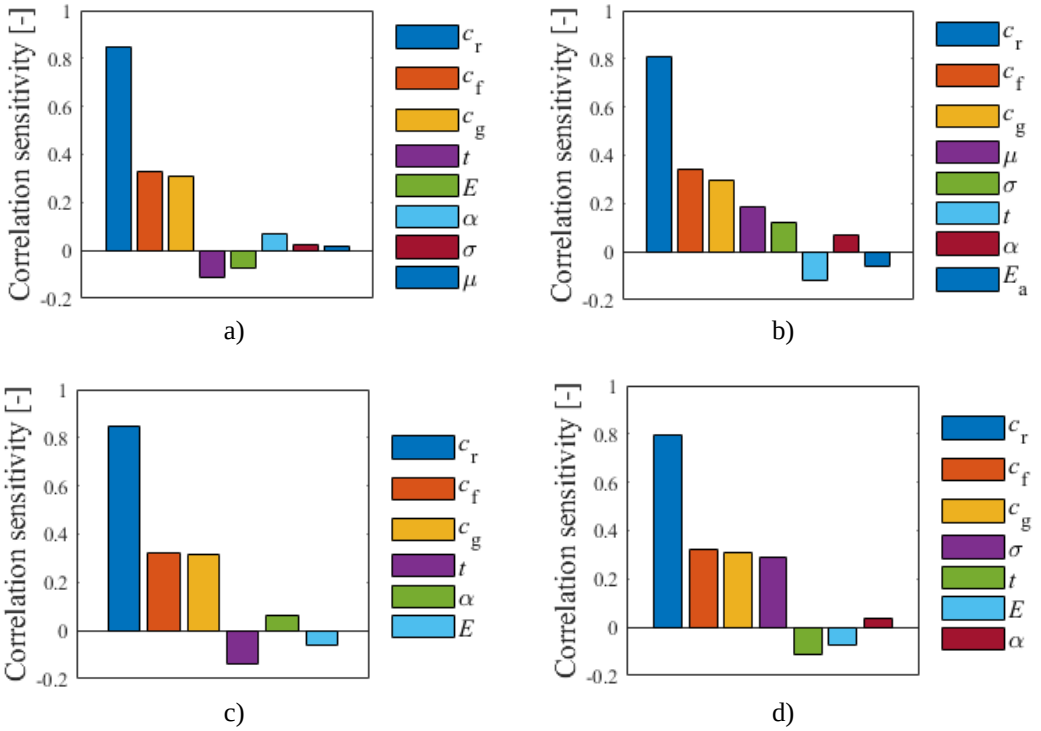

Figure 4.32. Spearman rank-order coefficients for SLS for a) Hungary, b) Hungary - Kriging, c) Hungary - Sződliget, and d) Sződliget

It is highlighted that the roughness factor c_r, force coefficient c_f and gust factor c_g have a dominant influence on the *EDP*s due to their higher CVs, while material parameters have smaller influence on the *EPD*s. The density of the steel ρ is found to be statistically insignificant at a significance level of 2.5% in all cases. In addition, it is observed that σ has a significant impact on the *EDP*s for data extracted from Sződliget, where only the POT method was utilized. In the "Hungary" case, the parameters σ and μ have a relatively small impact. This is possibly due to the standard deviations of these parameters not being determined through MLE fitting; instead, they were calculated using the standard error of the mean and standard deviation, leading to smaller standard deviations. However, in the Bayesian updated case, these two parameters are found to be statistically insignificant. Although, the present statements are valid for the dataset under consideration and for similar climatic conditions, methods presented in this paper are applicable for other wind engineering problem.

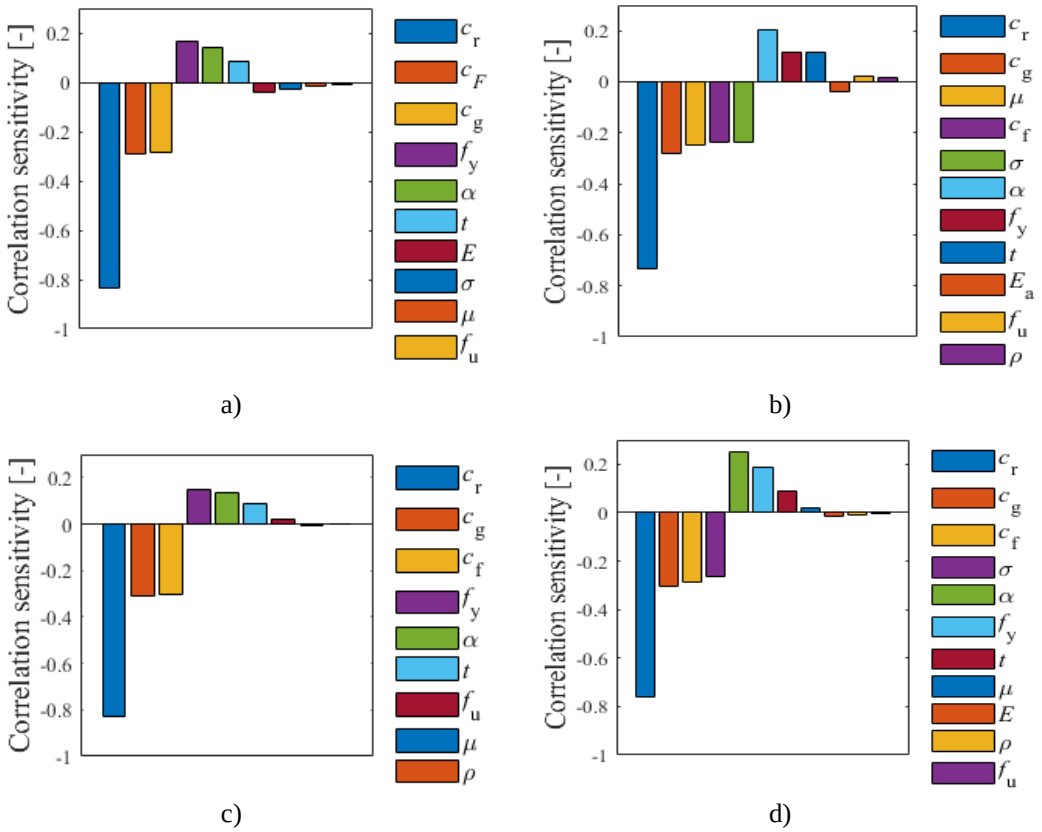

Figure 4.33. Spearman rank-order coefficients for ULS for a) Hungary, b) Hungary - Kriging, c) Hungary - Sződliget, and d) Sződliget

Variance-based sensitivity analysis is conducted alongside the Spearman rank-order coefficients to address nonlinear mathematical models and their Monte Carlo estimates. Specifically, Sobol indices, representing first-order sensitivity indices, are calculated (Figure 4.34 and 4.35). This approach decomposes the variance of the model or system output into fractions that can be attributed to individual inputs or sets of inputs.

This study confirms the significant influence of the c_r factor on the EDPs. Reducing the uncertainty associated with this factor involves enhancing the reliability of the model. In the ULS calculation, the sensitivity of α_{ULS} to wind direction is notable. The Spearman rank coefficient may not detect this sensitivity as it assumes a monotonically increasing relationship between input and output, while the relationship between wind direction and α_{ULS} is non-monotonic. In the "Hun - Kriging" case, the sensitivity of the EDPs to the parameter μ is more significant, while in the "Sződliget" case, the sensitivity to the parameter σ is more noticeable, given the larger standard deviation of these parameters in each respective case.

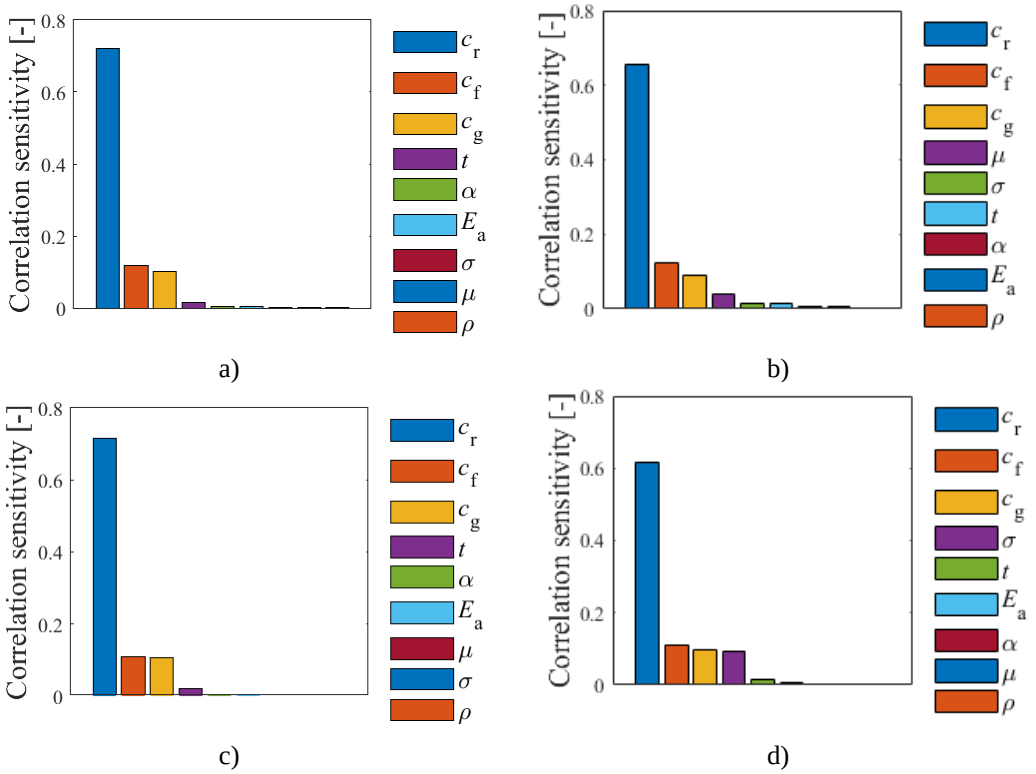

Figure 4.34. Sobol sensitivity indices for SLS a) Hungary, b) Hungary - Kriging, c) Hungary - Sződliget, and d) Sződliget

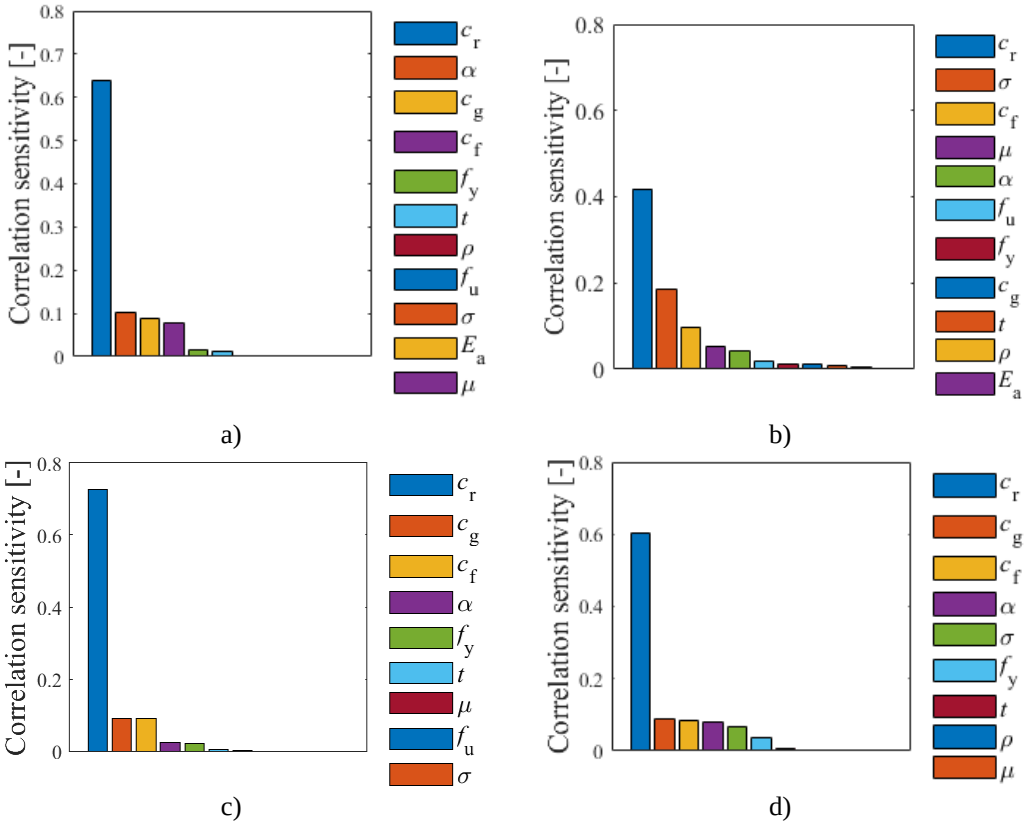

Figure 4.35. Sobol sensitivity indices for ULS a) Hungary, b) Hungary - Kriging, c) Hungary - Sződliget, and d) Sződliget

5 Conclusions

In the present dissertation, the FEM-based PBWE assessment of a telecommunication steel lattice tower is presented. The telecommunication steel lattice mast is equipped with wind speed and strain sensors and located in Central Hungary. The probabilistic characterization of a meteorological phenomenon, such as wind actions on structures is essential to get correct and accurate answers about the structural performance resulting in economic and optimal design. Furthermore, on-site data acquisition enables the assessment of parameters like stochastic extreme wind velocity, direction and roughness length based on measurements, since these parameters derived from a standard may frequently deviate from the actual conditions observed at the site. The study shows that Bayesian inference of extreme wind velocity model parameters allows combining short-duration measurements from the tower site with a more extensive dataset from nearby locations or even across the country, improving the design and verification of structures with limited measurement data.

A comprehensive numerical model is developed in a general-purpose finite element software for full probabilistic performance assessment of the lattice structure. It is demonstrated in this study that utilizing the innovative standardized FEM-based design approach, structural engineers can effectively account for multiple failure modes. The probabilistic analysis involves utilizing Monte Carlo simulation with random Latin hypercube sampling and fitting response surfaces for the output variables. By running simulations on the response surfaces with a large number of simulation loops, the analysis can efficiently evaluate the engineering demand parameters (EDPs), ensuring quick calculations and precise estimations.

A comparison was made between the internal axial forces obtained from strain measurements on the bottom chord member of a full-scale telecommunication lattice mast and the results from a deterministic numerical model. This model integrated wind load drag coefficients calculated according to EN 1993-3-1 and data from wind tunnel experiments. Notably, discrepancies in the internal axial forces under tension were observed, varying from 20% to 40% for wind velocities of 20 and 30 m/s. To address these discrepancies, wind forces measured in wind tunnel tests were exclusively applied to the upper tower segment (sections 7-9) to align with the utilized wind tunnel

experiments. Meanwhile, standard wind forces were employed for the lower tower section (sections 1-6), leading to a reduction of differences to approximately 10-20%.

The posterior predictive sampling is achieved by the Monte Carlo simulations on the derived response surfaces.

The analysis reveals that the scale parameter of the extreme wind velocity distribution has a notable influence on the selected EDPs when utilizing a 3.5-year measurement data series extracted from the site, solely applying the POT method. Therefore, it is essential to consider the uncertainty of the scale parameter when performing the calculations in this procedure. On the other hand, for the 20-year measurement data series in Hungary, the parameters σ and μ, calculated from the mean and standard deviation of the HMS wind velocities, have a relatively minor impact. This is possibly due to the standard deviations of these parameters not being determined through MLE fitting; instead, they were calculated using the standard error of the mean and standard deviation of the annual maxima wind speed data, leading to smaller standard deviations. However, in the case of Bayesian updating, these two parameters are found to be statistically insignificant; therefore, the uncertainty associated to this parameter can be neglected.

Using Kriging spatial interpolation to calculate wind speed values at the site of interest from longer data series of HMS stations, and even updating it with field measurement information, leads to a reliable and consistent result in line with previously mentioned estimated exceedance probabilities. The estimated exceedance probabilities of the "Hun - Kriging" are slightly smaller, by an order of magnitude for SLS, than the "Hungary" case.

The substantially lower wind speeds observed at both the tower site and the nearby station lead to considerably lower probabilities of failure compared to those calculated based on the national standard. The topography around Sződliget is characterized by the town on flat terrain, with the Danube River situated behind it. In contrast, the surroundings of the nearby station, Penc, feature hills with forested areas, which may contribute to lower wind speeds at 10 m height and assessed failure probabilities due to the influence of the terrain. These estimations may be considered as unconservative. Hence, our findings support the conclusion that the POT procedure without Bayesian updating, when applied with approximately 4 years of wind measurement data, tends to

underestimate the fundamental basic wind velocity. Consequently, the assessed reliability of the structure may be considered as unconservative. The comparison of internal axial forces in chord members based on measurements and finite element modelling, using wind forces calculated according to EN 1993-3-1 and wind tunnel tests, validates previous findings that the Eurocode tends to overestimate the wind load at higher velocities. Therefore, a higher degree of structural reliability can be attained through the execution of full-scale wind tunnel experiments and/or numerical simulations during the development of the second-generation Eurocode.

The objective of this research was to showcase the effectiveness of integrating site-specific wind loading models into the standardized FEM-based design framework as a powerful tool for design engineers.

6 New academic contributions

The scientific results derived from the research presented in this dissertation are summarized below.

6.1 Theses

6.1.1 Thesis 1

I compared the wind force, as calculated in accordance with EN 1993-3-1, to the wind force derived from wind tunnel experiments conducted by Balczó et al. (2006). These tests involved a bare mast section with a triangle cross-section with width of 1300 mm and a length of 1600 mm, constructed using hot-dip galvanized circular hollow sections with diameters of $D = 108$ mm for chord members and $D = 75$ mm for the bracing members. However, the EN 1993-3-1 standard formula conservatively omits the critical range and lacks specific definitions for the Reynolds number at which drag coefficients decrease. Consequently, there exists a disparity between the drag coefficient determined through wind tunnel measurements and the standard value and this difference falls within the range of 15-19% for Reynolds numbers spanning from $2.7\text{-}2.8 \cdot 10^5$, corresponding to the basic wind velocity determined in the Hungarian National Annex.

I conducted a comparison between the internal axial forces obtained from strain measurements on the bottom chord member of a full-scale telecommunication lattice mast and the results from a deterministic numerical model. This model incorporated wind load drag coefficients calculated according to EN 1993-3-1, as well as data from wind tunnel experiments. Differences in the internal axial forces under tension became apparent, with variations ranging from 20% to 40% for wind velocities of 20 and 30 m/s. To mitigate these discrepancies, wind forces measured in wind tunnel tests were applied exclusively to the upper tower segment, encompassing sections 7-9, because these sections align with the ones utilized in the wind tunnel experiments. For the lower part of the tower, comprising sections 1-6, standard wind forces were utilized. This adjustment resulted in a reduction of differences to approximately 10-20%.

Related publications: Kenéz, Á., and Joó, A. L. (2023a)

6.1.2 Thesis 2

In this investigation, the utilization of wind tunnel-derived drag/force coefficient c_f, instead of calculated according to EN 1993-3-1, significantly reduces the estimated probability of failure P_f by approximately two orders of magnitude. Adjusting the roughness length z_0 on the basis of on-site measurements, instead of the value proposed in EN 1991-1-4 standard for suburban terrain, can lead to one order of magnitude decrease in estimated P_f. The observed fundamental basic wind velocities at Sződliget and Penc are lower by 57% compared to the value considering all Hungarian meteorological stations. It results in significantly lower estimated P_f for these locations, with differences of approximately three orders of magnitude for SLS and around eight orders of magnitude for ULS. Applying Kriging spatial interpolation for extreme wind velocity calculations, along with Bayesian updating using observed data from the site of interest, results in a more reliable and consistent estimated P_f, aligning with other estimated exceedance probabilities where at least 20 year-long and multiple meteorological data series are considered. The Kriging spatial interpolation exhibits smaller estimated P_f by an order of magnitude compared to the reference case where the generalized extreme value distribution parameters calculated using the mean and standard deviation of the annual maxima wind velocity data. Furthermore, Bayesian updating of prior information associated with the Hungarian meteorological stations, incorporating observed data from the site of interest, reduces the P_f by approximately one order of magnitude compared to the reference case.

Related publications:
Kenéz, Á., and Joó, A. L. (2023a), Kenéz, Á., and Joó, A. L. (2023b)

6.1.3 Thesis 3

I demonstrated the significant impact of the scale parameter of the extreme wind velocity distribution on the selected Engineering Demand Parameters (EDPs) in the context of the probabilistic analysis within the presented Performance-based wind engineering framework. This impact is particularly significant when the Peaks Over Threshold (POT) method with automated threshold selection technique is employed with a dataset of fewer than 500 wind measurements and the generalized extreme value distribution parameters are estimated utilizing maximum likelihood estimation. Monte Carlo simulation, utilizing random Latin hypercube sampling with 160 samples (MCS) and a finite element model for structural analysis, is used to fit quadratic response surfaces for engineering demand parameters and develop a surrogate model. Subsequently, Monte Carlo simulations with $N = 10^6$ simulation loops are conducted on the derived response surfaces (RSM) to determine the probabilities of exceeding the specified limit values. The estimated Spearman rank-order correlation coefficient and the Sobol index of the scale parameter is 0.27 and 0.08, respectively. Therefore, it is crucial to account for the epistemic uncertainty associated with the scale parameter during the POT procedure.

Conversely, when utilizing Bayesian inference to synthesize information from the POT procedure, considering a dataset of fewer than 500 samples, alongside the Annual Maxima method and a 20-year long data series, the scale σ and location μ parameters are found to be statistically insignificant at a significance level of 2.5%. Consequently, the associated epistemic uncertainty related to these parameters can be safely disregarded.

Related publications:
Kenéz, Á., and Joó, A. L. (2023a), Kenéz, Á., and Joó, A. L. (2023b)

6.1.4 Thesis 4.

I devised a Performance-based wind engineering framework based on finite element method (FEM) improved by Bayesian inference to assess the reliability of a freestanding telecommunication lattice tower exposed to extreme wind conditions.

a) Here are the key components of this framework:

i. **Parameter Assessment:** Parameters for the stochastic extreme wind velocity model, including wind speed, direction, and roughness length, are determined through on-site data acquisition.

ii. **Threshold Selection:** In addition to the traditional annual maxima method, the peaks over threshold (POT) method is employed, enhanced by an innovative automated threshold selection technique introduced by Thompson et al. (2009) This approach is verified using conventional graphical diagnostics. The method had not been applied to wind velocity data before the studies were carried out.

iii. **Bayesian Inference:** Bayesian inference is leveraged to synthesize information from diverse sources of wind data measurements and various extreme wind velocity models. This application within the PBWE framework is novel in its approach.

iv. **Structural Response Modelling:** A finite element model is formulated to simulate the structural response of the tower. This facilitates structural engineers in accounting for various failure modes and complex phenomena.

v. **Probabilistic Analysis:** Monte Carlo simulation, supported by random Latin hypercube sampling and quadratic response surfaces, is adopted for probabilistic analysis. This approach accelerates and enhances the efficiency of calculations, ensuring a comprehensive assessment.

b) I proved the applicability of the method through a Performance-based analysis of a telecommunication lattice tower located in Central Hungary.

c) The average differences in estimated reliability indices, calculated based on P_{f} assuming Gaussian distribution of EDPs, corresponding to MCS and RSM are 2% and 5% for the SLS and ULS calculations, respectively. The maximum differences for the SLS and ULS calculations are 9% and 17%.

Related publications: Kenéz, Á., and Joó, A. L. (2023a), Kenéz, Á., Joó, A. L. (2020)

6.2 Relevant publications

Academic journal articles:

Kenéz, Á., and Joó, A. L. (2023a). Performance-based Wind Engineering assessment of a telecommunication mast utilizing Bayesian extreme wind velocity model, Stochastic Environmental Research and Risk Assessment, (2023), https://doi.org/10.1007/s00477-023-02596-w, Impact factor: 4.2 (Q1)

Kenéz, Á., and Joó, A. L. (2023b). The impact of parameter estimation uncertainty in extreme wind speed models. Pollack Periodica, 18 (2023) 1, pp. 78-83, https://doi.org/10.1556/606.2022.00645, Impact factor: 0.26 (Q3)

Kenéz, Á., and Joó, A. L. (2020). Parameter estimation and threshold selection uncertainty in extreme wind speed distribution – A frequentist approach with generalized Pareto distribution using automatic threshold selection. Idojárás, 124(3), pp. 311-330, https://doi.org/10.28974/idojaras.2020.3.1, Impact factor: 0.86 (Q4)

Conference papers:

Kenéz, Á., and Joó, A. L. (2023c), Performance-based wind engineering assessment of a telecommunication mast. ce/papers, 6(3-4), pp. 1099-1104.
https://doi.org/10.1002/cepa.2322

Kenéz, Á., and Joó, A. L. (2019), Extrém szélsebesség eloszlás paraméterbecslési bizonytalansága és hatása a tartószerkezetek megbízhatóságára - POT módszer automatikus küszöbválasztással, XIII. Magyar Mechanikai Konferencia, 2019.08.27-29.

Irrelevant publications and conference papers:

Szabó, G., Völgyi, I., Kenéz, Á., (2022) Vibration Assessment of a New Danube Bridge at Komárom", Periodica Polytechnica Civil Engineering, 66(4), pp. 1014–1022. https://doi.org/10.3311/PPci.19508, Impact factor: 1.3 (Q3)

Kenéz, Á., Jakab, S., Opoldusz, M., Joó, A. L. (2016) Vékonyfalú, hidegen alakított Z-szelemen átlapolt kapcsolatának vizsgálata, XX. Nemzetközi Építéstudományi Konferencia, Csíksomlyó, Románia, 2016.06.01-05., pp. 109-110

Lendvai A., Kenéz, Á., Rácz A., Joó, A. L. (2015) Acélcsarnokok burkolati merevsége - 3. rész: az Eurocode módszerének pontosítása. MAGÉSZ Acélszerkezetek 12: (1. különszám) pp. 78-83.

Kenéz, Á., Rácz A., Joó, A. L., Dunai, L. (2015) Acélcsarnokok trapézlemez burkolatának merevítő hatása, XIX. Nemzetközi Építéstudományi Konferencia, Csíksomlyó, Románia, 2015.06.04-07., pp. 97-100

Fenyvesi, O., Kenéz, Á., Kovács, É, Rácz, A. (2014) Ipari hulladékok újrahasznosítása beton adalékanyagként, Meddő? Hulladék? Nem! Haszonanyag!, Budapest, Hungary, 2014.05.15., pp. 111-118

Fenyvesi, O., Kenéz, Á., Kovács, É, Rácz, A. (2014) Szerkezeti könnyűbeton előregyártott hídszerkezeti elemekhez, XVIII. Nemzetközi Építéstudományi Konferencia, Csíksomlyó, Románia, 2014.06.12-15., pp. 149-152

6.3 Future research work

The drag coefficient stands as an area for potential future research. The drag coefficient for wind-structure interaction in the equivalent static method, as per EN 1993-3-1, is originally derived from wind tunnel tests at a reduced scale of 1:6, conducted by the National Maritime Institute (NMI) in the UK in 1977. Consequently, it appears that the formula provided by EN 1993-3-1 is more aligned with force coefficients observed at the model scale rather than in full-scale conditions. The standard distinguishes between circular members in the subcritical and supercritical range, setting the transition point at $Re = 4 \cdot 10^5$ while conservatively omitting the critical range. Considering the industry's goal of conserving resources and reducing costs through the acquisition of precise load data, there is a need for a closer examination of drag coefficients obtained from scaled tests in the UK during the 1970s. The challenge arises in determining the Reynolds number at which drag coefficients significantly decrease. To address this, further investigations through full-scale wind tunnel tests and computational fluid dynamics simulations are essential.

Another significant area for future research, particularly due to high uncertainty, is the basic wind velocity. In line with European Union directives, the Hungarian Meteorological Service (HMS) has made its observation and measurement data, from 2002 onwards, freely available for use through an open data server from 2021. The database allows for an in-depth examination of the fundamental wind speed in various regions across Hungary. A detailed comparison between the traditional method and the block method, along with the peak-over-threshold method, can be made using the data. Additionally, the implementation of the Offset Elliptical Normal model, as proposed by Cook (2019), could offer a more physically feasible depiction of joint and marginal wind speed and direction distributions, presenting a potentially effective strategy for wind climate modelling. The presented estimation process is based on the assumption of a stationary ergodic process, where the underlying process is considered constant over time with consistent parameter values. Future research can explore non-stationary analysis, which accounts for changes in the behaviour of extremes over time, allowing for the simultaneous variation of statistical properties. Moreover, a Markov chain Monte Carlo process can be explored to extend short data records by generating synthetic data series based on the statistics of the distribution revealed by the actual data sets.

Appendix

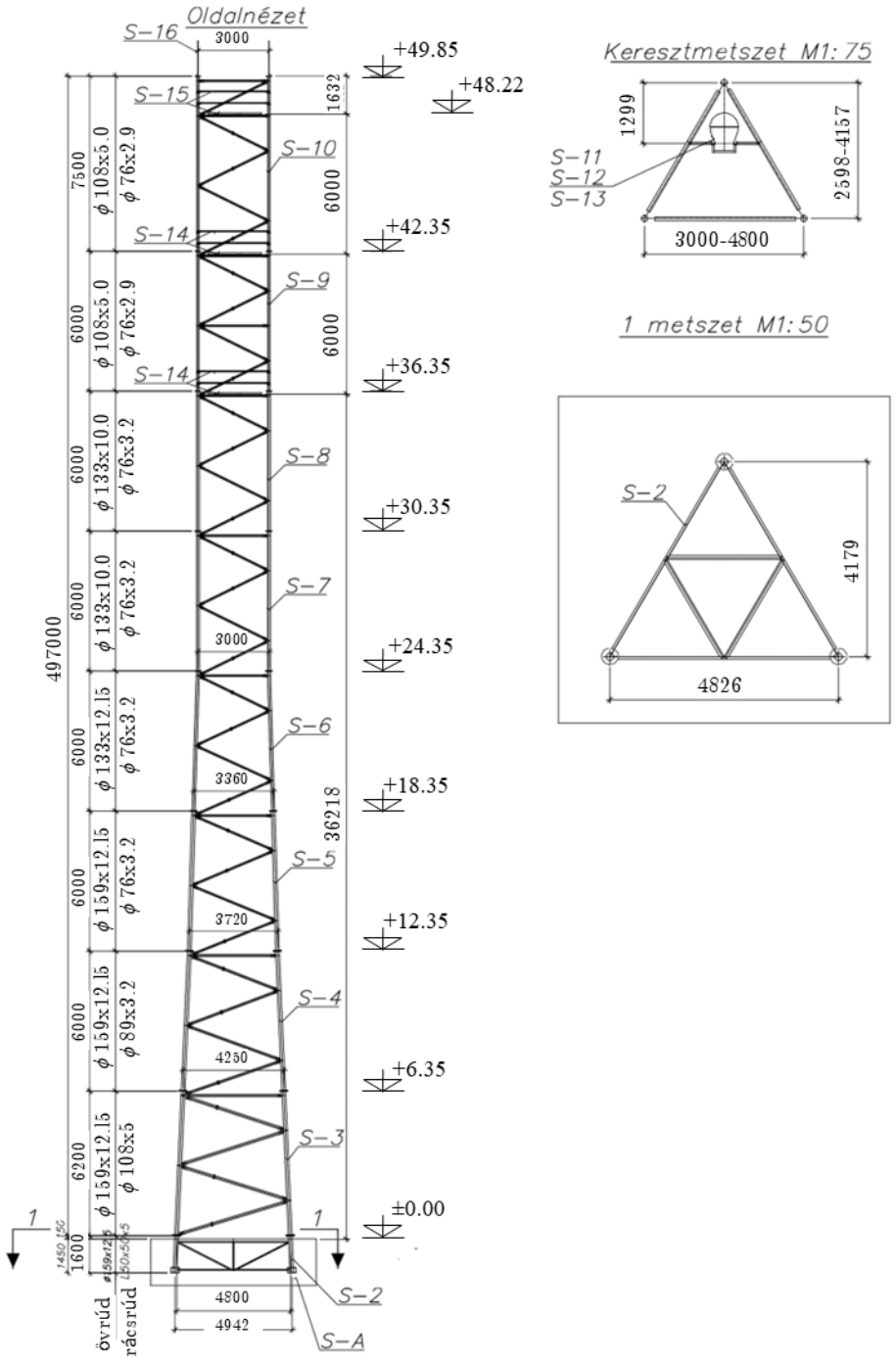

Figure A.1. The construction plan drawing of the telecommunication mast in Sződliget

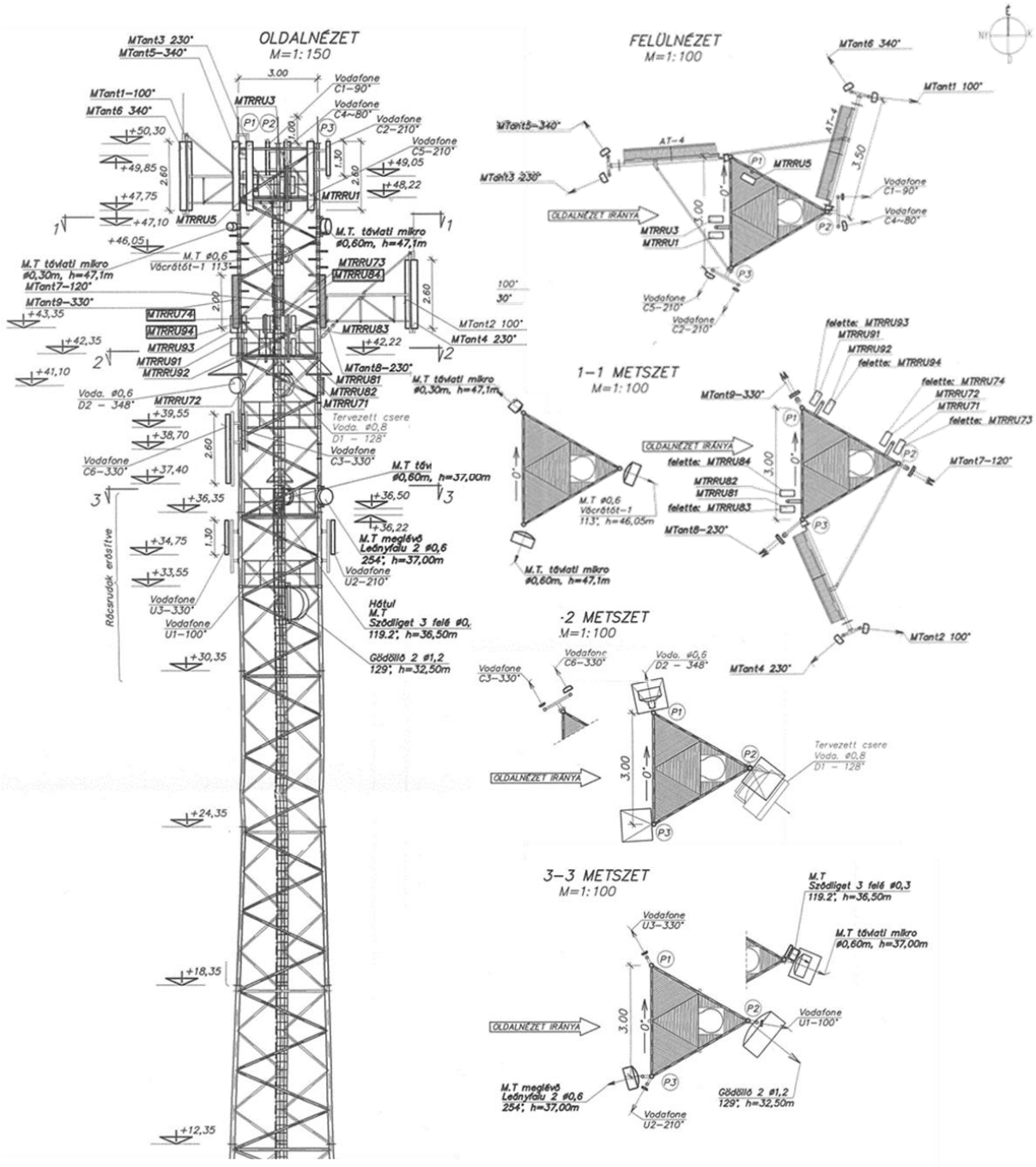

Figure A.2. Antennae installed on the telecommunication mast

Table A.1. Details of antennae installed on the telecommunication mast

Antenna #	**Section #**	**Face #**	**Antenna type**	A_{ant} [m²]	$c_{f,A,0}$ [-]	α_{min} [°]	α_{max} [°]	z [m]
1	9	3	Sector	2.6×0.26×2×1.5	1.4	300	120	47.75
2	9	3	Sector	1.3×0.16×1.1	1.4	300	120	49.05
3	9	2	Sector	2.6×0.26×1.1	1.4	360	240	47.75
4	9	2	Sector	1.3×0.16×1.1	1.4	60	240	49.05
5	9	1	Sector	2.6×0.26×1.1	1.4	120	0	47.75
6	9	1	Sector	2.6×0.26×2×1.5	1.4	180	0	47.75
7	8	2	Microwave	0.62×π/4	1.4	60	270	47.10
8	8	1	Microwave	0.32×π/4	1.4	180	90	47.10
9	8	3	Microwave	0.62×π/4	1.4	360	210	46.05
10	8	2	Sector	2.6×0.26×2×1.5	1.4	60	270	43.35
11	8	1	Sector	2.0×0.30×1.1	1.4	180	0	43.35
12	8	2	Sector	2.0×0.30×1.1	1.4	360	180	43.35
13	8	3	Sector	2.0×0.30×1.1	1.4	210	90	43.35
14	7	3	Microwave	0.62×π/4	1.4	210	90	41.10
15	7	2	Microwave	0.82×π/4	1.4	360	240	41.10
16	7	1	Sector	1.3×0.16×1.1	1.4	180	0	38.70
17	7	3	Sector	2.6×0.26×1.1	1.4	270	120	37.40
18	7	2	Microwave	0.62×π/4	1.4	120	0	37.00
19	7	3	Microwave	0.32×π/4	1.4	300	180	36.50
20	6	1	Sector	1.3×0.16×1.1	1.4	90	330	34.75
21	6	2	Sector	1.3×0.16×1.1	1.4	210	90	34.75
22	6	3	Sector	1.3×0.16×1.1	1.4	330	210	34.75
23	6	2	Microwave	1.22×π/4	1.4	360	240	32.50

Table A.2. Measured internal axial forces S for various wind speeds v and turbulence intensities I_v

		$I_v = 10\%$			$I_v = 20\%$			$I_v = 30\%$		
v [m/s]	α [°]	S_1 [kN]	S_2 [kN]	S_3 [kN]	S_1 [kN]	S_2 [kN]	S_3 [kN]	S_1 [kN]	S_2 [kN]	S_3 [kN]
30	270	-	-	-	83.75	-182.53	81.36	93.52	-201.19	96.04
	300	-	-	-	138.03	-163.85	-11.57	148.34	-190.54	-15.83
	330	-	-	-	148.88	-97.25	-103.55	152.33	-117.79	-163.21
20	270	-	-	-	39.26	-81.11	37.95	42.32	-96.82	42.37
	300	-	-	-	69.20	-74.30	-7.21	70.83	-85.50	-5.78
	330	-	-	-	77.93	-39.57	-49.16	80.11	-59.28	-49.78
15	270	17.87	-39.00	15.88	19.96	-45.80	18.25	21.24	-61.31	17.16
	300	32.19	-33.57	-3.59	38.75	-41.65	-5.85	40.28	-55.35	-6.82
	330	37.22	-20.13	-23.80	44.84	-22.95	-31.44	45.95	-39.05	-33.08
10	270	5.93	-19.00	3.26	7.15	-22.80	6.86	4.58	-38.33	1.44
	300	13.03	-17.29	-5.10	19.38	-19.58	-3.16	22.57	-34.49	-7.64
	330	15.42	-12.71	-13.11	22.95	-13.16	-13.14	24.23	-23.57	-17.09

Table A.3. Internal axial forces S for various wind speeds v utilizing c_f according to EN 1993-3-1 and wind tunnel test

		c_f - EN 1993-3-1			c_f - Wind tunnel test		
v [m/s]	α [°]	S_1 [kN]	S_2 [kN]	S_3 [kN]	S_1 [kN]	S_2 [kN]	S_3 [kN]
30	270	103.00	-209.65	106.58	86.62	-176.65	89.97
	300	184.03	-186.42	1.96	154.48	-156.73	1.82
	330	212.25	-107.70	-104.65	179.34	-91.18	-88.28
20	270	46.88	-95.46	48.53	40.12	-81.83	41.67
	300	83.73	-84.84	0.91	71.49	-72.54	0.85
	330	96.58	-49.03	-47.62	82.99	-42.20	-40.86
15	270	27.21	-55.40	28.17	23.69	-48.32	24.60
	300	48.56	-49.20	0.52	42.18	-42.79	0.49
	330	56.02	-28.44	-27.62	48.97	-24.89	-24.11
10	270	12.31	-25.07	12.74	11.03	-22.50	11.45
	300	21.97	-22.26	0.24	19.62	-19.90	0.23
	330	25.35	-12.87	-12.50	22.78	-11.57	-11.22

Table A.4. Parameters of fitted lognormal distributions of the rotation of the top node φ_{top} for SLS

	Simulation type	μ_{ln} [m/s]	σ_{ln} [m/s]	**Variance** μ_{ln}	**Variance** σ_{ln}	**Covariance** μ_{ln} - σ_{ln}
Hungary	MCS	-1.741	0.495	$1.53 \cdot 10^{-3}$	$7.74 \cdot 10^{-4}$	$1.72 \cdot 10^{-19}$
	RSM	-1.752	0.518	$2.68 \cdot 10^{-7}$	$1.34 \cdot 10^{-7}$	$5.95 \cdot 10^{-23}$
Hun - Kriging	MCS	-2.122	0.482	$1.45 \cdot 10^{-3}$	$7.32 \cdot 10^{-4}$	$7.72 \cdot 10^{-19}$
	RSM	-2.127	0.494	$2.44 \cdot 10^{-7}$	$1.22 \cdot 10^{-7}$	$1.04 \cdot 10^{-22}$
Hungary - Wind tunnel force	MCS	-1.987	0.447	$1.25 \cdot 10^{-3}$	$6.29 \cdot 10^{-4}$	$-1.82 \cdot 10^{-19}$
	RSM	-1.983	0.464	$2.15 \cdot 10^{-7}$	$1.08 \cdot 10^{-7}$	$-3.92 \cdot 10^{-23}$
Hungary - $z_0 = 0.3$ m	MCS	-1.468	0.490	$1.50 \cdot 10^{-3}$	$7.58 \cdot 10^{-4}$	$-4.04 \cdot 10^{-19}$
	RSM	-1.474	0.489	$2.40 \cdot 10^{-7}$	$1.20 \cdot 10^{-7}$	$3.65 \cdot 10^{-22}$
Hun - Sződliget	MCS	-1.918	0.516	$1.66 \cdot 10^{-3}$	$8.39 \cdot 10^{-4}$	$3.17 \cdot 10^{-19}$
	RSM	-1.905	0.478	$2.29 \cdot 10^{-7}$	$1.14 \cdot 10^{-7}$	$3.80 \cdot 10^{-23}$
Hun - Kriging - Sződliget	MCS	-2.131	0.517	$1.67 \cdot 10^{-3}$	8.45E-04	$1.05 \cdot 10^{-18}$
	RSM	-2.138	0.539	$2.91 \cdot 10^{-7}$	$1.46 \cdot 10^{-7}$	$-8.362 \cdot 10^{-23}$
Penc - Sződliget	MCS	-2.905	0.482	$1.45 \cdot 10^{-3}$	$7.32 \cdot 10^{-4}$	$1.54 \cdot 10^{-19}$
	RSM	-2.908	0.485	$2.35 \cdot 10^{-7}$	$1.18 \cdot 10^{-7}$	$2.92 \cdot 10^{-22}$
Sződliget	MCS	-2.828	0.496	$1.53 \cdot 10^{-3}$	$7.75 \cdot 10^{-4}$	$1.17 \cdot 10^{-18}$
	RSM	-2.825	0.501	$2.51 \cdot 10^{-7}$	$1.25 \cdot 10^{-7}$	$1.99 \cdot 10^{-22}$

Table A.5. Parameters of fitted lognormal distributions of load amplification factor α_{ULS} for ULS

	Simulation type	μ_{ln} [m/s]	σ_{ln} [m/s]	**Variance** μ_{ln}	**Variance** σ_{ln}	**Covariance** μ_{ln} - σ_{ln}
Hungary	MCS	1.701	0.453	$1.28 \cdot 10^{-3}$	$6.48 \cdot 10^{-4}$	$-1.20 \cdot 10^{-18}$
	RSM	1.674	0.489	$2.40 \cdot 10^{-7}$	$1.20 \cdot 10^{-7}$	$-2.00 \cdot 10^{-23}$
Hun - Kriging	MCS	1.746	0.500	$1.56 \cdot 10^{-3}$	$7.89 \cdot 10^{-4}$	$-1.21 \cdot 10^{-18}$
	RSM	1.752	0.505	$2.55 \cdot 10^{-7}$	$1.28 \cdot 10^{-7}$	$2.31 \cdot 10^{-23}$
Hungary - Wind tunnel force	MCS	1.866	0.422	$1.11 \cdot 10^{-3}$	$5.61 \cdot 10^{-4}$	$-1.20 \cdot 10^{-19}$
	RSM	1.865	0.424	$1.80 \cdot 10^{-7}$	$9.00 \cdot 10^{-8}$	$-1.42 \cdot 10^{-23}$
Hungary - $z_0 = 0.3$ m	MCS	1.464	0.486	$1.48 \cdot 10^{-3}$	$7.45 \cdot 10^{-4}$	$3.89 \cdot 10^{-19}$
	RSM	1.463	0.515	$2.65 \cdot 10^{-7}$	$1.33 \cdot 10^{-7}$	$-1.05 \cdot 10^{-22}$
Hun - Sződliget	MCS	1.855	0.448	$1.25 \cdot 10^{-3}$	$6.32 \cdot 10^{-4}$	$4.84 \cdot 10^{-19}$
	RSM	1.842	0.455	$2.07 \cdot 10^{-7}$	$1.04 \cdot 10^{-7}$	$9.13 \cdot 10^{-23}$
Hun - Kriging - Sződliget	MCS	2.058	0.433	$1.17 \cdot 10^{-3}$	$5.90 \cdot 10^{-4}$	$6.10 \cdot 10^{-19}$
	RSM	2.031	0.504	$2.54 \cdot 10^{-7}$	$1.27 \cdot 10^{-7}$	$-1.31 \cdot 10^{-22}$
Penc - Sződliget	MCS	2.659	0.337	$7.10 \cdot 10^{-4}$	$3.58 \cdot 10^{-4}$	$-6.40 \cdot 10^{-19}$
	RSM	2.662	0.341	$1.16 \cdot 10^{-7}$	$5.82 \cdot 10^{-8}$	$-9.74 \cdot 10^{-25}$
Sződliget	MCS	2.603	0.361	$8.12 \cdot 10^{-4}$	$4.10 \cdot 10^{-4}$	$8.83 \cdot 10^{-19}$
	RSM	2.600	0.379	$1.44 \cdot 10^{-7}$	$7.19 \cdot 10^{-8}$	$-1.93 \cdot 10^{-22}$

References

Ahn, S., Fessler, J. A. (2003). Standard errors of mean, variance, and standard deviation estimators. *Technical Report 413, Comm. and Sign. Proc. Lab., Dept. of EECS, Univ. of Michigan, Ann Arbor, MI*, *48109–2122*.

Bakker, F. P., De Koker, N., Viljoen, C. (2021). Preconditioning wind speeds for standardised structural design. *Engineering Structures*, *238*, 111856. https://doi.org/https://doi.org/10.1016/j.engstruct.2021.111856

Balczó, M., Goricsán, I., Kovács, T., Lajos, T., Régert, T., and Sebestyén, P. (2006). Prediction of wind load acting on telecommunication masts. *IABSE Symposium: Responding to Tomorrow's Challenges in Structural Engineering*, 23–30. https://doi.org/10.2749/222137806796169236

Baravalle, M., Köhler, J. (2018). On the probabilistic representation of the wind climate for calibration of structural design standards. *Structural Safety*. https://doi.org/10.1016/j.strusafe.2017.10.012

Birjulin, A. P., Burgsdorf, V. V, Makhlin, B. J. (1960). *Wind Loads on Overhead Lines*. Paper.

Briggs, A. H., Weinstein, M. C., Fenwick, E. A. L., Karnon, J., Sculpher, M. J., Paltiel, A. D. (2012). Model parameter estimation and uncertainty analysis: A report of the ISPOR-SMDM modeling good research practices task force working group-6. *Medical Decision Making*. https://doi.org/10.1177/0272989X12458348

C, L., Y, O., Ma, X., JE, M. (2016). Structural Analysis of Lattice Steel Transmission Towers: A Review. *Journal of Steel Structures & Construction*, *2*(1), 1–11. https://doi.org/10.4172/2472-0437.1000114

Calotescu, I., Torre, S., Freda, A., Solari, G. (2021). Wind tunnel testing of telecommunication lattice towers equipped with ancillaries. *Engineering Structures*, *241*, 112526. https://doi.org/10.1016/j.engstruct.2021.112526

CEN. (2005). *EN 1991-1-4 :2005, Eurocode 1: Actions on structures - Part 1-4: General actions - Wind actions*.

CEN. (2006). *EN 1993-3-1:2006, Eurocode 3 - Design of steel structures - Part 3-1: Towers, masts and chimneys - Towers and masts*.

CEN. (2020). *prEN 1993-1-14:2020, Eurocode 3: Design of steel structures, Part 1-14: Design assisted by Finite element analysis (under development by European Committee for Standardization*.

Chuang, W.-C., Spence, S. M. J. (2017). A performance-based design framework for the integrated collapse and non-collapse assessment of wind excited buildings. *Engineering Structures*, *150*, 746–758. https://doi.org/https://doi.org/10.1016/j.engstruct.2017.07.030

Ciampoli, M., Petrini, F., Augusti, G. (2011). Performance-Based Wind Engineering: Towards a general procedure. *Structural Safety*. https://doi.org/10.1016/j.strusafe.2011.07.001

Coles, S. (2001). *An Introduction to Statistical Modeling of Extreme Values* (3rd ed.). Springer.

Cook, N. J. (1982). Towards better estimation of extreme winds. *Journal of Wind Engineering and Industrial Aerodynamics*, *9*(3), 295–323. https://doi.org/10.1016/0167-6105(82)90021-6

Cook, N. J. (1985). *The designer's guide to wind loading of building structures. Part 1.: Background, Damage Survey, Wind Data and Structural Classification*. Building Research Establishment. Garston and Butterworths.

Cook, N. J. (2019). The OEN mixture model for the joint distribution of wind speed and direction: A globally applicable model with physical justification. *Energy Conversion and Management*, *191*, 141–158. https://doi.org/https://doi.org/10.1016/j.enconman.2019.04.015

Cook, N. J., Ian Harris, R. (2001). Discussion on Application of the generalized Pareto distribution to extreme value analysis in wind engineering by J.D. Holmes, W.W. Moriarty. *Journal of Wind Engineering and Industrial Aerodynamics*. https://doi.org/10.1016/s0167-6105(00)00063-5

Cooley, D. (2016). DIPAK K. DEY, JUN YAN, EDS. Extreme Value Modeling and Risk Analysis: Methods and Applications. *CRC Press, Taylor & Francis Group*, *Boca Raton*.

Davenport, A. G. (1961). The spectrum of horizontal gustiness near the ground in high winds. *Quarterly Journal of the Royal Meteorological Society*, *87*(372), 194–211. https://doi.org/https://doi.org/10.1002/qj.49708737208

Davenport, A. G. (1982). The interaction of wind and structures. In Erich J. Plate (Ed.), *Engineering meteorology*. Elsevier. https://www.scopus.com/inward/record.uri?eid=2-s2.0-0020227057&partnerID=40&md5=e08f250c15c6480c2746222a2dae28b4

Davenport, A. G. (1993). Wind Climate in Cities. In J. E. Cermak, A. G. Davenport, E. J. Plate, & D. X. Viegas (Eds.), *Wind Climate in Cities*. https://doi.org/10.1007/978-94-017-3686-2

Depina, I., Divić, V., Munjiza, A., Peroš, B. (2021). Perfomance-based wind engineering assessment of critical telecommunication infrastructure subjected to bora wind. *Engineering Structures*, *236*, 112083. https://doi.org/10.1016/j.engstruct.2021.112083

Ducloux, H., Figueroa, L. (2016). Background information about the wind action model of CENELEC EN 50341-1 (2012) and associated expected reliability of electrical overhead lines. *Journal of Wind Engineering and Industrial Aerodynamics*, *157*, 104–117. https://doi.org/https://doi.org/10.1016/j.jweia.2016.08.006

ECCS Technical Committee T2: Wind Effects. (1978). Recommendations for the Calculation of Wind Effects on Buildings and Structures. In *European Convention for Construction Steelwork*. Elsevier.

Fisher, R. A., Tippett, L. H. C. (1928). Limiting forms of the frequency distribution of the largest or smallest member of a sample. *Mathematical Proceedings of the Cambridge Philosophical Society*. https://doi.org/10.1017/S0305004100015681

G., D. A. (1967). Gust Loading Factors. *Journal of the Structural Division*, *93*(3), 11–34. https://doi.org/10.1061/JSDEAG.0001692

Gardner, L., Yun, X., Fieber, A., Macorini, L. (2019). Steel Design by Advanced Analysis: Material Modeling and Strain Limits. *Engineering*, *5*(2), 243–249. https://doi.org/https://doi.org/10.1016/j.eng.2018.11.026

Gatey, D. A., Miller, C. A. (2007). An investigation into 50-year return period wind speed differences for Europe. *Journal of Wind Engineering and Industrial Aerodynamics*, *95*, 1040–1052. https://doi.org/10.1016/j.jweia.2007.01.016

Georgakis, C. T., Støttrup-Andersen, U., Johnsen, M., Nielsen, M. G., Koss, H. H. (2009). Drag coefficients of lattice masts from full-scale wind-tunnel tests. *5th European and African Conference on Wind Engineering, EACWE 5, Proceedings*.

Gnedenko, B. (1943). Sur La Distribution Limite Du Terme Maximum D'Une Serie Aleatoire. *The Annals of Mathematics*. https://doi.org/10.2307/1968974

H. Mors, K.W. Baer, M. E. (1956). Wind Pressure on Stranded Conductors – Hornisgrinde Testing Station. *Sweden, CIGRE Report*, *220*.

Harris, R. I., Cook, N. J. (2014). The parent wind speed distribution: Why Weibull? *Journal of Wind Engineering and Industrial Aerodynamics*, *131*, 72–87. https://doi.org/10.1016/j.jweia.2014.05.005

Holmes, J. D. (2002). Effective static load distributions in wind engineering. *Journal of Wind Engineering and Industrial Aerodynamics*, *90*, 91–109. https://doi.org/10.1016/S0167-6105(01)00164-7

Holmes, J. D., Moriarty, W. W. (1999). Application of the generalized Pareto distribution to extreme value analysis in wind engineering. *Journal of Wind Engineering and Industrial Aerodynamics*, *83*(1), 1–10. https://doi.org/https://doi.org/10.1016/S0167-6105(99)00056-2

Holmes, J. D., Moriarty, W. W. (2001). Response to discussion by N.J. Cook and R.I. Harris. *Journal of Wind Engineering and Industrial Aerodynamics*. https://doi.org/10.1016/s0167-6105(00)00064-7

Hoven, B. I. Van Der. (1956). Power spectrum of horizontal wind speed in the frequency. *Journal of meteorology*, *14*.

Huang, M. F., Chan, C. M., Lou, W. J. (2012). Optimal performance-based design of wind sensitive tall buildings considering uncertainties. *Computers & Structures*, *98–99*, 7–16. https://doi.org/https://doi.org/10.1016/j.compstruc.2012.01.012

IEC. (2022). IEC 61400-50-1:2022 Wind energy generation systems - Part 50-1: Wind measurement - Application of meteorological mast, nacelle and spinner mounted instruments. *International Electrotechnical Commission*.

James Pickands III. (1975). Statistical Inference Using Extreme Order Statistics. *The Annals of Statistics*. https://doi.org/10.1214/aos/1176343003

Joint Committee on Structural Safety. (2001). *JCSS Probabilistic Model Code*.

Kang, S., Song, J. (2017). Parameter and quantile estimation for the generalized Pareto distribution in peaks over threshold framework. *Journal of the Korean Statistical Society*. https://doi.org/10.1016/j.jkss.2017.02.003

Koss, H., Srouji, R. G. (2015). Scaling Issues in the Determination of Wind loads on

Lattice Masts. *14th International Conference on Wind Engineering*, 9.

Kövesdi, B., Kollár, D., Dunai, L., Horváth, A. (2022). Reliability analysis-based investigation of the historical Széchenyi Chain Bridge deck system. *Results in Engineering*, *15*, 100555. https://doi.org/https://doi.org/10.1016/j.rineng.2022.100555

Kundu, P. K., Cohen, I. M., Dowling, D. R. (2016). Boundary Layers and Related Topics. In *Fluid Mechanics*. https://doi.org/10.1016/b978-0-12-405935-1.00010-1

Kwon, D. K., Kareem, A. (2013). Comparative study of major international wind codes and standards for wind effects on tall buildings. *Engineering Structures*, *51*, 23–35. https://doi.org/10.1016/j.engstruct.2013.01.008

Landberg, L. (2015). Meteorology for Wind Energy. In *Meteorology for Wind Energy*. https://doi.org/https://doi.org/10.1002/9781118913451.fmatter

Lechner, J. A., Leigh, S. D., Simiu, E. (1992). Recent approaches to extreme value estimation with application to wind speeds. Part I: the pickands method. *Journal of Wind Engineering and Industrial Aerodynamics*, *41–44*, 509–519. https://doi.org/10.1016/0167-6105(92)90457-L

Lee, J. K., Lee, K. H., Kim, S. Il, Yook, D., Ahn, S. (2017). Weibull parameter calculation and estimation of wind speeds for the return period: A case study in the Kori and Wolsong NPP areas. *Annals of Nuclear Energy*, *108*, 406–412. https://doi.org/10.1016/j.anucene.2017.04.040

Lee, M. D., Wagenmakers, E.-J. (2013). *Bayesian Cognitive Modeling*. Cambridge University Press.

Lettau, H. (1950). A Re-examination of the "Leipzig Wind Profile" Considering some Relations between Wind and Turbulence in the Frictional Layer. *Tellus*, *2*(2), 125–129. https://doi.org/10.3402/tellusa.v2i2.8534

Lungu, D., Gelder, P. H. A. J. M., Trandafir, R. (1996). Comparative study of Eurocode 1, ISO and ASCE procedures for calculating wind loads. *IABSE Reports*, *74*.

Ma, T., Cui, W., Zhao, L., Yejun, D., Genshen, F., Ge, Y. (2023). Extreme wind speed prediction in mountainous area with mixed wind climates. *Stochastic Environmental Research and Risk Assessment*, *37*(3), 1163–1181. https://doi.org/10.1007/s00477-022-02335-7

Malakatas, N. (2023). *DIBt Eurocode Conference 2023 - EN 1991 "Actions on*

structures." Berlin, 24 May 2023.

Marchal, G. H., Dienne, G., Jacques, A. (1956). The Action of Wind on Overhead Line Conductors. *CIGRE Paper*, *216*.

Mildner P. (1932). Uber Reibung in einer speziellen Luftmasse. *Beiträge Zur Physik Der Atmosphäre*, *19*, 151–158.

Nielsen, M. G. (2019). New Eurocode for Towers, Masts and Chimneys. *Ce/Papers*. https://doi.org/10.1002/cepa.1094

Oke, T. R. (1987). Boundary layer climates, Second edition. In *Routledge*.

P Palutikof, J., Brabson, B., Lister, D., T Adcock, S. (1999). A review of methods to calculate extreme wind speeds. *Meteorological Applications*, *6*, 119–132.

Paulotto, C., Ciampoli, M., Augusti, G. (2004). Some proposals for a first step towards a Performance Based Wind Engineering. *International Journal (Toronto, Ont.)*.

Peña, A., Floors, R., Gryning, S.-E. (2014). The Høvsøre Tall Wind-Profile Experiment: A Description of Wind Profile Observations in the Atmospheric Boundary Layer. *Boundary-Layer Meteorology*, *150*(1), 69–89. https://doi.org/10.1007/s10546-013-9856-4

Petrini, F., Ciampoli, M. (2012). Performance-based wind design of tall buildings. *Structure and Infrastructure Engineering*, *8*(10), 954–966. https://doi.org/10.1080/15732479.2011.574815

Pop, L., Sokol, Z., Hanslian, D. (2016). A new method for estimating maximum wind gust speed with a given return period and a high areal resolution. *Journal of Wind Engineering and Industrial Aerodynamics*, *158*, 51–60. https://doi.org/10.1016/j.jweia.2016.09.005

Poyart, R. (1952). Experimental Research on Ice-Coating and Wind Action on Single and Bundle Conductors. *France, CIGRE Report*, *234*.

Prud'homme, S., Legeron, F., Langlois, S. (2018). Calculation of wind forces on lattice structures made of round bars by a local approach. *Engineering Structures*, *156*, 548–555. https://doi.org/10.1016/j.engstruct.2017.11.065

Rózsás, Á., Sýkora, M. (2016). Effect of Statistical Uncertainties on Predicted Extreme Wind Speeds. *Proceedings, 7th International Workshop on Reliable Engineering Computing (REC)*.

Tessari, R. K., Kroetz, H. M., Beck, A. T. (2017). Performance-based design of steel towers subject to wind action. *Engineering Structures*, *143*, 549–557. https://doi.org/https://doi.org/10.1016/j.engstruct.2017.03.053

Thompson, P., Cai, Y., Reeve, D., Stander, J. (2009). Automated threshold selection methods for extreme wave analysis. *Coastal Engineering*. https://doi.org/10.1016/j.coastaleng.2009.06.003

Troen, I., Petersen, E. L. (1989). European Wind Atlas. In *Risø, National Laboratory, Roskilde*.

Vrouwenvelder, T., Scholten, N. (2010). Assessment criteria for existing structures. *Structural Engineering International: Journal of the International Association for Bridge and Structural Engineering (IABSE)*. https://doi.org/10.2749/101686610791555595

WMO. (2021). World Meteorological Organization— Guide to Instruments and Methods of Observation. In *The Europa Directory of International Organizations 2021* (2021 editi).

Zetterholm, O. D., Sandin, S. (1954). Wind Pressure on Overhead Transmission Line Conductors. *Sweden, CIGRE Report*, *202*.